Measurement of the Ratio of Inclusive Cross Sections $\sigma(p\bar{p} \rightarrow Z + b\text{-jet})/\sigma(p\bar{p} \rightarrow Z + \text{jet})$ at $\sqrt{s} = 1.96$ TeV

A Dissertation Presented

by

Yıldırım Doğan Mutaf

to

The Graduate School

in Partial Fulfillment of the Requirements

for the Degree of

Doctor of Philosophy

in

Physics

Stony Brook University

May 2005

State University of New York
at Stony Brook

The Graduate School

Yıldırım Doğan Mutaf

We, the dissertation committee for the above candidate for the Doctor of Philosophy degree, hereby recommend the acceptance of the dissertation.

Professor Paul D. Grannis
Dissertation Advisor
Department of Physics and Astronomy, SUNY at Stony Brook

Professor John D. Hobbs
Chairman of Defense Committee
Department of Physics and Astronomy, SUNY at Stony Brook

Professor Jack Smith
Committee Member
Department of Physics and Astronomy, SUNY at Stony Brook

Professor Gregorio Bernardi
Committee Member
LPNHE, University of Paris VI

This dissertation is accepted by the Graduate School.

Dean of the Graduate School

Abstract of the Dissertation

Measurement of the Ratio of Inclusive Cross Sections
$\sigma(p\bar{p} \to Z + b\text{-jet})/\sigma(p\bar{p} \to Z + \text{jet})$ at $\sqrt{s} = 1.96$ TeV

by

Yıldırım Doğan Mutaf

Doctor of Philosophy

in

Physics

Stony Brook University

2005

Using the data collected with the DØ detector at $\sqrt{s} = 1.96$ TeV with integrated luminosities of about 180 pb^{-1}, we have measured the ratio of inclusive cross sections for $p\bar{p} \to Z + b$-jet to $p\bar{p} \to Z + \text{jet}$ production. The inclusive $Z + b$-jet reaction is an important background to searches for the Higgs boson in associated ZH production at the Fermilab Tevatron collider and is sensitive to the b quark content of the proton. This thesis describes our measurement which is performed using the dimuon decay channel of the Z boson, i.e. $Z \to \mu^+\mu^-$. The ratio in the dimuon channel is measured to be 1.86 ± 0.44 (stat) $^{+0.24}_{-0.28}$ (syst)% for hadronic jets with transverse momenta $p_T > 20$ GeV/c and pseudorapidities $|\eta| < 2.5$, consistent with next-to-leading order predictions of the standard model. This measurement is also combined with the result of the same ratio using the dielectron decay of the Z boson, and the combined measurement of the ratio of cross-sections yields 2.11 ± 0.41 (stat) $^{+0.22}_{-0.25}$ (syst)%.

In addition to our measurement, we also study optimization procedures for the search of $Z(\mu\bar{\mu}) + b\bar{b}$ signal at DØ . We demonstrate that substantial improvements in the signal sensitivity can be obtained by choosing more optimal selection cuts tailored for this signal and by combining the attributes of the similar objects in the events like muons and jets.

Contents

List of Figures

List of Tables

Acknowledgments

There is a long list of people to acknowledge their help and support which played a significant role in earning my doctoral degree. I would like to start by saying that I could not be where I am today without the continuous encouragement, support and love of my family; especially my parents Lutfi and Saadet Mutaf. I am blessed with the tremendous dedication and effort they devoted on me to have a high quality education despite all the economical hardship of the past times. My sisters Feride, Suna, Selma and Yasemin deserve equal gratitude for giving up their priorities at many times for the benefit of my brother Cihan and I.

I would like to extend my thanks to the newest member of our family; my dear wife Asli, who constantly supported me in the stressful years of the graduate school and embraced me with her endless love and care. Living fifteen minutes apart in Istanbul for many years without knowing each other and meeting 8000 miles away for the first time, I feel extremely fortunate to have you in my life.

I am deeply indebted to my advisor, Prof. Paul D. Grannis for his guidance and wisdom from which I learned a lot through my Ph.D. years. Paul introduced me to DØ and supported me to be a part of this world-class high energy physics experiment at Fermilab. Through our frequent discussions during my Ph.D. studies, he thought me how to approach to problems and always encouraged me to look for ways of improvement. I consider myself very lucky to be one of his students. I would also like to express my sincere gratitude to Prof. John D. Hobbs, my co-advisor, who acquainted me with

the Higgs group at DØ and has always been there to evaluate my studies and provide me with invaluable direction.

The scientific work presented in this thesis would not have been possible without the tireless efforts by the entire DØ collaboration, the Fermilab Accelerator Division and financial support by the funding agencies. I am also thankful to the Higgs group members at DØ with whom I have closely worked and benefited from the frequent meetings we had during my Ph.D. studies. On an individual basis, I wish to emphasize the invaluable support I received from Prof. Avto Kharchilava, Dr. Suyong Choi, Dr. Qizhong Li and Dr. Kazu Hanagaki in the Higgs group. It was a great pleasure to be a part of this team.

Significant thanks go to the remainder of the past and present Stony Brook High Energy group members: Dr. Levan Babukhadia for helping me start off on a good track in my first years at DØ ; Dr. Sherry Towers for supplying me with her vast reserve of statistical methods; Dr. Dean Schamberger and Satish Desai for providing excellent computing support and always being there when I had problems or questions to ask; Joan Napolitano and Alice Cichanowitz-Dugan for the local support they provide at Stony Brook.

Chapter 1

Introduction

The work presented in this thesis describes a study of the b-jet production in association with electroweak Z boson. The study consists of two parts. First, we make a measurement of the ratio of cross sections for inclusive $Z + b$-jet process to inclusive Z+jet processes in the dimuon channel. The result from the dimuon channel of the Z boson decay is also combined with a similar measurement performed in the dielectron channel. These results provide the first experimental tests of the theoretical predictions on the production cross sections for the respective processes and establish an important first step for the search for the Higgs boson.

In the second part of our study, we look for ways to perform an optimized search for the $Z + b\bar{b}$ production which is the most important background for the Higgs boson in the similar final state. We believe custom tailored analysis schemes are more suitable for these type of rare signal searches and propose basic improvements for a future search program.

In its construction, this dissertation consists of six chapters. Chapter 2 (*Theoretical Overview*) provides an introduction to the current status of

the particle physics and lays the foundations to understand the motivation behind the original work presented in the later chapters. Chapter 3 (*Experimental Apparatus*) briefly discusses the Tevatron proton antiproton accelerator and the DØ detector which are used as the primary apparatus in our study. Chapter 4 (*Offline Event Reconstruction at DØ*) describes the primary methods of particle reconstruction used in DØ and provides quantitative measurements for the performance related to muon and jet reconstructions. This chapter also provides a discussion of the b-tagging methods which form the central analysis tools used in our study for the identification of b-jets. After these general introductory chapters, we present the first study of the b-jets produced in association with Z bosons at the DØ detector. Chapter 5 (*Production of Z + b-jet in Dimuon Channel*) presents the measurement of the ratio of cross sections for inclusive $Z+b$-jet process to inclusive Z+jet processes in the dimuon decay channel of the Z boson. Besides the techniques used for the measurement of this physical quantity and the corresponding uncertainties, this chapter provides a detailed account of how the associated backgrounds are measured and a pseudo-independent means of cross-checking the validity of the b-tagging methods used in this measurement. We also shortly decribe the similar analysis in the dielectron channel in Chapter 6 (*Dimuon and Dielectron Channel Combination*) and combine the two individual measurements into a single result. A comparison between the next-to-leading order QCD calculations and our combined measurement is presented in this chapter as well. Finally, in the last chapter, Chapter 7 (*Outlook for $Z+b\bar{b}$ Cross Section Measurement*), we perform an optimization study for the search of $Z + b\bar{b}$ signal for future studies at DØ .

Physical quantities presented in this thesis follow a convention often employed in high energy physics. Due to their frequent occurence in the units, we prefer adopting the system of units in which $\hbar = c = 1$, unless noted otherwise. Therefore the energy, momentum and the mass of the particles are all presented in the same unit, often selected as GeV (1 GeV $= 1 \times 10^9$ eV or 1 GeV $= 1.60219 \times 10^{-10}$ J).

Chapter 2

Theoretical Overview

This chapter presents a basic overview of the framework, the so called Standard Model, that describes our current understanding of matter particles and interactions between them. An interested reader is directed to several excellent and extensive resources on the same account [2], [3] and [4] for more rigorous understanding.

2.1 Standard Model of Particle Physics

In the early 20^{th} century, our understanding of the fundamental constituents of matter was made up of a set of a few particles like the proton, neutron, and the electron together with the electromagnetic field carrier particle called the photon. During the same period, two groundbreaking theoretical achievements, special relativity and quantum mechanics, were also developed which formed the basis of contemporary particle physics.

Our current understanding of the fundamental building blocks of matter as well as the existing interactions is more complete and integrated in a

framework which is called the Standard Model. In the Standard Model, all matter is composed of fundamental spin-1/2 particles called the *quarks*, that carry fractional electric charges ($\pm 2/3$ e and $\pm 1/3$ e) and *leptons*, that carry electric charges of $\pm 1e$ (e.g. electron) or zero (e.g. neutrinos). Protons and neutrons, the fundamental particles of the early 20^{th} century, are now known to be composite particles each containing three *valence* quarks of different flavors.

The interactions between these matter particles are also described by the Standard Model. Apart from gravity which is neglected due to its very weak strength and not yet incorporated into the Standard Model, the forces responsible for the interactions between the particles are electromagnetic as well as the weak and strong nuclear forces. As a consequence of the quantum nature of the universe, the energy is carried by discrete quanta that are identified as particles which transmit the corresponding force. This quantum nature of fields was originally proved to be true for photons and thus for electromagnetic fields via photo-electric effect and Compton scattering. We also know today that there exist $W^{\pm}/Z^{0}$ particles and *gluons*, all *bosons* obeying Bose-Einstein statistics, which transmit the weak and strong nuclear forces respectively.

2.1.1 Particles

The particles can be considered in two categories, the particles that make the matter and those that transmit forces or interactions. In this section, we will only review the matter particles and leave the discussion of the field particles for the next section. The matter particles are divided into two major

Leptons spin = 1/2		
Flavor	Mass GeV/c^2	Electric charge
ν_e electron neutrino	$<1\times10^{-8}$	0
e electron	0.000511	−1
ν_μ muon neutrino	<0.0002	0
μ muon	0.106	−1
ν_τ tau neutrino	<0.02	0
τ tau	1.7771	−1

Quarks spin = 1/2		
Flavor	Approx. Mass GeV/c^2	Electric charge
u up	0.003	2/3
d down	0.006	−1/3
c charm	1.3	2/3
s strange	0.1	−1/3
t top	175	2/3
b bottom	4.3	−1/3

Figure 2.1: Properties of fermion particles, quarks and leptons, adapted from [5]. These particles are all accompanied with corresponding anti-particles not shown separately.

categories called quarks and leptons and their properties are summarized in Fig. 2.1.

A quark is a spin-1/2 fermion which carries fractional electric charge as well as the color charge of the Quantum Chromo-Dynamics (QCD) which we will review later. There are only six observed species of quarks (also called flavors) along with their anti-particles. These quarks are called *up*, *down*, *charm*, *strange*, *bottom* and *top*. While most of the mass of all the elements in the universe is due only to the up and down type quarks as well as the QCD binding energy between them (since they make the protons and neutrons), other types of quarks are created in high energy cosmic ray showers or artificially in high energy particle collisions.

One fascinating characteristic of quarks is that they can not be observed in isolation. When separated from a bound state, the force required to free the quark from this state becomes very large due to the fact that the interec-

tion strength increases with distance and therefore decreases with momentum transfer. Understanding of this feature, which is called the asymptotic freedom, has led to 2004 Nobel Prize in Physics [6], [7]. When large amount of energy is introduced to separate the quark from its bound state (as in high energy hadron collisions), a series of quark and antiquark pairs are produced which then form new bound states.

Bound states of quarks are called *hadrons* and these strongly interacting particles are built from two different quark combinations. *Baryons* are hadrons of three quark bound states (e.g. QQQ) and protons and neutrons are most common examples of such particles with up-up-down and up-down-down quark combinations respectively. *Mesons* are hadrons of paired quark-antiquark combinations (e.g. $Q\bar{Q}$); pions ($\pi^{0,\pm}$) and kaons (K^0, $\bar{K^0}$ and $K^{\pm}$) are the most commonly produced mesons.

Leptons are also spin-1/2 fermions with integral electric charges, 0 or $\pm$ e as seen in Fig. 2.1. The neutral leptons are called *neutrinos*[1] (v_e, v_μ and v_τ) and their existence was first predicted by Wolfgang Pauli to account for the imbalance in the momentum and energy in certain radioactive decays. Charged leptons are *electrons* ($e^{\pm}$), which exist in all atoms, *muons* ($\mu^{\pm}$) which were first observed in cosmic rays and *tau* leptons ($\tau^{\pm}$) which were discovered in high energy experiments. Apart from their mass, the last two charged leptons have similar characteristics as the electron.

Each charged lepton and its corresponding neutrino form a flavor pair which is conserved in particle reactions excluding recent findings of neutrino oscillations. For example, when a muon decays to an electron, a muon neutrino as well as an electron neutrino is created:

[1]Meaning "the little neutral one".

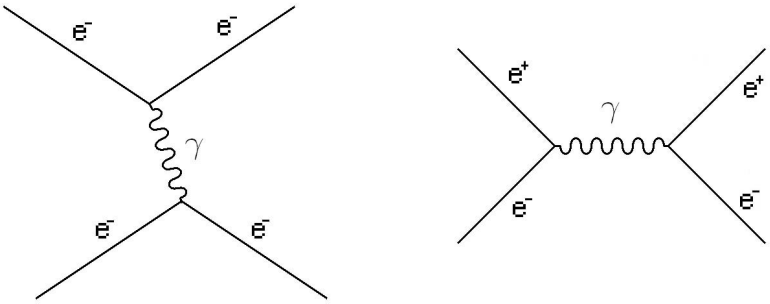

Figure 2.2: Feynman diagrams showing the exchange of photon between the two electrons. The diagram on the left shows the electron scattering process whereas the diagram on the right shows the electron annihilation followed by an electron-positron pair production.

$$\mu^- \rightarrow e^- + \bar{v}_e + v_\mu$$

2.1.2 Interactions

The combination of quantum mechanics and relativity gives rise to the introduction of quantum fields and the associated quanta of these fields. In a quantum field theory, the particle interactions are interpreted as the exchange of field particles. For example, the classical Coulomb force between two charged particles can be thought as an exchange of photons. A charged particle emits a photon and recoils; the emitted photon is absorbed by another charged particle, which changes its motion as a result. The Feynman diagram for such an interaction is shown in Fig. 2.2.

There are four fundamental forces, and their basic properties are listed in Fig. 2.3.

A quantum field theory for gravity has not yet been devised and hence

Property \ Interaction	Gravitational	Weak (Electroweak)	Electromagnetic (Electroweak)	Strong: Fundamental	Strong: Residual
Acts on:	Mass – Energy	Flavor	Electric Charge	Color Charge	See Residual Strong Interaction Note
Particles experiencing:	All	Quarks, Leptons	Electrically charged	Quarks, Gluons	Hadrons
Particles mediating:	Graviton (not yet observed)	W^+ W^- Z^0	γ	Gluons	Mesons
Strength relative to electromag for two u quarks at: 10^{-18} m	10^{-41}	0.8	1	25	Not applicable to quarks
Strength relative to electromag for two u quarks at: 3×10^{-17} m	10^{-41}	10^{-4}	1	60	
for two protons in nucleus	10^{-36}	10^{-7}	1	Not applicable to hadrons	20

Figure 2.3: Types of fundamental forces in nature and some of their properties, adapted from [5].

currently is not included in the Standard Model. However, electromagnetic, weak nuclear and strong nuclear forces are incorporated into the framework of the Standard Model through electroweak theory and quantum chromodynamics respectively.

Electromagnetic Interactions

Electromagnetic interactions take place between the charged particles and the field carrier photons with strength determined by the dimensionless fine-structure constant, α (Eq. 2.1).

$$\alpha = \frac{e^2}{\hbar c} \simeq \frac{1}{137} \tag{2.1}$$

The field theory describing the electromagnetic interactions and used to calculate cross-sections for these processes is called quantum electrodynamics (QED). An important feature of QED is that the theory is said to be renormalizable. To explain this with an example, we can describe an electron constantly emitting and re-absorbing virtual photons. These processes contribute to the mass of the electron and such divergences ultimately lead to the calculation of infinitely large electron mass. However, it is shown that

these divergences can be contained within mass and charge terms in the calculations and hence a new normalization for these quantities can be defined. The new definitions are replaced with their experimentally determined values and thus the QED calculations yield finite predictions for cross-sections when presented in terms of the physical quantities (like the mass of electron). This technique is called renormalization.

Another important property of electromagnetic interactions is that of gauge invariance. Gauge invariance simply refers to the invariance of the field Lagrangian under groups of unitary transformations denoted by U(1) and SU(n) for $n > 1$ where n is the dimensionality of the gauge charge space. QED is a U(1) type theory which means that the QED Lagrangian stays constant when the charged particle wave function undergoes an arbitrary phase change accompanied by a suitable change in the photon field as shown in Eq. 2.2. This invariance leads to the conservation of electric charge and currents.

$$\psi(x) \rightarrow e^{iq\lambda(x)}\psi(x) \tag{2.2}$$

Weak Interactions

The weak interactions occur among quarks and leptons. The most commonly known process involving weak interactions is the beta decay of a neutron:

$$n \rightarrow p + e^{-} + \bar{v}_e$$

The weak interactions are mediated by massive bosons $W^{\pm}$ and Z^0 as shown in Fig. 2.4. The masses of $W^{\pm}$ and Z^0 bosons are measured experimentally to be 80.425 ± 0.033 GeV and 91.1876 ± 0.0021 GeV respectively [8].

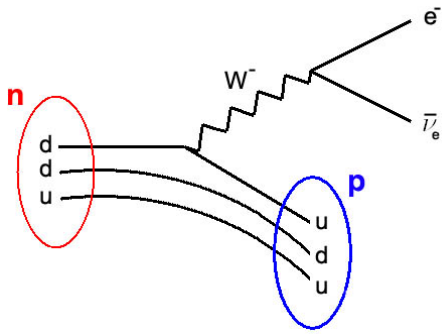

Figure 2.4: Feynman diagram showing the weak decay of neutron to proton accompanied by the emission of W^- boson which decays to an electron and electron-neutrino in a very short timescale.

Exchange of $W^{\pm}$ bosons results in the change of the charge of the lepton as well as the quark and is called a "charged-current" reaction while Z^0 boson exchanges do not cause any change in the electric charges and hence called "neutral-current" reactions.

The quantum field theory which describes the weak interactions was first outlined in 1967-8 by Glashow, Salam and Weinberg (GSW) and brought about the unification of the weak forces and electromagnetic interactions [9]. By replacing the U(1) group of quantum electrodynamics, GSW introduced the unification of weak interactions with electromagnetism via the introduction of more complex SU(2)×U(1) transformations.

Local gauge invariance under SU(2) group transformations requires the introduction of three massless spin-1 gauge bosons W^+, W^- and W^0. The conserved charge is called the weak isospin and the fermions are arranged into weak isospin doublets. To account for the experimental observations of Z^0 boson and the photon, the SU(2) symmetry group is combined with U(1) bringing in another gauge boson called B^0. The gauge invariance of this new

combination leads to the conservation of the so-called *weak-hypercharge* which is a combination of weak isospin and electric charge. In order to give the two observed bosons, the weak eigenstates of W^0 and B^0 are mixed leading to the orthogonal combinations of photon and Z^0 as shown in Eq. 2.3 and 2.4.

$$\gamma = W^0 \sin\theta_W + B^0 \cos\theta_W \tag{2.3}$$

$$Z^0 = W^0 \cos\theta_W - B^0 \sin\theta_W \tag{2.4}$$

where θ_W is the weak mixing angle, a parameter of the electroweak theory.

Strong Interactions

Strong interactions take place between the constituent quarks which make up the hadrons. The mediating particles of the strong force are called *gluons*. Quantum chromodynamics, which describes the strong nuclear forces, introduces a new internal degree of freedom called *color*. Figuratively speaking, each quark is supposed to have one of the three possible colors; red, blue or green. Anti-quarks have the anti-colors: anti-red, anti-blue and anti-green. Gluons carry two labels at one time, one color and an anti-color label such that the color is conserved at each interaction. For example, a red quark can turn into a blue quark by emitting a red-antiblue gluon which would conserve the net color. Leptons and the EW bosons are all colorless particles and therefore do not interact via strong forces.

Quantum chromodynamics describes the strong interactions in terms of an SU(3)[2] gauge invariance and this leads to the existence of 8 gauge bosons

[2]Three refers to the three colors in QCD

corresponding to different two-color combinations of 8 gluons. Due to the fact that two gluons can have color charges, they can interact with each other, a situation not observed with neutral electroweak bosons such as photons.

The most striking feature of the quantum chromodynamics is that it requires all the isolated particles to be *colorless* i.e. a combination of red-green-blue quarks or color-anticolor pairs. This leads to the known particles of three quark baryonic states and two quark meson states. Color confinement requires that when a quark is separated from its bound state, the extra energy is turned into a quark-antiquark pair and new hadrons are created. Breaking a hadron is therefore something similar to breaking a bar magnet where the broken pieces are not separately N or S poles but rather individual magnets of both N and S poles.

Due to the color confinement, quarks and gluons are experimentally observed as a *jet* of colorless particles. In a collision with sufficient momentum transfer, the hadron collisions can be considered to be occuring between the incoming quarks or gluons which are collectively called *partons* to indicate a constituent of a hadron. Fig. 2.5 shows the schematic diagram for such a collision where the two partons fuse to create a virtual gluon which then splits into a quark-antiquark pair.

Since the quarks can not roam freely in isolation, color confinement requires the production of colorless and stable hadrons. This process of *hadronization* results in a *jet* of colorless particles which live long enough to be detected in the detector with a total momentum nearly equal to that of the initial parton.

The probability to observe a specific flavor parton with a given momentum

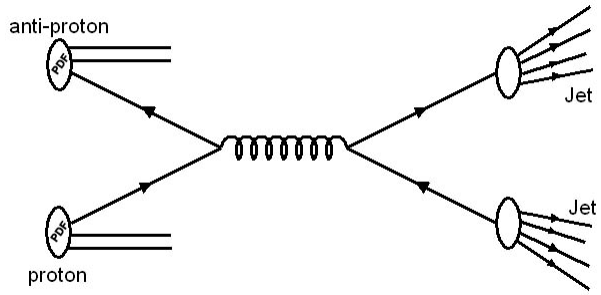

Figure 2.5: A schematic diagram showing the leading order proton-antiproton interaction resulting in the production of two jets.

inside a hadron is often presented with the parton distribution functions (PDF). PDF's, specific to each hadron and are parametrized as a function of fractional parton momentum within the hadron, denoted x, and defined as in Eq. 2.5. A recent PDF set obtained from experimental data is shown in Fig. 2.6, where

$$x \equiv \frac{|\vec{p}_{\text{parton}}|}{|\vec{p}_{\text{hadron}}|} \tag{2.5}$$

Since the proton is composed of two up quarks and one down quark, by definition;

$$\int_0^1 u_v(x)dx = 2 \tag{2.6}$$

and

$$\int_0^1 d_v(x)dx = 1 \tag{2.7}$$

As Fig. 2.6 shows, there is also non-zero probability of observing other partons in the proton produced as virtual quark pairs. These quarks are

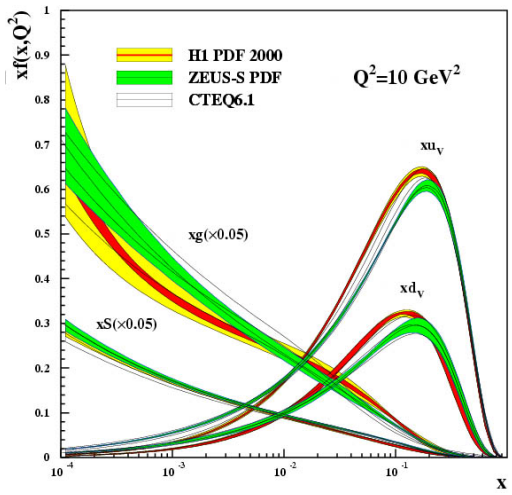

Figure 2.6: Parton distribution functions with error bands in $xf(x)$ standard form obtained from deep inelastic scattering experiments. PDF for *valence* up and down quarks as well as gluon and strange quarks are shown, [10]. Refer to the text for description.

called *sea* quarks and differ from the constituent two up and down quarks which are called *valence* and denoted with subscript v in Eq. 2.6 and 2.7. In summary, the proton is composed of three valence quarks, a sea of quark-antiquark pairs which are created and annihilated continuously, and finally a collection of gluons which hold all the quarks together as indicated schematically in Fig. 2.7.

2.2 Electro-Weak Symmetry Breaking

The existence of force carriers and interactions follows from the gauge invariance principle which requires that the Lagrangian of matter fields is invariant under gauge transformations. Choosing a particular gauge transformation leads to a specific type of interaction and this can simply be illustrated for

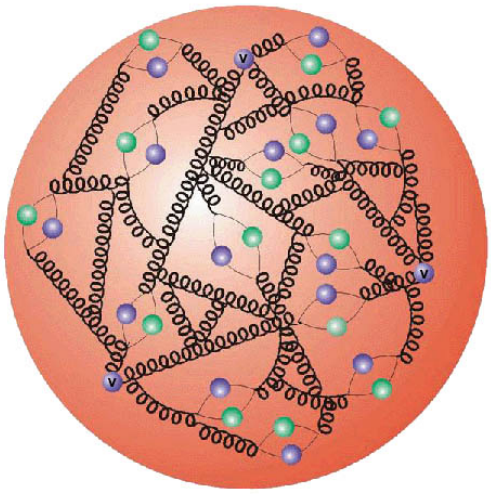

Figure 2.7: An artist's view of inside of the proton. Three valence quarks are marked with the letter v.

electromagnetic interactions.

The Lagrangian shown in Eq. 2.8 is not invariant under U(1) gauge transformation in Eq. 2.9. The new Lagrangian under this gauge transformation becomes Eq. 2.10.

$$\mathcal{L} = i\bar{\psi}\gamma^{\mu}\partial_{\mu}\psi - m\bar{\psi}\psi \tag{2.8}$$

$$\psi(x) \rightarrow \psi'(x) \equiv e^{-iq\lambda(x)}\psi(x) \tag{2.9}$$

$$\mathcal{L}' = \mathcal{L} + (q\bar{\psi}\gamma^{\mu}\psi)\partial_{\mu}\lambda(x) \tag{2.10}$$

However, when we introduce an extra field A_{μ} which transforms as $A_{\mu} \rightarrow A'_{\mu} \equiv A_{\mu} + \partial_{\mu}\lambda(x)$, then the Lagrangian in Eq. 2.10 becomes:

$$\mathcal{L}' = i\bar{\psi}\gamma^{\mu}\partial_{\mu}\psi - m\bar{\psi}\psi - (q\bar{\psi}\gamma^{\mu}\psi)A_{\mu} \tag{2.11}$$

and the gauge invariance is preserved [4]. The extra term added introduces the interaction between fermions and a massless gauge boson which is the photon field of electromagnetic interaction. Other interactions can also be derived in a similar manner by applying other gauge transformations.

After this example of the gauge invariance principle, we can observe the spontaneous symmetry breaking through a simple mathematical formalism. For this purpose, we follow the introductory presentation used in [2]. We start by considering the Lagrangian of a scalar field ϕ in the following form:

$$\mathcal{L} = \frac{1}{2}(\partial_\mu \phi)(\partial^\mu \phi) - V(\phi) \tag{2.12}$$

If the effective vacuum potential, $V(\phi)$, is an even function of the scalar field ϕ,

$$V(\phi) = V(-\phi) \tag{2.13}$$

then the Lagrangian in Eq. 2.12 is invariant under a simple parity transformation:

$$\phi \rightarrow -\phi \tag{2.14}$$

A general potential can be written as in Eq. 2.15 to ensure bounded oscillations about the vacuum state and renormalizable theory.

$$V(\phi) = \frac{1}{2}\mu^2\phi^2 + \frac{1}{4}|\lambda|\phi^4 \tag{2.15}$$

The state of lowest energy applies to the minima of the effective potential $V(\phi)$. If the parameter μ^2 is positive then the minimum of the potential occurs for:

$$< \phi >_0 = 0 \tag{2.16}$$

The Lagrangian for the study of the small oscillations around this minimum is unchanged from the original Lagrangian and the original symmetry with respect to the parity transformation is maintained. However if $\mu^2 < 0$, the potential becomes:

$$V(\phi) = -\frac{1}{2}|\mu^2|\phi^2 + \frac{1}{4}|\lambda|\phi^4 \tag{2.17}$$

which has a minimum at:

$$< \phi >_0 = \pm\sqrt{\frac{-\mu^2}{|\lambda|}} \equiv \pm v \tag{2.18}$$

Thus, the minima of the potential correspond to two degenerate vacuum states. In order to show that the choice of either ground states leads to the breaking of the original Lagrangian symmetry, we consider the oscillations about $< \phi >_0 = +v$ and define a shifted field about this ground state:

$$\phi' = \phi - v \tag{2.19}$$

In the new representation, the ground states corresponds to $< \phi' >_0 = 0$ and the transformed Lagrangian becomes:

$$\mathcal{L} = \frac{1}{2}(\partial_\mu \phi')(\partial^\mu \phi') - |\mu^2|\Big(\frac{\phi'^4}{4v^2} + \frac{\phi'^3}{v} + \phi'^2 - \frac{v^2}{4}\Big) \tag{2.20}$$

which does not respect the symmetries of the original Lagrangian. This phenomenon of vacuum state not sharing the symmetry of the Lagrangian is called the *spontaneous symmetry breaking*. It is called *spontaneous* since no external agency is responsible for breaking the symmetry; unlike the agent of gravity which breaks the symmetry of up and down directions as opposed to the unbroken symmetry observed in left and right directions.

Furthermore, the Lagrangian for small oscillations about the vacuum yields:

$$\mathcal{L}_{\text{S.O.}} = \frac{1}{2}(\partial_\mu \phi')(\partial^\mu \phi') - |\mu^2|\phi'^2 \tag{2.21}$$

which is the Dirac Lagrangian of small oscillations for a particle with mass equal to $\sqrt{}(2|\mu^2|)$.

Besides the discrete symmetries, the same phenomenon can also be observed in continuous symmetries like the rotation or SO(2) group transformations. In this case, the Lagrangian for two scalar fields ϕ_1 and ϕ_2 can be written as in Eq. 2.22.

$$\mathcal{L} = \frac{1}{2}\Big[(\partial_\mu \phi_1)(\partial^\mu \phi_1) + (\partial_\mu \phi_2)(\partial^\mu \phi_2)\Big] - V(\phi_1^2 + \phi_2^2) \tag{2.22}$$

The Lagrangian is invariant under rotations in two dimensions:

$$\phi = \begin{pmatrix} \phi_1 \\ \phi_2 \end{pmatrix} \rightarrow \begin{pmatrix} \cos\theta & \sin\theta \\ -\sin\theta & \cos\theta \end{pmatrix} \begin{pmatrix} \phi_1 \\ \phi_2 \end{pmatrix} \tag{2.23}$$

Considering the similar potential as in Eq. 2.17 and replacing the field by ϕ, we quickly observe that positive μ^2 corresponds to the symmetry conserving vacuum state $< \phi >_0 = (0, 0)$. However, the choice of negative μ^2 yields to spontaneous breaking of the symmetry since the absolute minima occurs at:

$$< \phi^2 >_0 = \frac{-\mu^2}{|\lambda|} \equiv v^2 \tag{2.24}$$

which corresponds to a continuous selection of distinct vacuum states. If we select the simple physical vacuum state of $< \phi_0 >= (v, 0)$ then we can again describe the small oscillations about this state by a transformed field:

$$\phi' = \phi - < \phi_0 > \equiv \begin{pmatrix} \eta \\ \zeta \end{pmatrix} \tag{2.25}$$

again yielding a small oscillation Lagrangian of

$$\mathcal{L}_{\text{S.O.}} = \frac{1}{2}\Big[(\partial_\mu \eta)(\partial^\mu \eta) + 2\mu^2\eta^2\Big] + \frac{1}{2}\Big[(\partial_\mu \zeta)(\partial^\mu \zeta)\Big] + \text{const.} \tag{2.26}$$

Eq. 2.26 represents the Dirac Lagrangian of two particles in the spectrum. The η-particle which is associated with the radial oscillations has a mass of $\sqrt{2|\mu^2|}$. However, the ζ-particle is massless. The existence of the two particles is a direct consequence of the transformation we used and the massless particle is referred as a *Goldstone* boson [2].

In the presence of the massless vector field, A_μ, the corresponding Lagrangian of the small oscillations take the form in Eq. 2.27 [2].

$$\mathcal{L}_{\text{S.O.}} = \frac{1}{2}\Big[(\partial_\mu \eta)(\partial^\mu \eta) + 2\mu^2\eta^2\Big] - \frac{1}{4}F_{\mu\nu}F^{\mu\nu} + \frac{q^2v^2}{2}A'_\mu A'^\mu + \text{const.} \tag{2.27}$$

where $F_{\mu\nu} = \partial_\nu A_\mu - \partial_\mu A_\nu$ and $A'_\mu = A_\mu - \partial_\mu \lambda(x)$. The non-zero vacuum expectation value of the field breaks the SU(2)×U(1) symmetry of the electroweak theory and the particle spectrum corresponding to this Lagrangian consists of

- an η-field of mass equal to $\sqrt{-2\mu^2}$ ($\mu^2 < 0$).
- a massive vector field A'_μ, with mass equal to qv.
- no ζ-field

After spontaneous symmetry breaking, the massless Goldstone boson (ζ-particle) is absorbed in a massive vector field in the presence of A_μ. This is the process which gives the $W^\pm$ and Z^0 bosons their observed masses and the

remaining massive scalar η, is known as the Higgs boson [11]. The vacuum expectation value for the Higgs boson field (v) can be expressed in terms of the Fermi coupling constant as in Eq. 2.28 [12].

$$v = \frac{1}{\sqrt{2}G_F} \simeq 246 \text{ GeV} \tag{2.28}$$

2.2.1 Phenomenology of Higgs Boson

Although the theoretical formalism presented above gives a good description of the massive electroweak bosons, it also introduces a massive, spin-0 particle called Higgs boson. For this description to be fully accepted, the existence of the Higgs boson must experimentally be observed. Despite the prediction of such a particle, the theory does not provide a direct estimate of what the mass of this particle should be.

Nevertheless, the standard model provides clues to the likely mass of Higgs boson. One of the constraints on the mass of the Higgs boson is obtained by requiring that current electroweak theory is valid and no new physics intervenes up to a cutoff scale Λ. This is called the *triviality* bound and it yields a range of upper and lower bounds for the possible Higgs masses as a function of the cutoff energy limit as shown in Fig. 2.8. The triviality condition requires that if the electroweak theory is the effective field theory up to the Planck scale ($\sim 10^{19}$ GeV), the Higgs boson mass must not be lower than 130 GeV and not exceed 180 GeV [15]. For other cutoff energies, other ranges of Higgs boson masses are allowed. Alternatively if the Higgs boson is found with a mass of lower than 130 GeV , then it is likely that the hints of new physics should be observed below the Plack scale.

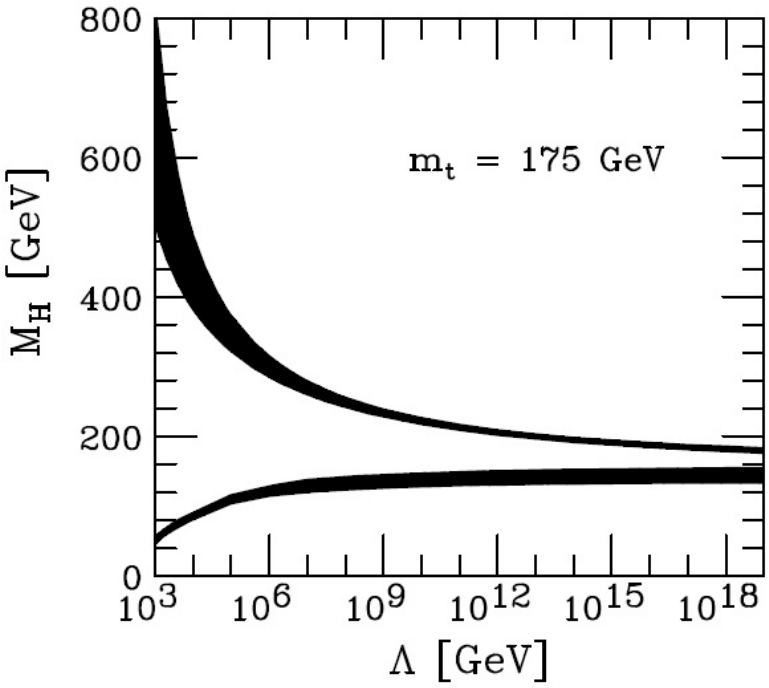

Figure 2.8: The lower and upper Higgs mass bounds as a function of the energy scale Λ at which the Standard Model breaks down, assuming $M_t = 175$ GeV and $\alpha_s(m_Z) = 0.118$. The shaded areas reflect the theoretical uncertainties in the calculations of the Higgs mass bounds, adapted from [13] and [14].

Precision electroweak measurements are also sensitive to the Higgs boson mass through radiative corrections. The effect of some of the experimentally known precision data is used to put constraints on the Higgs boson mass by the LEP Electroweak Working Group [16] in the context of SM and their fit is shown in Fig. 2.9. The yellow-colored band covering the lower regions of the possible Higgs boson masses is obtained through direct searches at LEP, and the 95 % confidence level (C.L.) lower limit due to the non-observation of the Higgs is set at 114.4 GeV [17]. Fig. 2.10 shows the possible values of the Higgs boson mass as a function of the W boson and top quark masses,

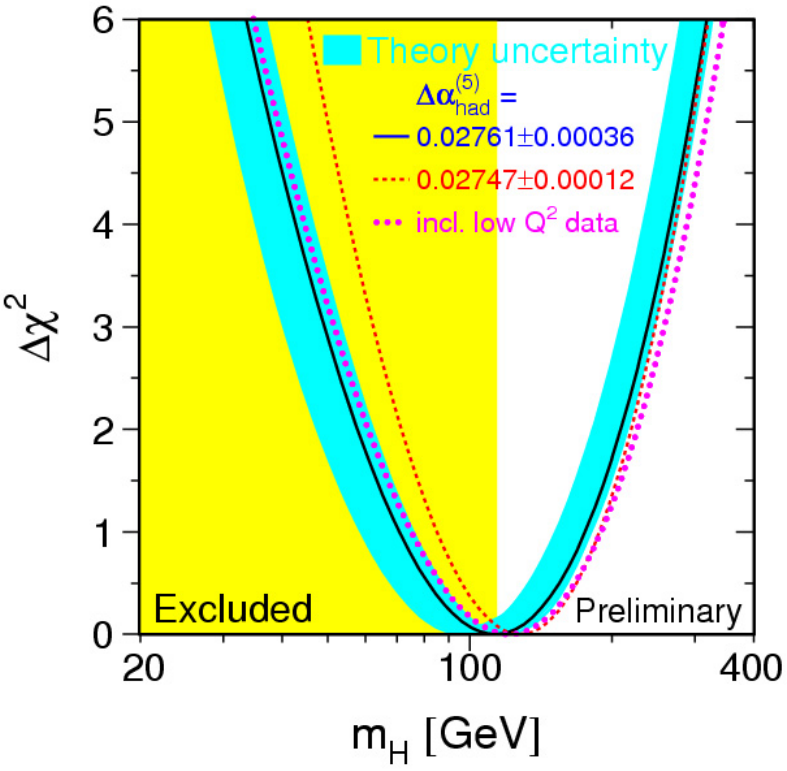

Figure 2.9: Goodness of the electroweak precision data fit ($\Delta\chi^2 \equiv \chi^2 - \chi^2_{\rm min}$) versus the mass of the Higgs boson (m_H). The line shows the fit using all available data and the band shows the estimate of the theoretical uncertainty. The yellow vertical band covering the low mass regions shows the 95 % C.L. exclusion limit on the mass of the Higgs boson from direct searches at LEP, adapted from [16].

again in the context of the SM.

In the Tevatron collider at Fermilab, with proton-antiproton collisions of center of mass energy near 2 TeV, the dominant channel of a light Higgs boson production occurs via gluon fusion, $gg \rightarrow h_{\rm SM}$ and Higgs decays mainly to a pair of b-quarks. However due to overwhelming QCD dijet background, this channel does not provide sufficient discrimination for the discovery of the relatively small Higgs signal. The SM Higgs boson production channels at

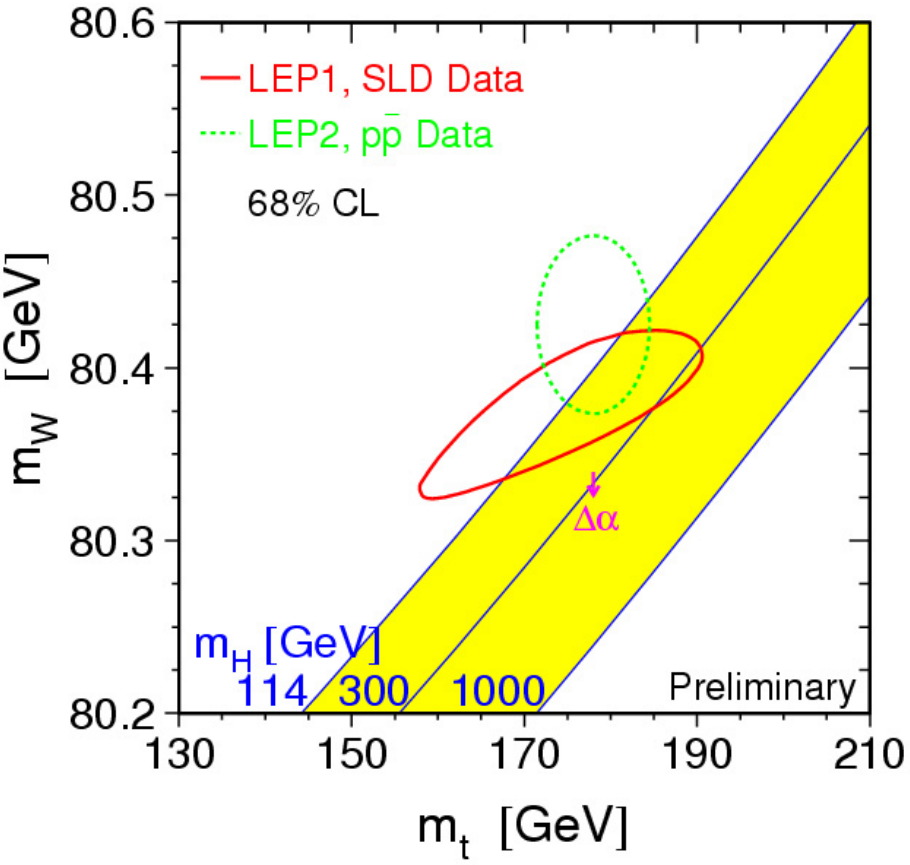

Figure 2.10: Regions of allowed Higgs boson mass consistent with the measurements for the mass of the W boson and the top quark. The red solid circle shows the limit from the indirect measurements of LEP-I and SLD and the green dashed circle shows the direct measurements from proton-antiproton colliders and LEP-II experiments. In both cases the 68 % C.L. curves are plotted, adapted from [16].

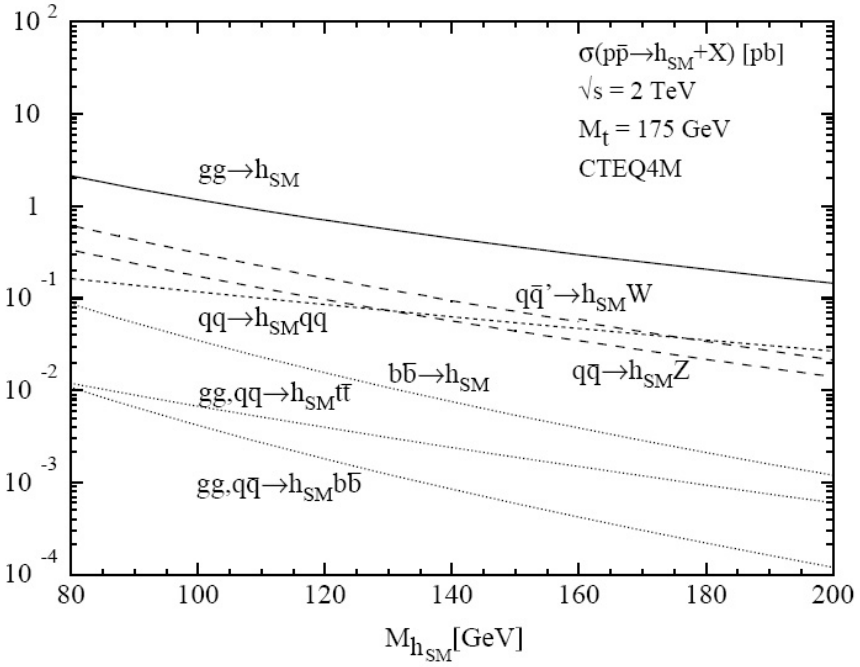

Figure 2.11: Higgs production cross-sections (in units of pb) at 2 TeV proton-antiproton collisions at Tevatron.

Tevatron are shown in Fig. 2.11 with the expected production cross-sections, [13].

The next-to-largest cross-section production channels for a light Higgs boson are the so-called Higgs-strahlung processes where the original quark and anti-quark pairs from the colliding hadrons fuse to create a virtual electroweak boson (W^* or Z^*) which later decays into a real electroweak boson and a Higgs boson. The diagram for this process is shown in Fig. 2.12. These vector boson associated production processes are more easily separated from background than the gluon fusion channel since the leptonic decay channels of the vector bosons can be exploited to significantly reduce the multijet background.

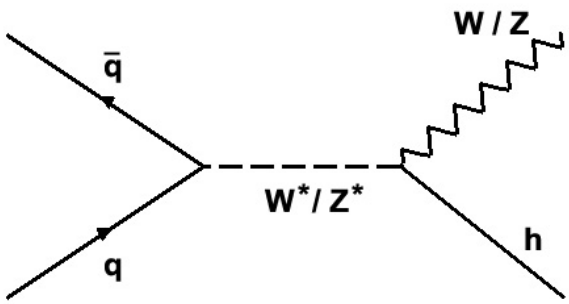

Figure 2.12: The associated production of Standard Model Higgs boson with a vector boson. The $q\bar{q}$ pair refers to different flavors of quarks for the associated production with W bosons (like $u\bar{d}$) and same flavor of quarks for the associated production with Z bosons (like $u\bar{u}$).

The main decay channels of a Standard Model Higgs boson are also shown in Fig. 2.13. Since the Higgs boson coupling to other Standard Model particles increase with the particle masses, it is natural to expect that a light Higgs decays mainly to a pair of b quarks, the heaviest particles kinematically allowed for a light Higgs boson below 135 GeV . However if the Higgs boson is heavier, than decays to the real or virtual electroweak bosons become kinematically possible and these channels start to dominate for Higgs boson masses larger than 135 GeV .

2.3 Heavy Quark Production with Z Boson

In the previous section, we have discussed that the most promising channels to discover light Higgs boson at Tevatron are the associated production channels where the Higgs boson is produced with an accompanying W or Z

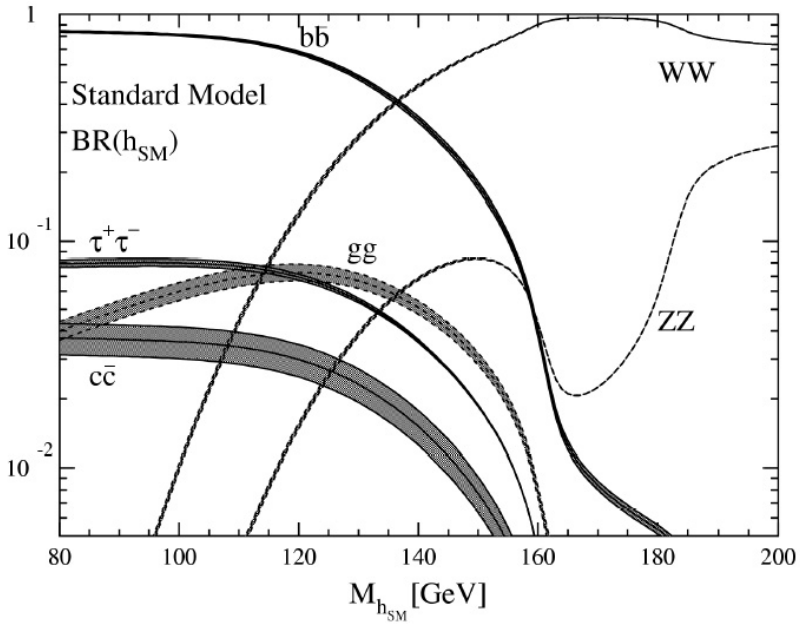

Figure 2.13: Branching ratios of the dominant decay modes of the Standard Model Higgs Boson obtained with the program HDECAY [18] including QCD corrections beyond the leading order. The shaded bands represents the effect of uncertainty in the input parameters like α_S, m_b and m_t.

boson. For the Higgs boson mass ranges below 135 GeV, the Higgs decays mainly to a b anti-b quark pair. We require that the vector boson can decay leptonically ($W^{\pm} \to \ell^{\pm}\bar{\nu}_{\ell}$ or $Z \to \ell\bar{\ell}$).

In this thesis, we concentrate on the production channels involving Z bosons where Z decays to a pair of muons ($Z \to \mu^+\mu^-$). The production cross-section for the Zh_{SM} production is about 0.07 pb for a Higgs mass of about 130 GeV [13]. The most important background for this channel is the QCD production of $b\bar{b}$ through gluon splitting in association with Z boson. The two final states are similar with signatures of two high momentum

leptons and two b-jets.

The most important tools for reducing the $Z + b\bar{b}$ background have been studied and possible multi-variate tools were proposed involving the dijet mass, jet momenta as well as other topological variables [19]. However before such a discrimination is possible, the $Z + b\bar{b}$ signal has to be observed at the Tevatron and production of heavy quarks in association with electroweak bosons must be studied. To date, there is no experimental study or measurement of this process and all our estimations rely on the theoretical next-to-leading order QCD calculations.

In the following chapters of this thesis, we study the inclusive production of the $Z + b$-jet production and develop the tools for optimal ways of measuring the $Z + b\bar{b}$ cross section. An extensive phenomenological study of this process at hadron colliders can also be found in reference [20].

Inclusive b-jet production has two major components;

- Scattering of the b quark present in the incoming beam hadron as a result of gluon splitting which occurs inside the proton. The gluon splitting inside the proton produces a pair of b quarks but only one of them undergoes hard scattering and detected as a heavy jet. The other b quark usually has a low momentum due to the low momentum of the initial gluon and gets lost in the beam remnant particles. Examples of such production are shown in Fig. 2.14 where only the scattered heavy quark is shown.

- Scattering of consituent light quarks inside the proton and creation of a gluon which subsequently decays to a pair of b quarks giving a two b-jet final state. There is also a significant chance of detecting this two b-jet

final state as a single b-jet event due to reconstruction efficiencies and kinematic acceptance. It is also possible that two jets can be very close to the each other and the reconstruction algorithms can reconstruct these jets as a single jet. Examples of the two b-jet production are shown in Fig. 2.15.

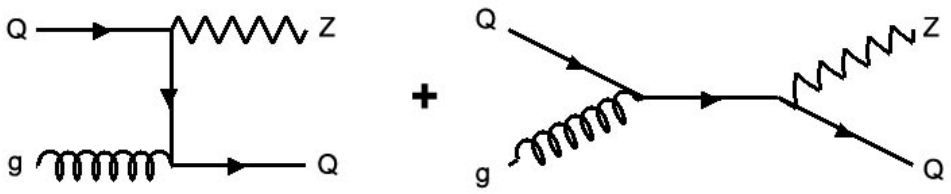

Figure 2.14: Associated production of a Z boson and a single high momentum heavy quark, $Qg \to ZQ$ ($Q = b$ or c).

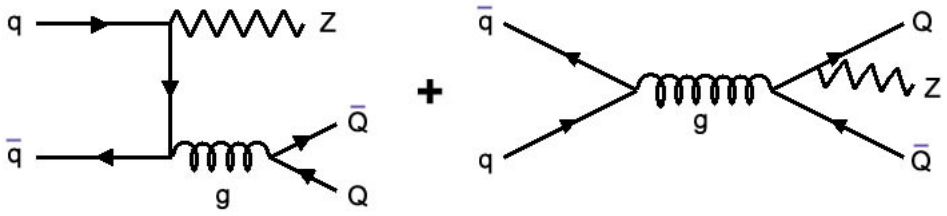

Figure 2.15: Associated production of a Z boson and a pair of heavy quarks, $q\bar{q} \to ZQ\bar{Q}$ ($Q = b$ or c). Both involve splitting a final state gluon but have Z radiated at different places.

The next-to-leading order calculations of cross sections for b-jets of transverse momentum[3] larger than 15 GeV and absolute pseudo-rapidity, $|\eta|$,

[3]Transverse momentum, $p_T \equiv |\vec{p}| \times \sin\theta$.

smaller than 2 are summarized in Table 2.1, [20]. For jet reconstruction a simple cone algorithm of radius 0.7 is assumed. In the case of two partons within a cone of radius 0.7, they are merged intoa single jet with four-momentum equal to the sum of the two partons' four-momenta. The kinematic cuts are applied after any merging is performed. For more detailed definitions of these quantities, the reader is referred to chapter 3.

In Table 2.1, ZQ refers to the final state of exactly one heavy quark; $Z(Q\bar{Q})$ refers to exactly one jet, which contains a merged heavy quark pair; ZQj refers to exactly two jets, one of which contains a heavy quark; $ZQ\bar{Q}$ refers to the final state of two jets, both of which contains a heavy quark. The meanings of Zj and Zjj follow similar convention. In the calculation of the ZQ cross section, the mass of the heavy quark is neglected in order to simplify the calculations. The error made by this approximation is proportional to $(m_Q/p_T^Q)^2$ and included in the uncertainty estimates [20]. The mass of the heavy quark is maintained throughout the $ZQ\bar{Q}$ calculations in order to regulate the divergences that would arise from a gluon splitting to massless collinear quarks.

In the last column of Table 2.1, inclusive next-to-leading order cross sections are provided for $Z + Q$ and $Z + QQ$. Only the inclusive $Z + Q$ cross-section calculations are reported with uncertainties due to the variations in the renormalization scale, factorization scale, and the parton distribution functions respectively [20].

In chapters 5 and 6, we show a measurement of the ratio of cross sections for the inclusive $Z + b$-jet to inclusive Z+jet processes. Being the first study of $Z + b$-jet production, this measurement has the importance of providing

	ZQ	$Z(Q\bar{Q})$	ZQj	$ZQ\bar{Q}$	ZQ inclusive
$gb \to Zb$	10.4	0.169	2.19	0.631	$13.4 \pm 0.9 \pm 0.8 \pm 0.8$
$q\bar{q} \to Zb\bar{b}$	3.32	1.92	—	1.59	6.83
$gc \to Zc$	16.5	0.130	3.22	0.49	$20.3^{+1.8}_{-1.5} \pm 0.1^{+1.3}_{-1.2}$
$q\bar{q} \to Zc\bar{c}$	5.66	6.45	—	1.70	13.8
	Zj		Zjj		Zj inclusive
$q\bar{q} \to Zg$ & $gq \to Zq$	870		137		$1010^{+44+9+7}_{-40-2-12}$

Table 2.1: Next-to-leading order cross sections (in units of pb) for Z boson production in association with heavy quark jets at the Tevatron [20]. No branching ratios are included. Refer to text for descriptions.

an experimental test of the QCD predictions provided in Table 2.1 and establishes an explicit confirmation of a related process to the most important background for Higgs searches.

In addition, this measurement provides another indirect benefit in that it provides experimental data to study the b quark density in the proton. The inclusive $Z + b$-jet production gets the largest contribution from the single b quark production where the final state b quark derives from the parton sea inside the incoming proton. Although our measurement does not make a clear distinction between initial state and final state b quark productions, our study could provide useful data for further studies of the heavy flavor content of the proton.

Chapter 3

Experimental Apparatus

In this chapter, we present an overview of the Fermilab Tevatron proton-antiproton collider and the DØ experiment that were utilized in the making of this study. Both the Tevatron collider and the DØ detector went through several upgrades in the course of their operation and the descriptions given in this chapter represent their current operating conditions. We note that future upgrades in these structures are also being planned and we will briefly discuss the motivations for future upgrades in this chapter as well.

3.1 Tevatron Accelerator Complex and Run II

With approximately 1 TeV [1] per particle beam energy, the Fermilab Tevatron collider is currently the highest energy particle accelerator operating in the world. Along the circumference of 4.26 miles, proton and anti-proton particle trains (series of bunches) are both accelerated and steered to create head-on collisions at two interaction points where two detectors, CDF and DØ are

[1] The nominal energy of the particles in the colliding bunches is 0.98 TeV.

placed to record these collisions. Therefore the Tevatron collider serves the purpose of both an accelerating synchrotron and a storage ring.

Using superconducting magnets and stochastic cooling technologies to prepare low emittance antiprotons, the Tevatron collider started its operations in 1983 with a beam energy of 512 GeV [21]. It was 1985 when the beam of particles reached the energy of 800 GeV and first collisions were observed at the Tevatron. A year later the beam energy was raised to 900 GeV with which Tevatron and the experiments started their 10 years of operation, a remarkable era in high energy physics that led to the discovery of the top quark in 1995.

Finally, with the replacement of Main Ring with the Main Injector, for injecting protons and anti-protons into the Tevatron, the Tevatron collider started its second phase of operation in March of 2002, called Run II, with considerably higher colliding particle flux [2] and about 10% higher beam energy. In this document, we will describe the state of the Tevatron collider during this phase. The physics results presented here are extracted from the collider data collected during this period as well.

The Fermilab Tevatron Accelerator is a very complex structure and the Tevatron ring itself is the last piece of a series of accelerating structures, as seen in Fig. 3.1, that are essential for a successful operation. More information on the technical details of the accelerator complex can be found in the references [22, 23]. However, we will briefly review the workings of the accelerator from the creation of individual particle beams to their collisions.

- **Ion Source and Pre-Accelerator**

[2] Or luminosity, which will be defined later in the text.

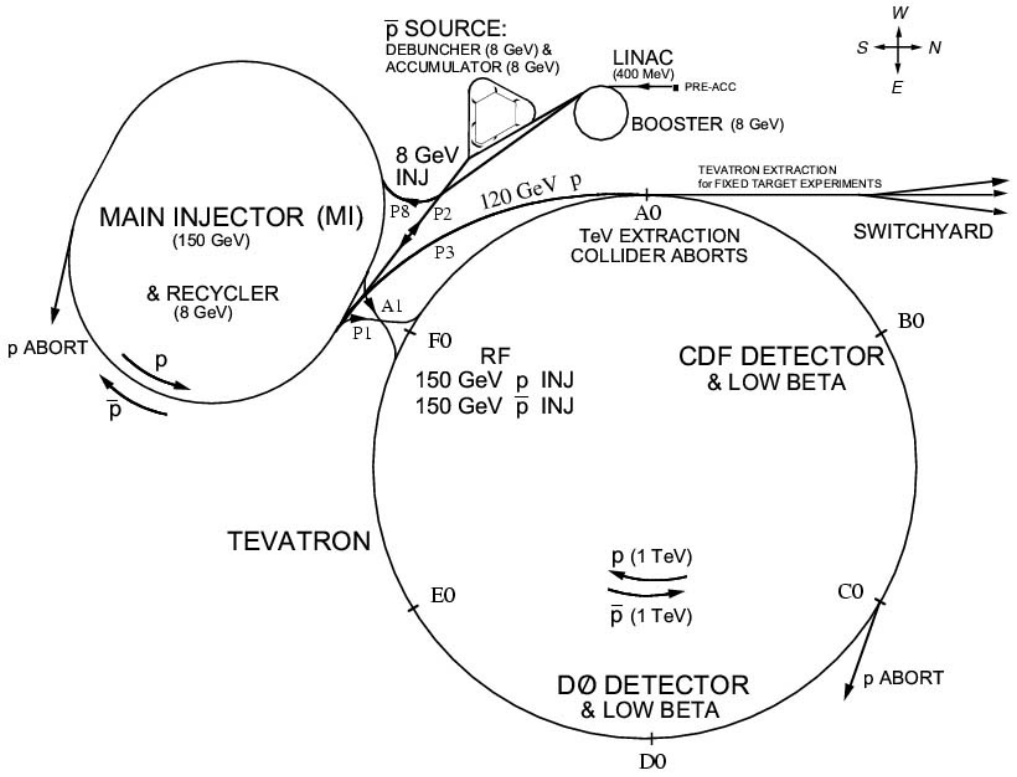

Figure 3.1: Schematic view of the Fermilab Accelerator Complex adapted from [24]. The several structures shown in this figure are drawn to approximate scales.

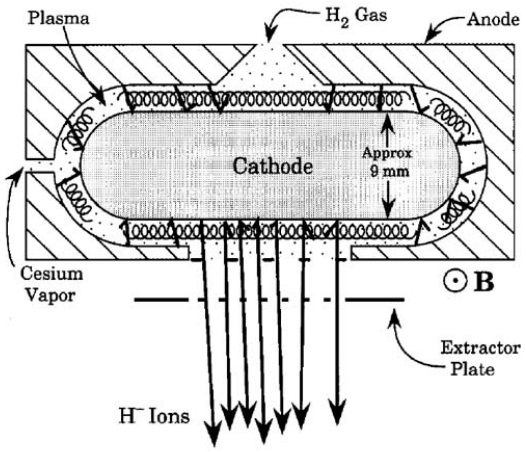

Figure 3.2: Schematic view of magnetron operation for the hydrogen ion source [26].

The accelerator chain starts at the pre-accelerator where the beam particles are in the form of negatively ionized hydrogen gas (H^-). These ions are produced using a magnetron surface-plasma source [25] and accelerated to a beam energy of 18 keV. A schematic view of magnetron operation is shown in Fig. 3.2. The hydrogen gas entering the magnetron is stripped of electrons by the electric field between the anode and the cathode surfaces. The positively charged hydrogen gas ions (or protons) strike the cathode and collect extra electrons absorbed on the surface. Only a small portion of these initial positive ions ($\sim$ 10 %) collect two electrons to become negative ions (H^-). The negative ions are extracted from the magnetron using an electric field of 18 kV applied by the extractor plate shown in Fig. 3.2.

Using a Cockcroft-Walton accelerator, 18 keV ions are accelerated through

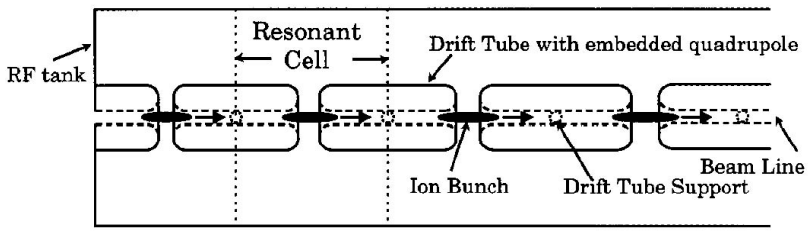

Figure 3.3: Schematic view of the linac tanks with concentric Alvarez-type drift tubes [26].

a 750 kV potential, attaining 750 keV net energy in the process [3]. After being accelerated to 750 keV, the beam is transferred to the Linac using one of the five transport lines which are used to connect several parts of the accelerator complex.

- **The Linac**

  The Fermilab Linear Accelerator (LINAC) is a 400 MeV hydrogen ion accelerator composed of two different types of acceleration structures. At the first stage, Alvarez-type drift tubes accelerate the ions up to 116 MeV operating at 201.25 MHz. This part of the linac is 79 m long and has 5 cylindrical steel tanks inside which 23 to 59 concentric drift tubes are suspended in the center. The second part of the Linac is called the side-coupled cavity Linac and operates in the same fashion as the drift-tube linac but with higher efficiency. This portion of the Linac is 67 m long with 7 side-coupled cavities operating at about 805 MHz.

[3] H^- ions have one proton and two electrons, giving 1 electron charge per ion. These ions gain 1 eV energy when accelerated through a potential of 1 V.

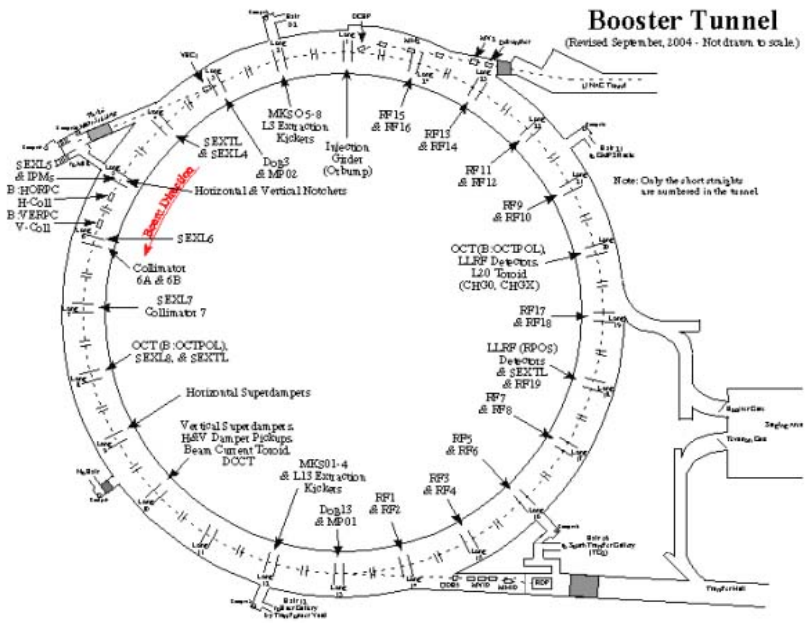

Figure 3.4: Schematic view of the Booster synchrotron.

Besides accelerating the hydrogen ions up to 400 MeV, the Linac also bunches the beam coming out of the pre-accelerator in pulses of 201.25 MHz rather than providing a continuous stream of particles.

- **The Booster**

  The Booster is a 75.47 m radius synchrotron ring and the first synchrotron accelerator in the accelerator chain (see Fig. 3.4). It accelerates the 400 MeV ions extracted from the Linac to a kinetic energy of 8 GeV through RF cavities and alternating gradient magnets [26, 27]. A typical pulse duration for injected beam is 10 turns in the synchroton ring.

  Before the injection to the Booster, a debuncher is used to reduce the

momentum spread of the beam (typically ∼0.3 %) that corresponds to a bunch length of approximately 8 mm in the Booster. The debuncher is a basic RF system which harmonizes the ions in the bunch by boosting the ions behind the beam (slow particles) and slowing down the ones ahead of the beam. After debunching, the hydrogen ions are passed through carbon foil layers which strip electrons from the ions and hence leaving only protons in the beam.

During the acceleration in the Booster, protons are kept in the same orbit by bending magnets with varying magnetic field strength (40 gauss at injection and 7000 gauss at extraction). The beam is accelerated by varying the RF frequency from 37.77 MHz at injection up to 52.81 MHz when they reach the kinetic energy of 8 GeV . This procedure of increasing the magnetic field strength and the RF frequency is the fundamental idea behind the sycnhrotron accelerators.

- **The Main Injector**

  The Fermilab Main Injector is a 150 GeV accelerator with a circumference of about 2 miles [28]. The main purposes of the Main Injector are to accelerate the 8 GeV protons up to 150 GeV for injection to the Tevatron and to provide 120 GeV protons to the anti-proton source. The construction of the Main Injector and its replacement of the Main Ring also provided the significant luminosity increase needed for many Run II physics programs.

  The overall benefits of the Main Injector can be summarized as:

  1. Increase in the proton intensity for antiproton production from

4.5×10^{15}/hour to 12×10^{15}/hour.

2. Increase the total number of protons injected to the Tevatron up to 6×10^{13}.

3. Acceleration of antiprotons in stacks of about 2×10^{12} for injection to the Tevatron.

4. Reduction in the beam background effects at the interaction points caused by Main Ring before.

- **The Anti-proton Source**

  The production of anti-protons is a much more difficult process than the production of protons from the hydrogen gas described before. One of the main problems in producing the anti-protons is the time required to collect the necessary number of anti-protons. This production is a very inefficient process with one or two anti-protons produced for every 10^5 protons striking the production target. Therefore, the main limiting factor for the Tevatron luminosity is the production of anti-protons.

  The anti-proton source is a facility which includes the target station and two rings which are called the Debuncher and the Accumulator [29]. The production of the anti-protons starts with the extraction of 120 GeV proton beam from the Main Injector containing a stack of 5×10^{12} protons. With the help of extraction bending magnets, the proton beam is diverted to the target station where the incident beam is further focused into a small area using a series of quadrupole magnets.

  A visual description of the collision process is given in Fig. 3.5. Fo-

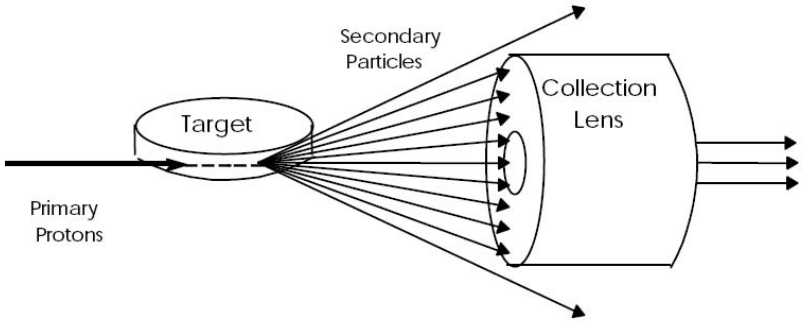

Figure 3.5: The process of anti-proton production [29]. A nickel target is used to create a shower of particles which contains anti-protons.

cused beams of protons strike a nickel target and the collisions produce a shower of secondary particles. This shower is further focused using a lithium lens known as the "Collection Lens". Negatively charged particles in the secondary beam are extracted by means of dipole magnets whereas all the rest of the particles are absorbed at a beam dump. At this point the average kinetic energy of the particles in the negative particle beam is about 8 GeV with a significant spread in the range of particles' momenta.

The key to accumulating a large and intense number of anti-protons is a process called *stochastic cooling*. Stochastic cooling is a technique that is used to remove the randomness of the initial anti-protons produced at the nickel target. The randomness of the momenta of the particles in the anti-proton beam can be described by a "temperature" or "isotropy", hence the stochastic cooling process reduces the temperature of the beam ("cools") and maintains a homogeneous beam on a particle by particle basis.

- **The Debuncher and Accumulator** The Debuncher and Accumulator are two anti-proton storage rings within the same rounded-triangle type tunnel with a circumference of about 51 m. The antiprotons from the target station are transferred into the Debuncher where the momentum spread of the particles is reduced.

  The purpose of the Accumulator, on the other hand, is to collect large quantities of anti-protons before injection to the Main Injector. The Accumulator also creates the bunch structure for the anti-proton beam that coincides with the proton beam already in the Main Injector. As we mentioned before, this collection of anti-proton stack is a long process and it usually takes many hours before reaching the desired amount of anti-protons ($\sim 10^{12}$) to be injected back into the Main Injector where they are accelerated to 150 GeV .

- **The Tevatron**

  The Tevatron is the last piece of the accelerator structure in the Fermilab Accelerator complex and it is also the site where proton anti-proton collisions occur. The Main Injector supplies proton and anti-proton beams of 150 GeV and these beams are then accelerated to 980 GeV inside the Tevatron ring.

  The Tevatron bends the beams of particles and keeps them in the orbit using a large array of superconducting dipole magnets that provide fields of up to 4 T, operating at liquid helium temperatures. The shape of the beams are further focused near interaction points (where the detectors are) using a series of quadrupole focusing magnets in order to provide increased luminosity.

As seen in Fig. 3.1, there are two small beam transverse size spots along the Tevatron ring, BØ and DØ points. Currently, BØ point hosts the Collider Detector Facility (CDF) Experiment and the DØ interaction point hosts the DØ Experiment.

Performing as a storage ring, the Tevatron accommodates 36 bunches of protons and anti-protons travelling in opposite directions with bunch spacing of 396 ns (2.5 MHz crossing rate). A useful set of Tevatron operating parameters are given in Table 3.1 for the two periods of running.

3.1.1 Luminosity and Cross-Sections

In high-energy physics, the processes are often expressed with a cross-section, σ, which is a measure of the interaction probability per unit flux. In collider experiments, the flux corresponds to the size and amount of particles in the colliding beams and is referred to as the luminosity, $\mathcal{L}$. The luminosity depends on a number of beam characteristics at the interaction point like the number of particles in each colliding beam, number of bunches and the transverse sizes of the bunches. It is often expressed in units of $\mathrm{cm}^{-2}\mathrm{s}^{-1}$ and it takes the form given in Eq. 3.1 at Tevatron [30].

$$\mathcal{L} = \frac{fBN_pN_{\bar{p}}}{2\pi(\sigma_p^2+\sigma_{\bar{p}}^2)}F\Big(\frac{\sigma_\ell}{\beta^*}\Big) \tag{3.1}$$

where;

$f \equiv$ revolution frequency

$B \equiv$ number of bunches

	Run Ib	Run IIa
Energy (GeV)	900	980
Bunches	6	36
Bunch Length RMS (mm-mr)	0.6	0.43
Protons(p)/bunch	2.32×10^{11}	2.70×10^{11}
Antiprotons ($\bar{p}$)/bunch	5.50×10^{10}	3.00×10^{10}
Total Antiprotons	3.30×10^{11}	1.30×10^{12}
$\bar{p}$ production rate (1/hr)	6.00×10^{10}	1.70×10^{11}
Proton Emittance (mm-mr)	23π	20π
$\bar{p}$ Emittance (mm-mr)	13π	15π
Beta Function (β^*) @ IP (mm-mr)	0.35	0.35
Average Luminosity ($cm^{-2}s^{-1}$)	1.6×10^{31}	8.1×10^{31}
Integrated Luminosity (pb^{-1} /week)	3.2	16.3
Bunch Spacing (ns)	3500	396
Interactions / Crossing (@ 50 mb)	2.7	2.3

Table 3.1: Miscellenaous Tevatron operating parameters [30]. Run Ib is the period of running from 1994 to 1995 and Run IIa is the period of running which started in 2002 and is still in progress.

$$
\begin{aligned}
N_i &\equiv \text{number of protons or anti-protons} \\
\sigma_i &\equiv \text{gaussian width of the proton or anti-proton beam} \\
F(\sigma_\ell/\beta^*) &\equiv \text{form factor}
\end{aligned}
$$

The cross-section, on the other hand, is expressed in units of *barn* where 1 barn $\equiv 10^{-28}$ m^2. Although it is intuitive to relate this quantity to an effective

geometrical area as in the case of classical elastic collisions, this quantity is not associated with anything similar in high-energy physics. Cross section is merely a figure of interaction probability and when combined with a given luminosity, it gives the interaction rate for a specific process as given in Eq. 3.2.

$$R = \sigma \mathcal{L} \tag{3.2}$$

Perhaps a more interesting quantity than the interaction rate per unit time is the number of interactions given a period of time. An integration of the interaction rate over time gives us the total number of interactions occuring in the collisions as given in Eq. 3.3.

$$N = \sigma \int_{t_0}^{t_0+\Delta t} \mathcal{L} dt \tag{3.3}$$

For a particular interaction, the cross-section is a constant but depending on the accelerator conditions, the luminosity is usually a changing factor over time. The integral quantity in Eq. 3.3, $\int_{t_0}^{t} \mathcal{L} dt$, is also referred to as the integrated luminosity over Δt. For example, a certain process of 1 pb cross-section is expected to occur 100 times during the delivery of 100 pb^{-1} integrated luminosity.

In Table 3.1, we listed corresponding Tevatron luminosity figures from Run IIa. The integrated luminosity profile of the Tevatron can also be seen in Fig. 3.6 from the start of Run IIa in April 2002 to Summer 2004. Even though the total integrated luminosity available for physics analyses is more than twice as much, the result presented in this thesis makes use of about 180 pb^{-1} colllider data.

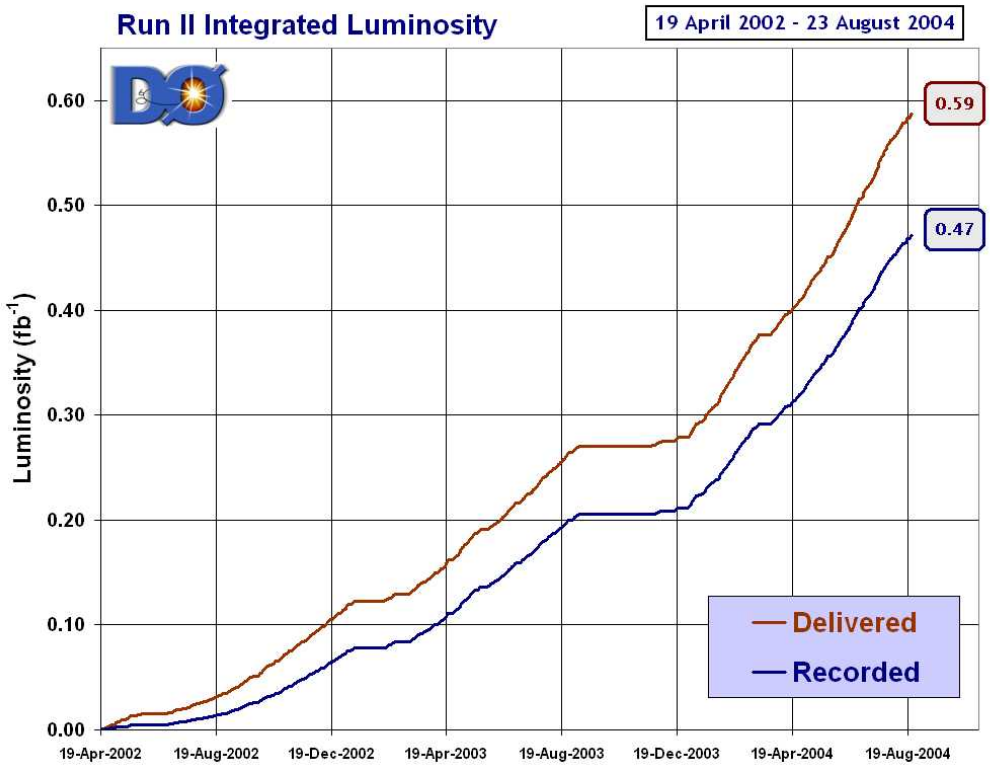

Figure 3.6: Tevatron integrated luminosity delivered to DØ experiment over two years between 2002 and 2004. Note that not all the delivered luminosity is recorded and available to the experiment due to the operation inefficiencies and the down time occuring during the recording process.

3.2 DØ RunII Detector

The DØ detector [31] is a multi-purpose apparatus composed of several sub-detector components and occupies a collision vault of about 2000 m^3 centered at the DØ interaction point of the Tevatron ring. The detector had originally been built for the Run I period of the Tevatron running but after significant upgrades, its capabilities have recently been increased even further.

A high-energy physics detector of this magnitude is generally a very com-

plex structure with about 5000 tons of detector material and about a million readout channels. It is designed and optimized to find the identities and the traces of the particles coming out of the proton-antiproton collisions and measures a list of useful physical quantities like their charges, momenta, energy as well as the 3D spatial location of their travel path through the detector. The original design of the detector in Run I proved to be a big success with the discovery of top quark [32] along with the CDF experiment [33], as well as making important measurements and providing improved understanding of many high-energy physics phenomena.

The DØ detector recently went through a series of upgrades together with the improvements in the Tevatron Accelerator Complex and more ambitious physics goals. The detector we describe in this chapter will refer to the current state of DØ , or the DØ Run II detector. An overall view of the DØ detector and its components can be seen in Fig. 3.7.

DØ detector is composed of three major detector sub-systems:

- **Tracking**

  Inclusion of a high-precision central tracking system immersed in a 2T solenoidal magnetic field provided by a commercially produced superconducting solenoid is the most important element in the Run II upgrade for DØ detector (Fig. 3.8). Composed of several tracking detectors, this system provides a precise charged particle trajectory (track) reconstruction and momentum measurement through its bending in the magnetic field. The tracks are analyzed to find the hard-scatter point where the collision occurs as well as secondary vertices where the long lived particles such as b-quark states or tau leptons produced.

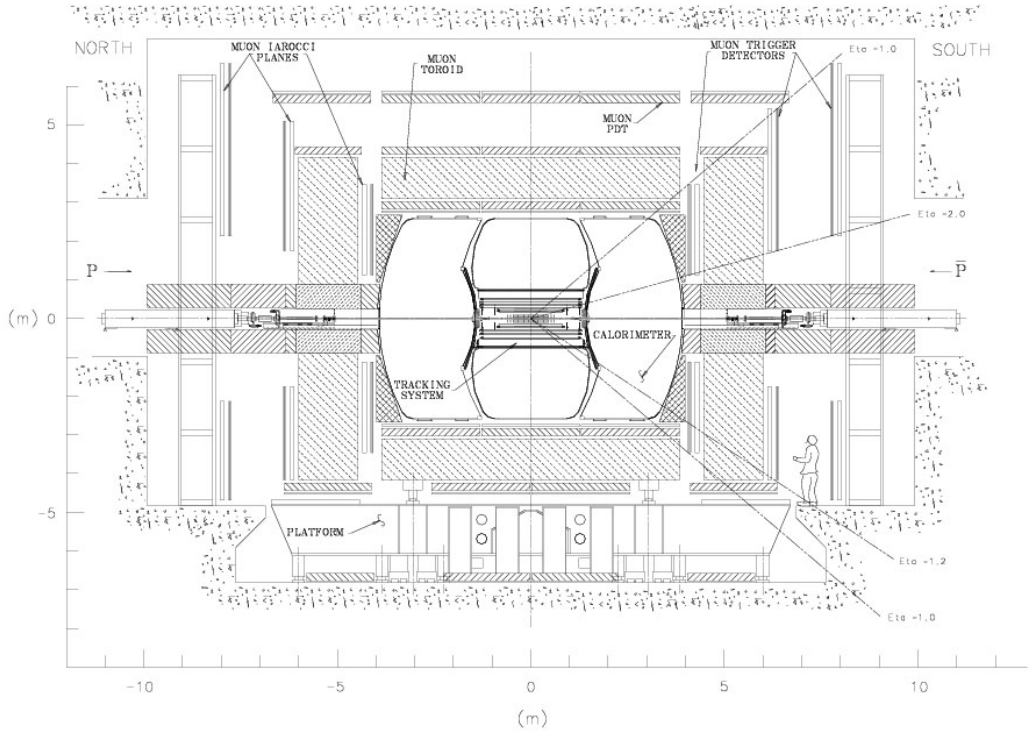

Figure 3.7: Two dimensional schematic view of the Run II DØ detector with several sub-systems specified.

The innermost tracking detector which is at the center of the DØ detector and closest to the beam line is the Silicon Microstrip Tracker (SMT). Being very close to the interaction point (IP) this detector enhances the impact parameter resolution of the tracks and becomes the most important ingredient for precise vertex reconstruction as mentioned above. Outside the silicon tracker, the DØ tracking volume includes a scintillating fiber detector called Central Fiber Tracker (CFT). Combined with the information coming from the SMT, this detector plays an important role in three-dimensional charged particle track reconstruction and momentum measurement.

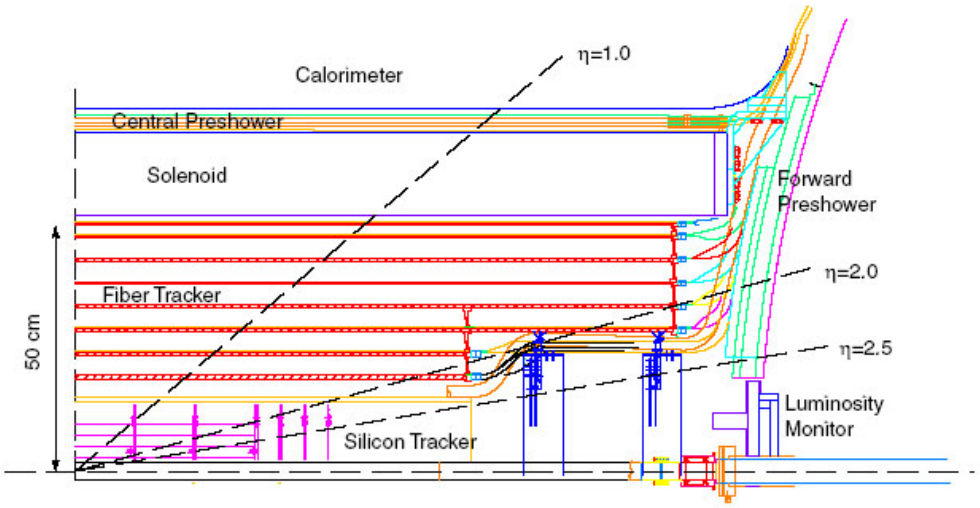

Figure 3.8: Two dimensional schematic view of the Run II DØ tracker system (quadrant of the detector). The innermost silicon tracker (SMT), central fiber tracker (CFT), solenoid magnet, central preshower (CPS) as well as forward preshower (FPS) detectors are marked on the figure.

Going out radially from the center of the detector, a superconducting solenoid magnet providing a uniform magnetic field of 2T covers the central part of the tracking volume. By measuring the curvature of the trajectory of charged particles in the magnetic field of the solenoid, the momenta of the tracks can be determined.

- **Calorimetry**

  DØ has a very advanced calorimetry system for measuring particle energies, with large coverage, finely segmented central and forward liquid argon calorimeters as well as central and forward preshower detectors. The liquid argon calorimeter provides accurate measurements of particles like electrons and photons as well as hadronic particle showers.

Preshower systems, both central and in two forward regions, also provide a pre-calorimeter sampling of the energy and provides electron vs. photon pattern recognition.

In addition to providing a measurement of the energy, DØ calorimeter systems also aid in 3D spatial reconstruction. With finely segmented structures in central and forward regions, calorimeter detectors provide an independent confirmation of track location via the localization of energy depositions.

- **Muon Spectrometry**

  Unlike electron, photon and hadrons, muons can penetrate through the calorimeter. Therefore, the muon system is positioned as the outermost system of the DØ detector (Fig. 3.7 and it provides extensive coverage for muon detection and measurement. Three layers of muon detectors in central and front regions of the detector are stacked with a toroidal magnetic field. Similar to the central tracking system, the DØ muon spectrometers provide both localization and momentum measurement for muons.

In the following subsections, we will review the individual components of the DØ detector in more detail but first, a general introduction to DØ coordinate system and conventions is provided.

3.2.1 Coordinate Systems and Conventions

The coordinate system employed by the DØ detector is a right-handed system. The z-axis of the coordinate is aligned parallel to the beam direction

with positive side pointing along the proton beam direction (south). The transverse axes, x and y, are aligned in a right-handed fashion, such that positive x-axis points outward towards east, with the y-axis pointing upward.

Rather than this cartesian system, DØ most often uses a cylindrical coordinate system (z, ϕ, θ). The polar angle, θ, is defined as the angle relative to the $+z$-axis, while the azimuthal angle, ϕ, is defined to be the angle on the transverse plane (xy-plane) and it is measured from the $+x$-axis.

Kinematic quantities used at DØ are the 4-vector momenta of the particles and 3D spatial location for vertices and track trajectories. These kinematic quantities in the fixed laboratory frame are not always useful for practical purposes. The net boost of the colliding proton and anti-proton along the transverse direction is almost zero, so the choice of laboratory xy frame is suitable but we cannot say the same for the z-direction. Therefore, instead of using the polar angle that needs to undergo relativistic transformation when switched back to the rest frame of the particles, a variable called the "rapidity" (y) is chosen as a more suitable variable defined in Eq. 3.4.

$$y = \frac{1}{2}\ln\left[\frac{E + p_z}{E - p_z}\right] \tag{3.4}$$

Although y is invariant under Lorentz transformations, a more convenient quantity called "pseudo-rapidity" (η) is used instead of the polar angle, θ. Pseudo-rapidity is defined as in Eq. 3.5 and it is the limit of y when the mass of the particle is much smaller than its energy..

$$\eta \equiv -\ln\Big[tan\Big(\frac{\theta}{2}\Big)\Big] \tag{3.5}$$

$$\equiv \quad \tanh^{-1}(\cos\theta)$$

and;

$$\lim_{m/E\to 0} y \quad = \quad \eta$$

Even though we speak of a laboratory frame, the frame of reference for describing the interactions and physical phenomena is a dynamical frame which is adjusted for each collision (event) and therefore the origin of the coordinate system is not always the (0,0,0) point and hence does not coincide with the geometrical center of the detector. This is due to the fact that the proton and anti-proton collisions occur within a geometrical volume rather than a point in the space. Since the particles emanate from the interaction point, we take this scattering vertex as the origin of the coordinate system, often referred as the "physics" coordinates as opposed to the detector coordinates. The spread of the interaction vertex in the transverse plane is usually very small with a gaussian width of about 30 microns centered on the beam axis. However the interaction point along the z-axis has a much wider distribution ($\sigma_z \simeq 30$ cm) due to proton and anti-proton bunch lengths in the longitudinal direction. Therefore the "physics" origin of the reference frame is dynamically adjusted for each event and it is usually the case that $\eta_{\,physics} \neq \eta_{\,detector}$.

Another widely used quantity is the transverse momentum (as well as energy) referring to the component of the momentum of the particle along the $x-y$ plane, defined in Eq. 3.6. The reason for frequent use of this variable rather than the 3D momentum comes from the fact that momentum conservation can only be applied in the transverse plane for hadron colliders due to

the undetected particles travelling down the beam pipe and the possibility that there may be multiple interactions in a single bunch crossing.

$$\begin{aligned} E_T &= E \times \sin\theta \\ p_T &= |\vec{p}| \times \sin\theta \end{aligned} \tag{3.6}$$

3.2.2 Solenoid Magnet

One of the most common ways of finding the momentum of charged particles is to determine their curvature in a known magnetic field. With the inclusion of a new central tracking system, DØ also obtained a new solenoid magnet which provides a magnetic field strength of 2T along its 2.7 meters of length [34]. The commercially built solenoid is composed of two layer superconducting coils and stores a total energy of 5MJ. The body of the solenoid magnet and its cryostat is about 0.9 radiation lengths thick.

The magnetic field provided by the solenoid is uniform to the level of 0.5% inside the tracking volume, [35], and field uniformity can be seen in Fig. 3.9. A useful set of solenoid parameters are also listed in Table 3.2.

3.2.3 Silicon Microstrip Tracker (SMT)

The major motivation for including a silicon detector in the design and construction of the Run II DØ detector is to have a very good momentum resolution for tracks and good vertex reconstruction. The Silicon Microstrip Tracker (SMT) is the highest resolution sub-detector and being closest to

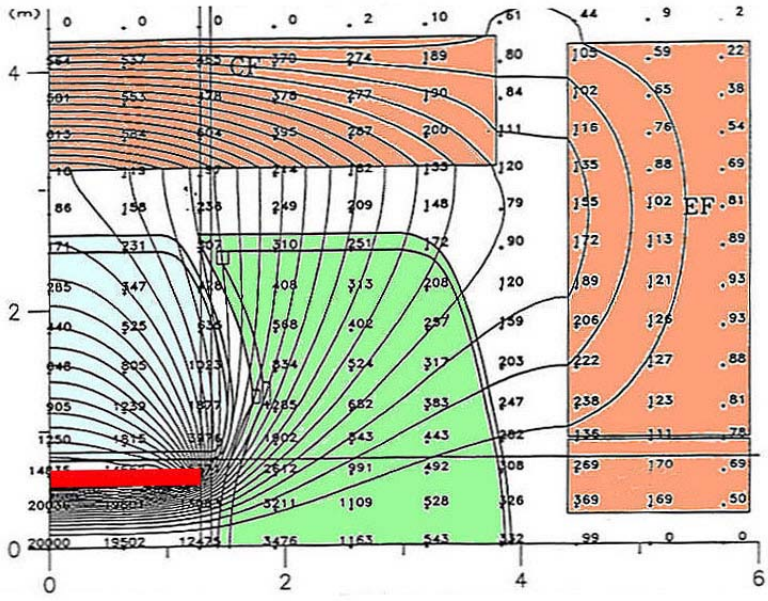

Figure 3.9: The field strength of the solenoid magnet over a quadrant section of the DØ detector. Magnetic field is uniform to 0.5 % level within the central tracking volume.

	Value
Central Field Strength (T)	2.0
Operating Current (A)	4825
Stored Energy (MJ)	5.6
Length (cm)	273
Inner Radius (cm)	53.3
Outer Radius (cm)	70.7
Radiation Thickness	0.87
Operating Temperature (K)	4.7 - 4.9

Table 3.2: Summary of DØ 's superconducting solenoid magnet parameters [34].

the beam collision point, it provides superb impact parameter and vertexing capability to DØ .

The main factors that drive the design of the silicon tracker detector are:

- three-dimensional track reconstruction capabilities with transverse impact parameter resolution better than 30 μm and good vertex resolution in longitudinal direction
- radiation hard detector which can withstand the increased luminosity of Run II Tevatron environment
- a capable readout system that can reliably be operated at the 2.5 MHz bunch crossing rate

The silicon tracker is a so-called hybrid system composed of barrel (strips running parallel to the beam direction) and disk geometry detectors (strips perpendicular to the beam direction) [36] covering the innermost area of the DØ detector ($r_{\mathrm{SMT}} < 10$ cm) as shown in Fig. 3.10. This design is motivated by the extended interaction region due to the longitudinal beam width and the desire to provide good coverage for large pseudo-rapidity regions.

The barrel detectors are composed of 4 concentric cylindirical layers (superlayers) repeating in 6 identical sections running parallel to the beam pipe. The radii of the superlayers range from 2.7 cm to 9.4 cm and the length of each barrel segment is 12.0 cm long. The basic silicon detector unit is called a ladder and it consists of 300 μm thick silicon wafers (6 cm $\times$ 2.1 cm) positioned end to end and electrically connected by micro-wirebonds. A schematic view of a ladder detector can be seen in Fig. 3.11. The second and fourth superlayers of barrel detectors are composed of ladders which are

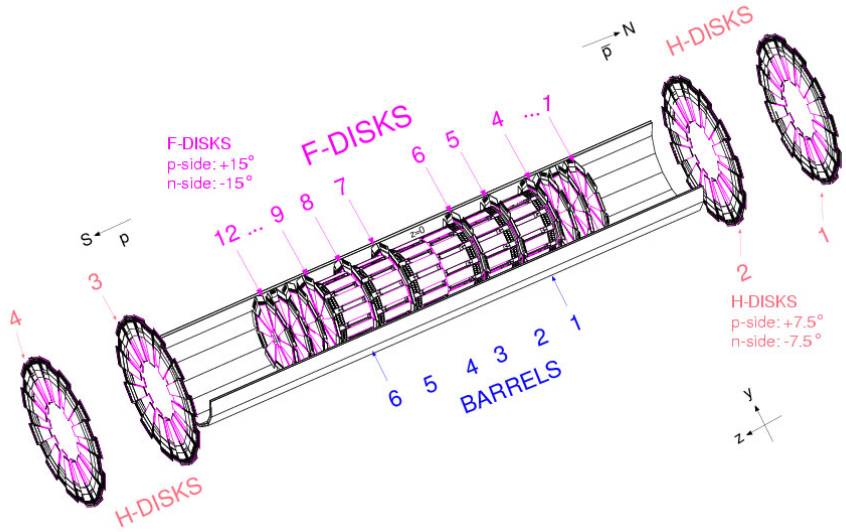

Figure 3.10: Three dimensional view of the SMT detector [24]. The detector has a hybrid structure being composed of layers of barrel detectors as well as two sizes of disk detectors. There are 6 barrel detectors with interspersed F disk detectors. There are 12 F disk detectors which are smaller in radius than their high pseudo-rapidity (high-z) coverage H disk detector counterparts. The total number of H disks is 4, two being on each side (south and north).

double-sided with strips on the two sides aligned at a small stereo angle of 2 degrees. These ladders have strips of 62.5 μm pitch. The first and third layers of the central four barrels also have double-sided detectors with 90 degree stereo angles and strip pitch of 156 μm. The outer barrels of these layers have single-sided axial (no-stereo angle) detectors with 50 μm pitch.

The F-disk detectors are interspersed between the barrel detectors, perpendicular to the beam direction (z-axis). Providing z-coordinate information (as well as rϕ), they are instrumental in providing three dimensional track reconstruction and enabling tracking at angles close to the beams (high

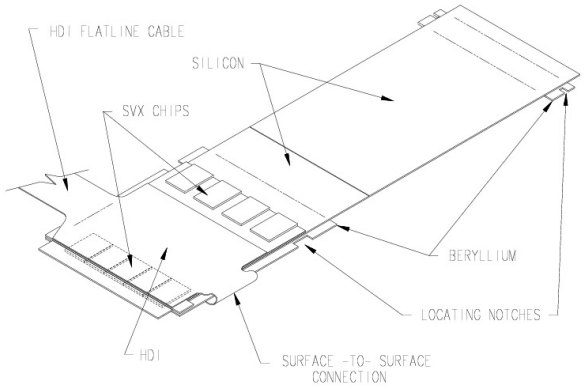

Figure 3.11: A drawing of the double sided silicon ladder detector (shown 9 chip design). Ladder detectors are the basic units of the SMT detector and enable good hit resolutions of about 10 μm.

η). These disks consist of 12 overlapping wedges with the surface dimensions of 2.6 cm $< r <$ 10.5 cm. The H-disks occupy a larger surface with dimensions of 9.5 cm $< r <$ 26.0 cm at $z = \pm 94$ cm and $z = \pm 126$ cm covering $|\eta_{det}| < 3$.

The structural support of the Silicon Microstrip Tracker is provided by beryllium bulkheads which can precisely be positioned and therefore provide the crucial alignment of the detector. These bulkheads also support the cooling for the electronic components at the edge of the ladders. These bulkheads are mounted on sturdy carbon fiber half cylinders for further support.

The technical details of the SMT detector are summarized in Table 3.3. With nearly 800,000 readout channels, SMT provides an $r - \phi$ hit resolution of about 10 μm and z hit resolution of 35 μm. This level of resolution helps DØ achieve a very good track pattern recognition capabilities as well as primary (hard-scatter) and secondary vertex reconstruction ability.

	Barrels	F-Disks	H-Disks
Layers (Planes)	4	12	4
Channels	387k	258k	147k
Modules	432	144	192
Readout Length	12.0 cm	7.5 cm	14.6 cm
Inner Radius	2.7 cm	2.6 cm	9.6 cm
Outer Radius	9.4 cm	10.5 cm	26.0 cm

Table 3.3: Summary of Silicon Microstrip Tracker (SMT) parameters broken down for different detector sections (barrels, f-disks and h-disks).

3.2.4 Central Fiber Tracker (CFT)

The Central Fiber Tracker (CFT) surrounds the SMT detector and extends the effective tracking volume to larger radii [37]. CFT is composed of layers of scintillating fibers at different radii and combined with the SMT hit information provide the three-dimensional charged particle tracking at DØ . The additional hit information coming from the CFT improves the momentum resolution, and to some extent the impact parameter resolution of the tracks. Another useful feature of CFT detector is that it provides the triggering ability for tracks.

8 CFT double-layers[4] cover the radial range from about 20 cm to 50 cm. The scintillating fibers are made out of a polystyrene core surrounded by a thin acrylic coating, which in turn is covered by a thin flouro-acrylic coating. These three fiber materials have internal refraction indices of 1.59, 1.49 and 1.42, respectively. The last layer of coating increases the light

[4]Each double-layer is a composite of an axial and a u or v stereo layer.

trapping efficiency by about 70 % with respect to the single coated fibers.

Primary track ionizes the molecules in the scintillator material and the subsequent ground state transitions yield photons. These photons is internally reflected inside the fiber and transported to the photo-detectors located outside the detector platform. The photo-detector devices are called Visible Light Photon Counters (VLPC) and they are operated at about 9 K. The VLPC devices, silicon-avalanche based photon detectors, operate at quantum efficiencies of over 70 %, noise rate of less than 0.1 % and a rate capability of more than 10 MHz [38]. The scintillation photons reaching the surface of these devices are detected and converted into digital signals, sent to the front-end electronics and read out for the reconstruction of hit information.

A schematic view of the Central Fiber Tracker can be seen in Fig. 3.8. With 8 doublet layers of scintillating fibers, the CFT detector accommodates about 80,000 read-out channels. A typical doublet layer has one layer of fibers stretched along the axial direction (parallel to the beam direction i.e. z-axis) and another stereo layer (u or v orientation) at a stereo angle of about 2 degrees. The orientation of the layers from the innermost radius to outer radii goes like $xu - xv - xu - xv - xu - xv - xu - xv$. A detailed information of the scintillating fiber layers is provided in Table 3.4.

3.2.5 Central Preshower (CPS) Detector

The Central Preshower Detector (CPS) is another scintillator detector sitting just outside the central tracking volume sandwiched in the 5 cm radial space between the superconducting solenoid magnet and the central calorimeter cryostat [39, 40]. The central preshower detector consists of a layer of lead

Layer	Radius (cm)	# of Fibers	Fiber Pitch (μm)	Length (m)
1-x	19.99	1280	979.3	1.66
1-u	20.15	1280	987.2	1.66
2-x	24.90	1600	975.8	1.66
2-v	25.60	1600	982.1	1.66
3-x	29.80	1920	973.4	2.52
3-u	29.97	1920	978.6	2.52
4-x	34.71	2240	971.7	2.52
4-v	34.87	2240	976.2	2.52
5-x	39.62	2560	970.4	2.52
5-u	39.78	2560	974.4	2.52
6-x	44.53	2880	969.5	2.52
6-v	44.69	2880	972.9	2.52
7-x	49.43	3200	968.7	2.52
7-u	49.59	3200	971.8	2.52
8-x	51.43	3520	916.1	2.52
8-v	51.59	3520	919.0	2.52

Table 3.4: Summary of Central Fiber Tracker parameters for 8 doublet layers (axial and stereo) [37].

radiator and three layers of finely segmented scintillating triangular bars. The Central Preshower detector helps the electron identification and triggering by measuring the scintillation photons created by the passage of the particles. Located just outside the solenoid magnet, it also aids in the electromagnetic energy measurement by providing a fast and early sampling of the electron

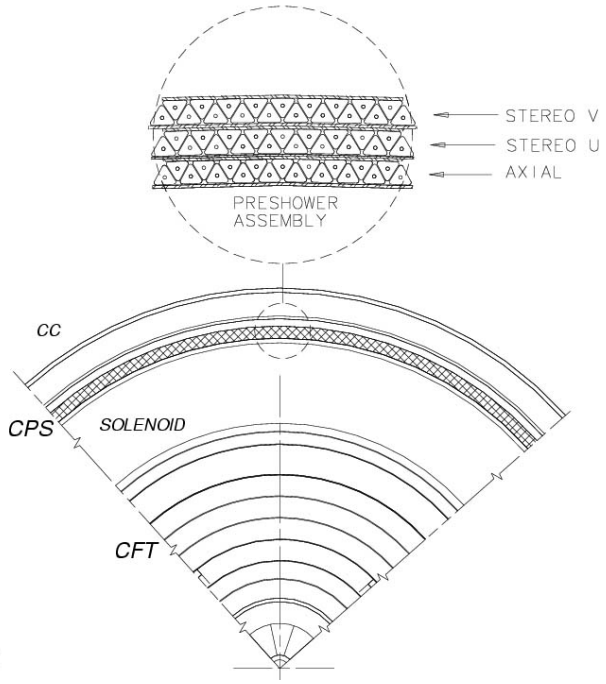

Figure 3.12: An end view (beam direction) of the tracking volume and the CPS detector. Three layers of the CPS detector with triangular shaped scintillating fiber strips are also shown in the enlarged view above.

energy.

As opposed to the rounded shapes of CFT fibers, the fiber strips used for the Central Preshower detector have a triangular geometry with each side of the triangle measuring 7 mm as shown in Fig. 3.12. A hole in the middle of the strips host the wavelength shifting fiber that runs along the full length of the strip. The neighboring strips are placed such that the dead space between the adjacent strips is reduced to zero.

The three concentric CPS layers are arranged in an axial, u and v orientation with a stereo angle of about 23 degrees. The lead layer placed before the fiber layers is about 1 radiation length thick, and with the solenoid, tjere

are about 2 radiation lengths before the CPS at normal incidence.

3.2.6 Forward Preshower (FPS) Detectors

DØ has two additional Forward Preshower (FPS) detectors located in the forward regions ($1.4 < |\eta| < 2.5$), and play a similar role to the CPS [41]. Mounted on the surface of the two end calorimeter cryostats facing the interaction region, these detectors aid in the discrimination of the electromagnetic showers of electrons and photons as well as providing triggering capabilities.

Each FPS detector (one on the south and the other on the north side) is composed of sixteen 22.5 degree wedges. These wedges are composed of an absorber material (two radiation lengths of lead) sandwiched between two sets of two-layer detectors as shown in Fig. 3.13. The two layers before and after the absorber material are aligned at a stereo angle to each other and called the u and v orientations. The two layers closest to the interaction point (upstream) are called the MIP layers and the other two behind the lead absorber material are called the SHOWER layers.

Besides cluster localization and providing an independent source of electromagnetic energy deposition which could later be matched to the energy found in the end calorimeters, the FPS detectors are also beneficial in discriminating the showers caused by electron-like and photon-like objects. All charged particles going through the detector will act as a minimum ionizing particle in the MIP layers (hence the name) and will create a cluster of energy in the exposed strips. The electron signal will be reconstructed when the SHOWER layer cluster location is spatially matched to a found MIP layer cluster. However, a photon will not leave a trace in the MIP layers and

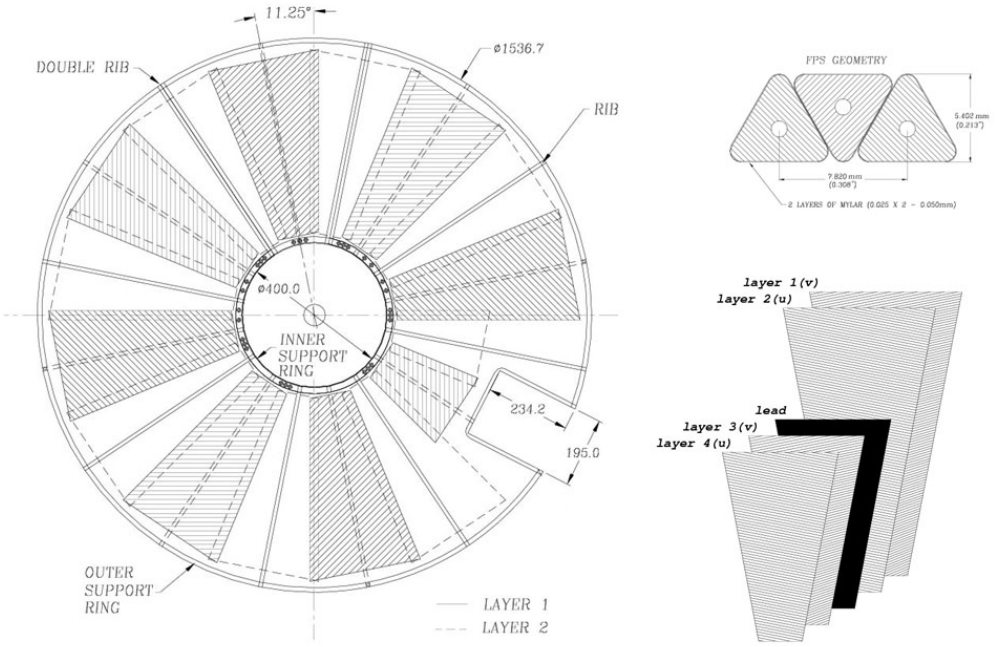

Figure 3.13: Schematic view of the FPS detectors. A full one-side detector with all wedges is shown on the left. The layer composition of each wedge is displayed with the figure on the right bottom side. The figure on top of it shows the triangular geometry of the FPS strips which is similar to the shape of CPS strips.

will be recognized as a cluster in the SHOWER layer without a matching cluster of energy in the MIP layers. For a better demonstration of this discrimination process, 50 GeV electron and π^0 are produced in Monte Carlo simulation and their interaction with the FPS detector layers is shown in Fig. 3.14.

3.2.7 Calorimeter

The uranium-liquid argon calorimeter system as shown in Fig. 3.15, plays a very significant part in the particle detection and measurement techniques applied at DØ [42]. It is built from alternating layers of heavy absorber plates and active ionization detectors. The major role of a calorimeter is to detect the electromagnetic and hadronic showers initiated by the particles like electrons, photons as well as hadronic jets. Besides detecting these showers, calorimeter also provides a way to measure the energies of these particles. Measuring the total visible energy deposition in the event and using momentum conservation in the transverse direction, the calorimeter provides a means of measuring the missing energy due to undetected particles like neutrinos as well.

The electromagnetic (EM) and hadronic (HD) showers are reconstructed by their distinguishing signals in the layers of the calorimeter. EM particles create showers in the calorimeter mostly due to bremsstrahlung and pair production. For each interaction, the number of secondary particles increases to a maximum and then dies out rather quickly. The number of such particles is proportional to the primary's energy. Recording the total number of these secondaries in the active sampling layers gives us a reliable way to reconstruct

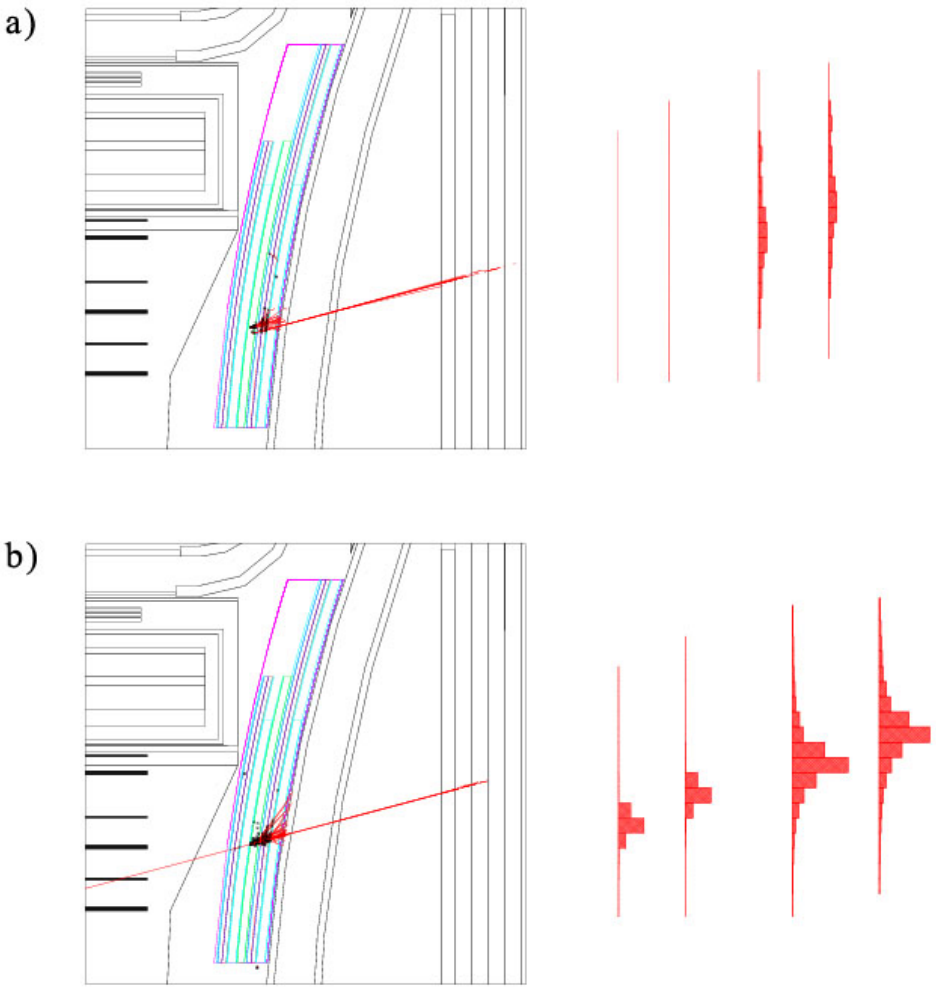

Figure 3.14: Signature of 50 GeV $\pi^0 \rightarrow \gamma\gamma$ (a) and electron (b) particles in the FPS detector generated by GEANT simulation. As described in the text, photons (from π^0) leave no trace in the first two MIP layers located before the lead absorber (histograms on the right) but electrons are recognized by their distinguishing energy depositions in these layers.

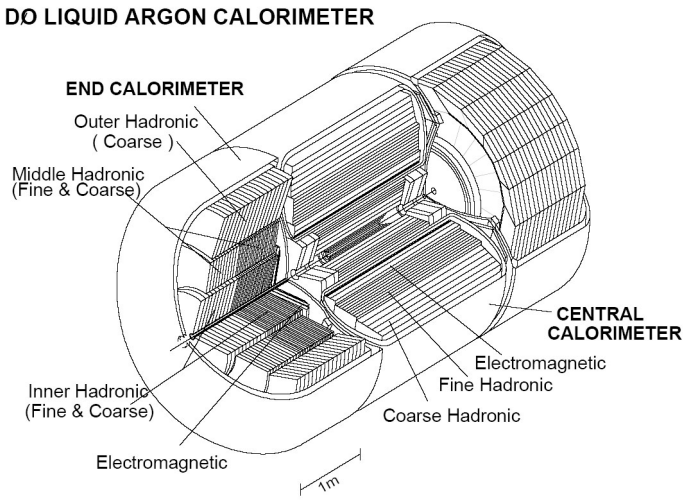

Figure 3.15: Full view of the DØ calorimeter which consists of one central and two end sections [43]. All three sections of the DØ calorimeter are divided into finely segmented electromagnetic and hadronic (fine and coarse) sections.

the original particle energy after an appropriate calibration.

For hadronic particles, on the other hand, the interaction with the detector occurs mostly via the strong nuclear forces with the uranium nuclei. By measuring the number of secondary particle showers produced as a result of these interactions, the energy of the hadron is reconstructed. Due to DØ calorimeter's finely segmented structure, Fig. 3.16, the energy depositions are localized to a good precision and this way three-dimensional kinematic profiles of the particles are reconstructed.

The DØ calorimeter uses liquid argon as the primary ionization medium and a dense metal as the absorber material. It is divided into three geographical cryostats, central calorimeter (CC) and two end calorimeters (EC) one on north side and the other in south side. The CC covers a region of $|\eta| < 1.0$ while the ECs extend to forward pseudo-rapidity regions of up to $|\eta| \simeq 4.5$.

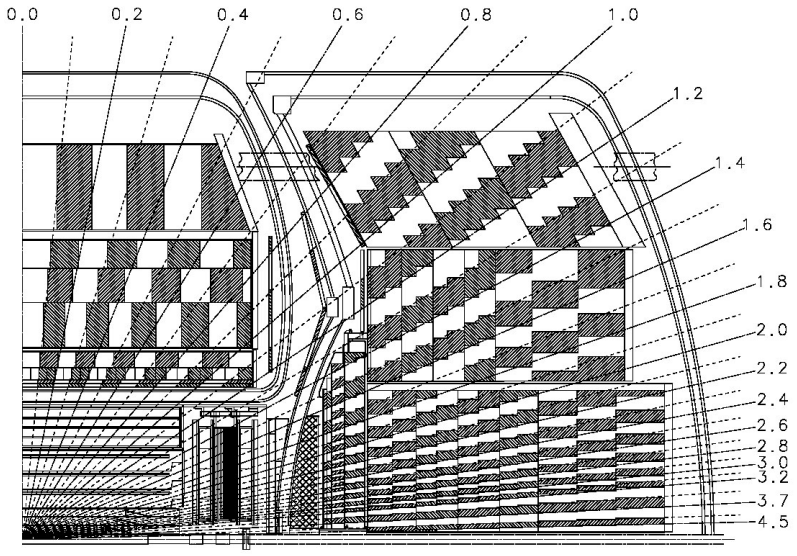

Figure 3.16: A schematic view of the calorimeter segmentation in a quarter of the detector. The radial lines show the detector psuedo-rapidity ranges covered by the calorimeter.

The total number of nuclear absorption lengths for central calorimeter is approximately 7, meaning that a photon has a probability of $1/e^7$ of suffering no interaction when it traverses the calorimeter. There are about 9 absorption lengths for the end calorimeters. Each calorimeter is made of three sections consisting different absorber thickness layers and materials. The innermost concentric layers are called the electromagnetic (EM) sections followed by fine hadronic (FH) and coarse hadronic (CH) sections. Technical details of the central calorimeter layer modules are given in Table 3.5, [43].

The basic detector unit of the calorimeter is shown in Fig. 3.17. A calorimeter read-out unit consists of a grounded absorber plate and a signal board maintained at a high voltage. When a secondary shower particle travels within the liquid argon medium of a calorimeter cell, it causes ionization

in the material and the ionization electrons drift to the readout boards where the collected charge is converted into a current. The drift time for electrons accross the liquid argon gap is 450 ns. Each cell has a typical size of $\Delta\phi \times \Delta\eta = 0.1 \times 0.1$ providing the fine segmentation necessary for good shower localization. Each section has several readout cells along the shower direction as indicated in Table 3.5.

CC Modules	EM	FH	CH
Rapidity Range	$\|\eta\| \leq 1.2$	$\|\eta\| \leq 1.0$	$\|\eta\| \leq 0.6$
Primary Absorber	Uranium	Uranium	Copper
Absorber Thickness	2.3 mm	6.0 mm	46.5 mm
Total Radiation Lengths	20.5	96	32.9
Total Nuclear Absorption Lengths	0.76	3.2	3.2
Number of Read Out Sections	4	3	1
Channels	10368	3000	1224

Table 3.5: A useful set of parameters for the Central Calorimeter [43].

The information from the cells are both sent to precision readout as well as the Level 1 calorimeter trigger. However, instead of using all the granularity of the cells, the calorimeter trigger uses $\Delta\eta \times \Delta\phi = 0.2 \times 0.2$ towers of cells, summed separataly for EM and FH sections, these towers give pseudo-rapidity projected accumulations of the calorimeter deposits.

3.2.8 Inter-Cryostat Detectors (ICD)

The region between the central cryostat and end cryostat is called the inter-cryostat region (ICR) and corresponds to the pseudo-rapidity range of 1.1

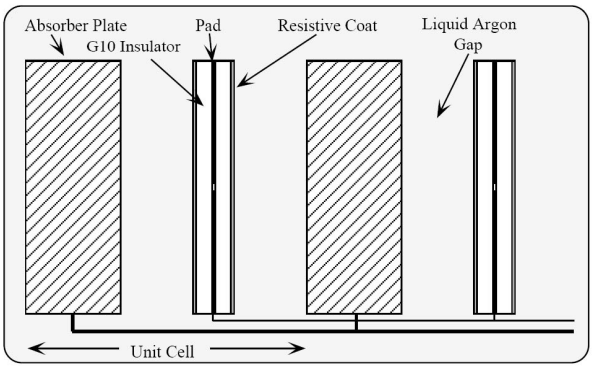

Figure 3.17: Schematic view of a calorimeter cell (two units shown).

$< |\eta| < 1.4$. This region of the detector suffers from the lack of detector instrumentation due to the existence of the support structures and cryostat walls. In order to improve the energy sampling of the particles going through this region of the detector, a set of Inter-Cryostat Detectors (ICD) are mounted on the inner face of the end cryostat walls [44].

The ICD detector is made of scintillating tiles arranged in a 22.5 degree wedge structure covering the full 2π solid angle of the un-instrumented ICR region as shown in Fig. 3.18. Wavelength-shifting scintillating fiber transmits light via optical connectors which are ultimately read by photomultiplier tubes. These photomultiplier tubes are read in crates mounted in the outside of the end cryostat walls. The digitizing equipment and the electronic is very much similar as the DØ liquid argon calorimeter electronic structure.

3.2.9 Muon Detectors

The muon detectors form the outermost detector substystems and consist of the central and forward muon detectors, as shown in Fig. 3.19. The muon

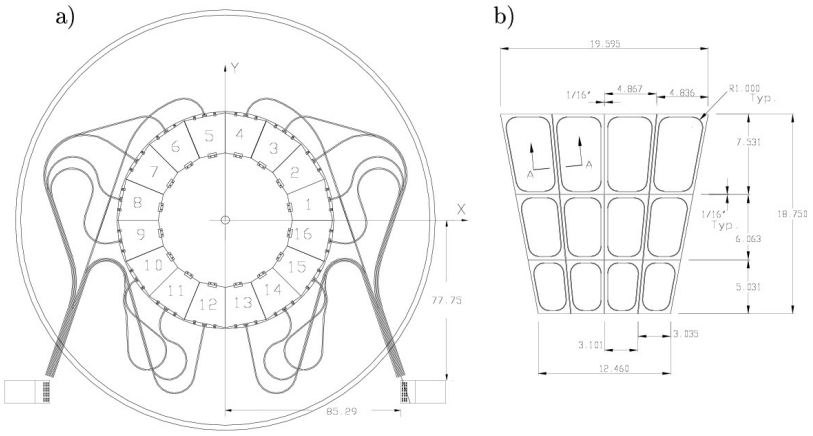

Figure 3.18: Schematic view of ICD modules mounted on the inner face of each end cryostat. a) Full face of the ICD detector with 16 wedges (optical cabling is also shown). b) Each wedge is composed of 12 scintillating tiles placed in an array structure as shown.

detection system is placed outside all other detectors since muons can penetrate a significant thickness of material (the calorimeter etc.) with a small amount of energy lost to ionization (about 2.5 GeV). Although muons are very similar to the electrons in many respects, their larger mass means that bremsstrahlung plays a small role in their energy loss. The primary energy loss is due to the ionization in the material they traverse.

The muon systems at DØ are composed of solid iron toroidal magnets which provide a magnetic field of 1.8 T and a means of measuring the tracks of the muons. The central muon system ($|\eta| < 1.0$) and the forward detectors cover the pseudo-rapidity region of up to $|\eta| < 2.0$. They provide muon identification both for offline studies and trigger purposes. With the toroid magnet, the muon system is also capable of making momentum measurements but the central tracking momentum measurement has much better

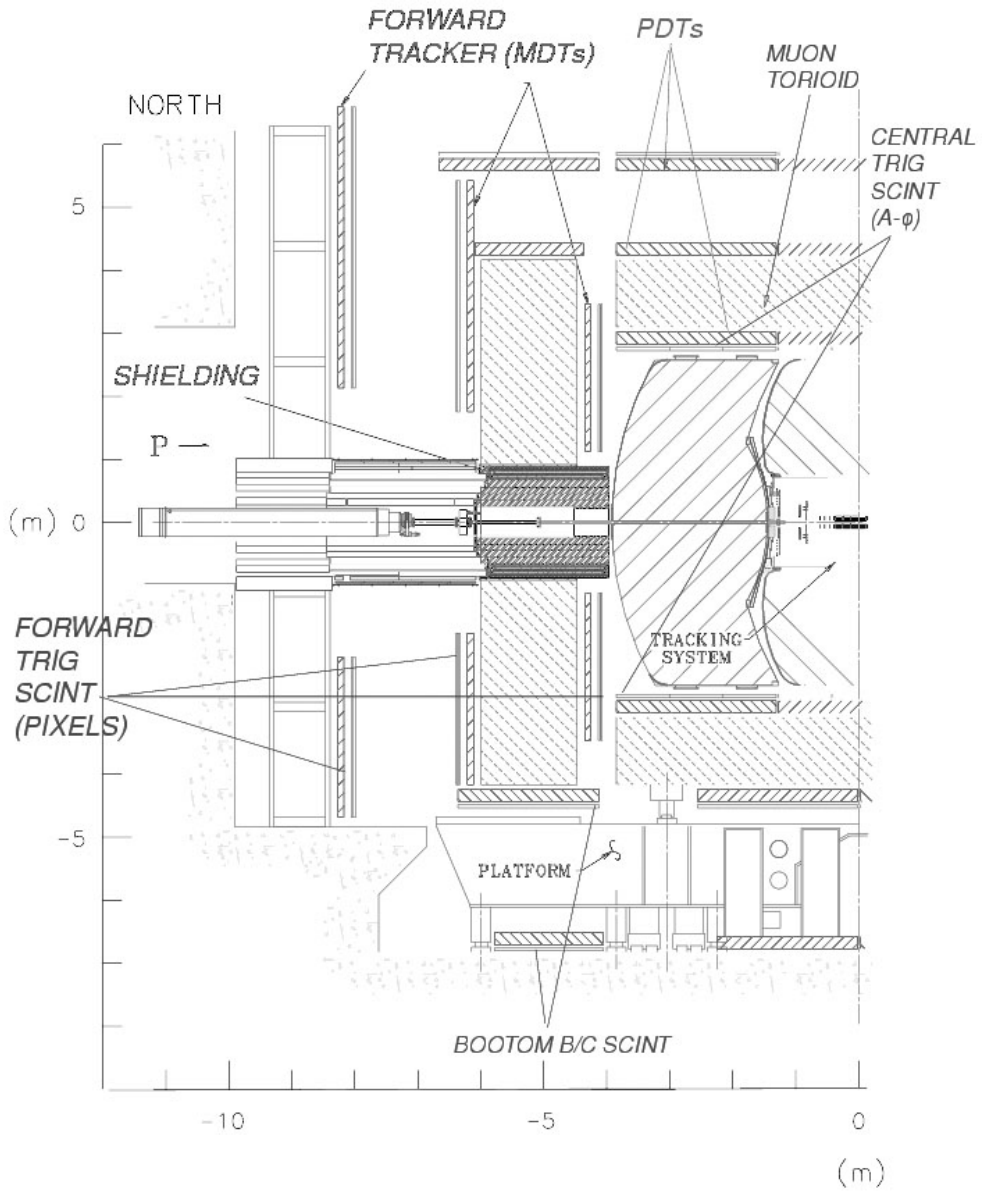

Figure 3.19: Two dimensional view of the half of the DØ detector showing the central and forward muon detectors.

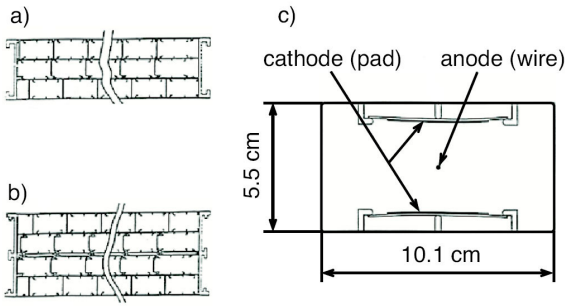

Figure 3.20: End view of extruded aluminum proportional drift tubes in the WAMUS detectors shown in a deck of a) 3 tubes as in B and C layers b) 4 tubes as in A layers. The end view of a single tube shown in more detail with the anode wire and cathode pads marked for clarity [45].

accuracy. The muon system momentum measurement is not generally used in the physics analysis but instead the local tracks found by the muon system are spatially matched to extrapolated central tracks for identifying muons.

The central muon detector called WAMUS (Wide Angle Muon Spectrometer) consists of three layers (A, B and C) of a combination of proportional drift tube detectors (PDT) and scintillators [45]. A layer is the closest to the interaction point and comes before the toroid whereas the B and C layers are placed outside of the toroid magnet.

The PDT chambers are made out of a deck of aluminum tubes (there are 4 decks in the A layer and 3 for the B and C layers) as shown in Fig. 3.20. These tubes are 10.1 cm wide and 5.5 cm high and about 24 of them make a PDT chamber. An anode wire runs along the length of each tube and two vernier pads, one at the top and another at the bottom of the tube, are used as the cathodes. The diamond shaped vernier pads give a coarse

measurement of the hit position along the tube axis. Each tube is filled with a gas mixture of 80 % argon, 10 % CH_4 and 10 % CF_4. At the operational high voltage of the 2.5 kV for the pads and 5.0 kV for the anode wire, the drift velocity in the gas mixture is about 10 cm/μm and the maximum drift time is 500 ns. The hit position uncertainty due to diffusion in the gas mixture is around 375 microns.

Besides the drift chambers, the central muon detector (WAMUS) also accomodates an inner layer of scintillators (A-ϕ counters) and outer layers of scintillators (cosmic cap). The A-ϕ counters cover the A layer PDTs and are placed between the toroid magnet and calorimeter cryostat. These counters are made of 4.5 degree segments in the ϕ direction and run a length of about 85 cm along the z direction (beam axis). These scintillators are coupled to a wavelength shifting fiber which is connected to a photo multiplier tube for reading out the muon signal. With timing resolution of approximately 4 ns, these scintillators provide an efficient means of triggering on muons as well as rejecting cosmic ray muons which do not arrive at the beam crossing time.

The cosmic cap scintillators cover the top and sides of the C layer of the central muon detector. The primary purpose of this system is to provide a time-stamp for muons already found with WAMUS PDTs. Along with A-ϕ counters, this time information is further used to associate the muons with a corresponding beam crossing and reject background sources like cosmic ray muons. Read out in a similar way as A-ϕ counters, cosmic cap scintillators have a timing resolution of about 5 ns which can be improved using offline corrections down to about 2.5 ns.

The forward region muon system called FAMUS (Forward Angle Muon

Spectrometer) also consists of three layers of detectors called A, B and C layers. However, these layers are made up of a combination of mini-drift tube (MDT) sections for muon track reconstruction and scintillation pixel counters for triggering on muons [46, 47].

FAMUS A layers are composed of 4 planes of MDT tubes whereas B and C layers only have 3 of these planes. Each plane is divided into eight octants as shown in Fig. 3.21 and consists of panels each having eight cells. The individual cells have an internal cross-section of about 1.0×1.0 cm^2 and have a 50 μm tungsten-gold anode wire at the center. The gas mixture present inside the MDT cells is 90 % CF_4 and 10 % CH_4. With a cathode voltage of 3.1 kV, the drift time achieved within this gas mixture is about 60 ns. The MDTs reconstruct the muon track trajectory as determined by the drift time measurement that achieves a position resolution of about 0.7 mm.

The forward muon layers also include a set of scintillation pixel counter layers mounted on the inner face of each MDT layer. Arranged in r-ϕ geometry and divided into eight octant regions (shown in a quadrant view in Fig. 3.22), the scintillation segmentation match the central fiber tracker (CFT) trigger segmentation. Pixel dimensions are designed such that each pixel will cover a 4.5 degree slice in ϕ and have an η segmentation of 0.12 for the 9 large-η rows (closer to beam pipe) and 0.07 for portions of the 3 small-η rows. With timing resolution of better than 1 ns and good $\eta - \phi$ segmentation, these scintillation pixel detectors provide an excellent triggering capability for muons travelling in the forward regions.

In Run II, DØ also included a new shielding around the beam-pipe in the forward regions to reduce the amount of background and the effects of the

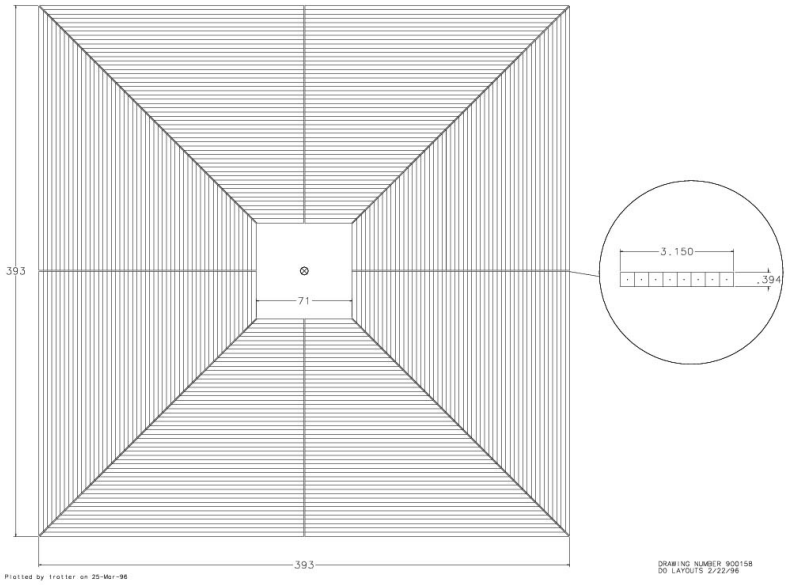

Figure 3.21: End view of one plane of FAMUS mini-drift tube layers divided into 8 octants. The cross-sectional view of an individual MDT tube consisting of eight cells is also shown for more detail.

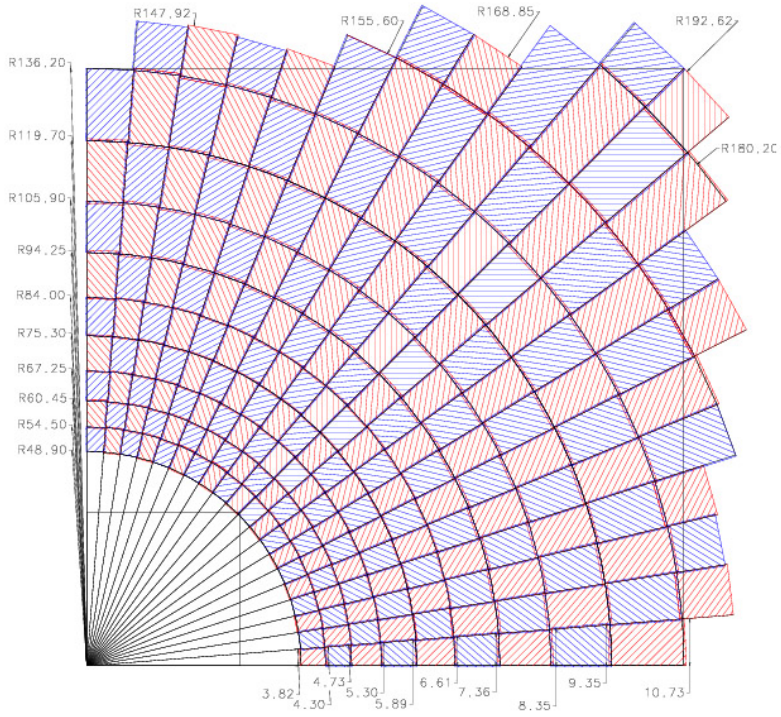

Figure 3.22: End view of a quadrant of FAMUS scintillation pixel layer. Each quadrant is made up of 208 scintillator pixels.

radiation damage to the forward muon systems due to its proximity to the beam pipe.

3.3 DØ Trigger System

The high rate and high luminosity environment at Tevatron requires a selective trigger system to retain the desired events and an advanced data acquisition system to log them on the permanent storage. The average reconstructed event contains about 300 KB data and recording every collision occuring at DØ (at 396 ns beam crossing, the crossing rate is approximately 2.5 MHz) would require about 7.5 GB of disk space for every second of recording. This is perhaps not a big value in today's environment of ubiquitious disk space, but running over years certainly makes this number impossible to handle, requiring about 10^8 GB of disk space per year with only 50 % up time. This is certainly impossible to cope both from the perspective of the availability of resources and the physicists required to analyze this data. Therefore we employ a selective recording system called *triggering* which keeps only a fraction of collider data which seems to have interesting physics implications.

The interaction rate for interesting physics like high-p_T phenomena, electroweak boson production, heavy quark production as well as exotic phenomena outside the Standard Model occur rarely compared to the inclusive proton-antiproton collisions. Therefore, triggering systems at high energy experiments are designed to *trigger* the event recording if some early signatures of interesting objects are found in the event at the run time. Some of the criteria imposed in the trigger are high-p_T tracks in CFT, electron or photon-like

showers in the calorimeter, CPS or FPS, muons or a jet in the calorimeter as well as advanced objects like a b-tagged calorimeter jet. Such criteria can also be required in combinations to provide more refined or topological signatures.

DØ 's trigger framework consists of a three-level sequential structure resulting in a final recording rate of 50 Hz as shown in Fig. 3.23, [48]. An initial Level 0 (L0) trigger also exists to trigger the presence of an inelastic collision. L0 is also used for luminosity determination purposes. The Level 1 (L1) trigger system is composed of a combination of hardware based trigger algorithms which bring an event rate reduction of about 1/500 while keeping high acceptance for leptons and jets in the event. In order to be able to keep up with the collision rate without introducing any deadtime, the L1 system makes decisions in about 4.2 μs during which all trigger information from successive interactions is kept in a data pipeline.

Level 2 (L2) trigger system is also made up of software triggers based on L1 outputs which analyze the events triggered by an earlier L1 accept and makes decisions in about 100 μs.

The last level of trigger system, Level 3 (L3) is also a software trigger based on fully digitized signals and serves the purpose of a high-level event filtering that is instrumental in keeping the final data rate to tape at about 50 Hz.

Due to data recording and processing limitations, the final rate to tape is limited. If the triggers and event filter algorithms are not sufficient to meet this rate limitation, acceptable events have to be thrown out regardless of their content. This is called *prescaling* and applied on an individual trigger

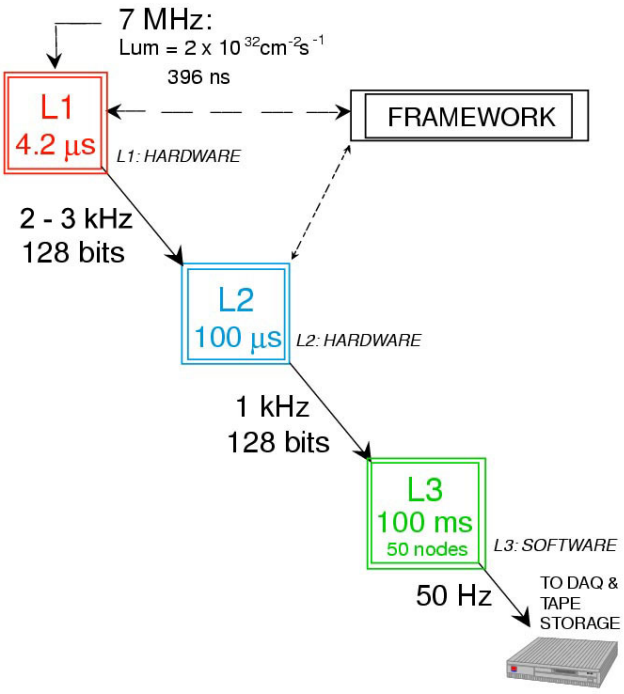

Figure 3.23: Three levels of the sequential triggering system employed at DØ . Input and output rates at each trigger level are also shown on the figure.

basis. If a trigger is accepting more data than the bandwidth allocated, the data acquisition coordinator is generally forced to match the available bandwith by allowing some fraction of the events to be thrown away. For example, if a trigger is assigned a prescale of 10 at a certain luminosity, this means that only one event out of 10 that pass this trigger will finally be accepted (triggered). This is, of course, an undesirable situation and a lot of effort has been made to minimize such cases.

3.3.1 Level 1 Trigger

The Level 1 (L1) trigger at DØ is a hardware based system filtering the 2.5 MHz event rate to an output of 2 - 3 kHz for input to Level 2 system [49]. There can be up to 128 distinct L1 triggers in operation, each setting an identifying hit if satisfied. The total time it has to make a trigger decision in all 128 trigger bits is 4.2 μs. The L1 trigger system contains a trigger framework which combines the trigger information coming from subdetectors like the central fiber tracker, central and forward preshower detectors, calorimeters and muon scintillation counters. The data flow for L1 trigger system (as well as L2 system) is shown in the block diagram of Fig. 3.24.

Due to the short time allowed for decision making at L1, only the simplified presentations of physics objects like electrons, muons, calorimeter towers and tracks are used. Each L1 subdetector trigger manager reports a list of trigger terms to the trigger framework depending on the trigger information coming out of the corresponding subdetector. Some of the most common L1 triggers make use of the following set of trigger information;

- Calorimeter pseudo-rapidity projective tower counts over certain EM or

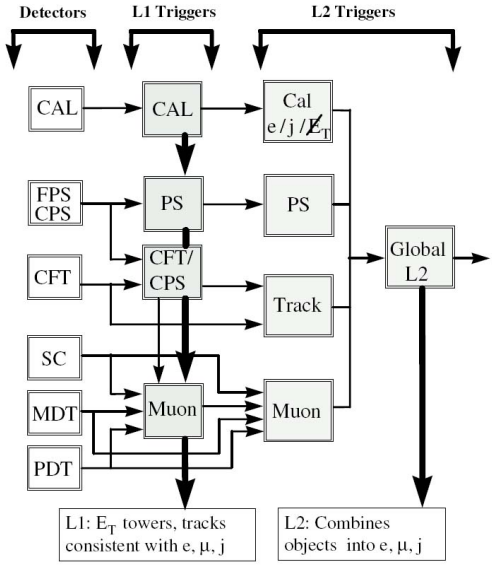

Figure 3.24: Block diagram showing the basic data path for Level 1 and Level 2 trigger systems.

hadronic transverse energy thresholds as well as the missing transverse energy in the calorimeter.

- Counts of central tracks made up of only axial layers of the central fiber tracker, sorted into several transverse momentum bins.

- Counts of preshower detector clusters in the central and forward regions.

- Central and forward muons in various p_T bin and pseudo-rapidity regions as well as the quality indicators based on the number of hits. The muon trigger also makes a crude central track matching to the scintillator hits in the muon detectors.

3.3.2 Level 2 Trigger

The Level 2 trigger system makes a more refined trigger decision at the hardware level using the trigger information coming from different sub-detector L1 trigger systems. The system makes trigger decisions in about 100 μs and reduces the event acceptance rate further down to 1 kHz using multi-detector correlations of trigger level objects found in the events.

The L2 system uses two distinct stages to make a trigger decision; pre-processor stage and the global processor stage [48]. In the pre-processor stage, each subdetector L2 pre-processor prepares a list of trigger objects available from the L1 trigger information using a set of correlation algorithms. These pre-processors currently exist for calorimeter, silicon and fiber trackers, muon detectors and the preshower detectors. Some of the L2 trigger algorithms applied by corresponding subdetector pre-processors can be summarized as;

- Calorimeter jet reconstruction in 5×5 groups of calorimeter trigger towers based on a basic jet cone algorithm. Available information for jets are kinematic variables like jet E_T, η and ϕ.

- Calorimeter level electron and photon reconstruction algorithms. These L2 algorithms find seed calorimeter towers and compares the total tower energy to the energy from the electromagnetic layers alone and based on this information the pre-processor makes a trigger decision for an electromagnetic (electron or photon) object.

- Calorimeter pre-processors can also make missing transverse energy calculations by summing the transverse energy of the individual trigger towers vectorially and checking for non-zero observed total transverse

energy.

- Transverse momentum ordered sets of L2 CFT tracks based on L1 central fiber trigger information. Tracks with silicon hits are also reconstructed using the L1 CFT tracks as the seed.

- Tracks not emanating from the primary vertex are found, giving the ability to trigger on long-lived particles like b-quarks.

- Computation of the preshower cluster ϕ and η to be used for matching to electromagnetic towers in the calorimeter as well as with the tracks found by the central fiber tracker.

- More precise muon trigger computations with better calibration and timing from scintillators. Muon tracks at L2 have η and ϕ information as opposed to the quadrant information available at L1.

3.3.3 Level 3 Trigger

The Level 3 trigger is a software based trigger system based on fully digitized outputs from the detectors with parallel data paths transferring data from the front end crates to a farm of processors [48]. Level 3 event filtering reduces the L2 output rate of 1 kHz to about 50 Hz in about 100 ms. The L3 processors apply a set of event filters utilizing high-level physics algorithms resembling the more refined offline object reconstruction and better correlations between object seeking for specific event topologies. Due to its software infrastructure, there is a wide variety of filter tools available for L3 and the sophistication of the trigger algorithms is roughly comparable to a basic offline analysis.

The filtered events accepted by L3 are stored on tapes for offline event reconstruction and data analysis. Average data storage per event is about 300 KB [5]. There are current plans to increase the L3 output bandwidth at DØ to 100 Hz which will essentially enable data taking without having to impose more restricted trigger filters at increased luminosities.

[5] 1 KB is 1024 bytes (1 byte = 8 bits)

Chapter 4

Offline Event Reconstruction at DØ

The events recorded by the data acquisition system are kept in a RAW format which contains the digitized information from detector sub-systems like the hits in the tracking and muon systems and the digitized counts in the calorimeter cells. In order to convert this raw information to more fundamental physics objects like electrons, and provide useful kinematic as well as quality information, the recorded events are processed through a set of computer algorithms called the offline event reconstruction. the DØ reconstruction system; DØRECO , is composed of large object-oriented algorithms producing the useful physics information used in various physics analyses [50].

In the next few sections, we will give more detailed accounts of how the reconstruction is performed but in summary the DØRECO software performs the following tasks;

- *Hit finding* — The digitized signals from the wires and strips of the tracking detectors are converted to spatial locations of hits. In addition, calorime-

ter signals, combined with appropriate calibration, are translated to energy depositions in calorimeter cells.

- *Tracking and Clustering* — At this stage, the hits from the tracking are combined to define the particle trajectories, i.e. tracks. From the curvature of the tracks in the known solenoid (or toroid for muon system) magnetic field, we also measure the momentum of the particles. Besides the formation of tracks, calorimeter cells and preshower hits are also grouped into clusters representing the total energy depositions by objects in these detectors.

- *Particle Identification* — After particle signatures are found in the form of tracks, calorimeter energy depositions or muon system segments, a set of higher level reconstruction algorithms categorize them into candidates of electrons, photons, muons and jets.

4.1 Track Reconstruction

The DØ detector has two main tracking components; an innermost silicon microstrip detector (SMT) arranged in barrel and disk geometry, and a scintillating fiber detector (CFT) with cylindrical layers surrounding the SMT. Both of these detectors provide strip hits along the trajectory of the charged particles, which are later fed into algorithms to reconstruct the original particle trajectory and make momentum measurements (Fig. 4.1).

4.1.1 Hit Reconstruction

Adjacent silicon and fiber strips above a certain threshold are grouped into a silicon or fiber cluster respectively. In SMT, the center of a cluster is defined to be the charge-weighted average of the strip positions in the cluster [51].

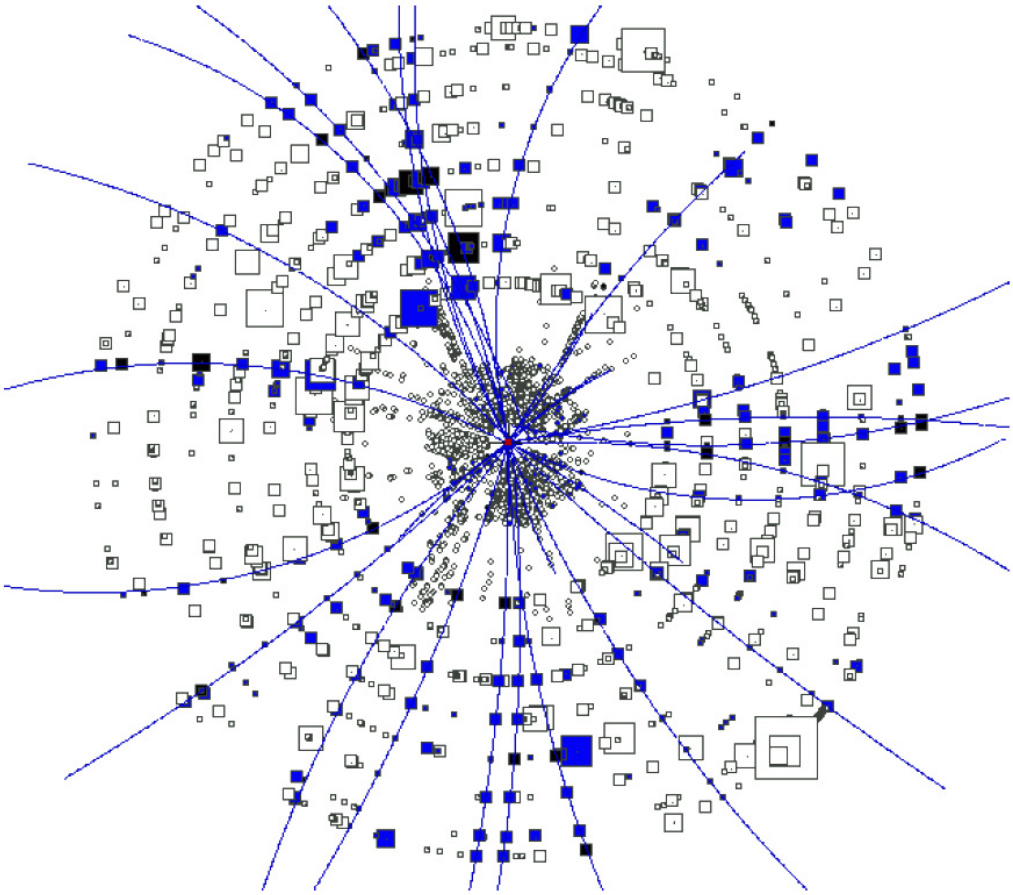

Figure 4.1: And end view of the central tracking systems with a live recorded event showing the hits and the tracks reconstructed. CFT hits are represented by squares and SMT hits are shown as little circles in this display. Hits are colored if they are associated with a reconstructed track. Reconstructed tracks are shown as solid lines and they are curved due to the presence of the solenoid magnetic field pointing perpendicular to the page.

In the SMT, the electrons and holes do not move directly to the silicon strips along the direction of the applied electric field because of the existence of the 2T magnetic field. Instead, they drift at an angle called the Lorentz angle, depending on the magnetic field strength and electron or hole mobility. The center of each silicon cluster is corrected for the average Lorentz angle measured for electrons and holes [1]

Particles going through the silicon strips create clusters on both p-side and n-side of the wafers[2], which are then combined to determine the location along the strips where the particle has passed through. The position of the hit can be reconstructed to as good as 10 μm in the axial direction (along x-y axes) and 35 μm in the z-direction.

Fiber tracker clusters, on the other hand, are mostly either single-fiber clusters (singlet) or doublet clusters containing one fiber from each sub-layer of the doublet-layer. By using the geometry of the doublet-layers, hit resolutions are $\leq$ 100 μm in the axial direction and about 2 cm in the z-direction. Even though the CFT hit resolution is worse than the innermost SMT detector, the addition of CFT hit information improves the impact parameter (point of closest approach to the primary vertex or beam axis) of the reconstructed tracks significantly as seen in Fig. 4.2.

4.1.2 Pattern Recognition

The pattern recognition in the central tracker is performed to reconstruct the tracks from the hits in the SMT and CFT. The trajectories of charged particles

[1]The Lorentz angle is measured to be about 4 degrees for holes and 18 degrees for electrons. The difference is due to the different mobilities of holes and electrons (holes are slower than electrons).

[2]The strips on p and n-sides of the silicon have a stereo angle.

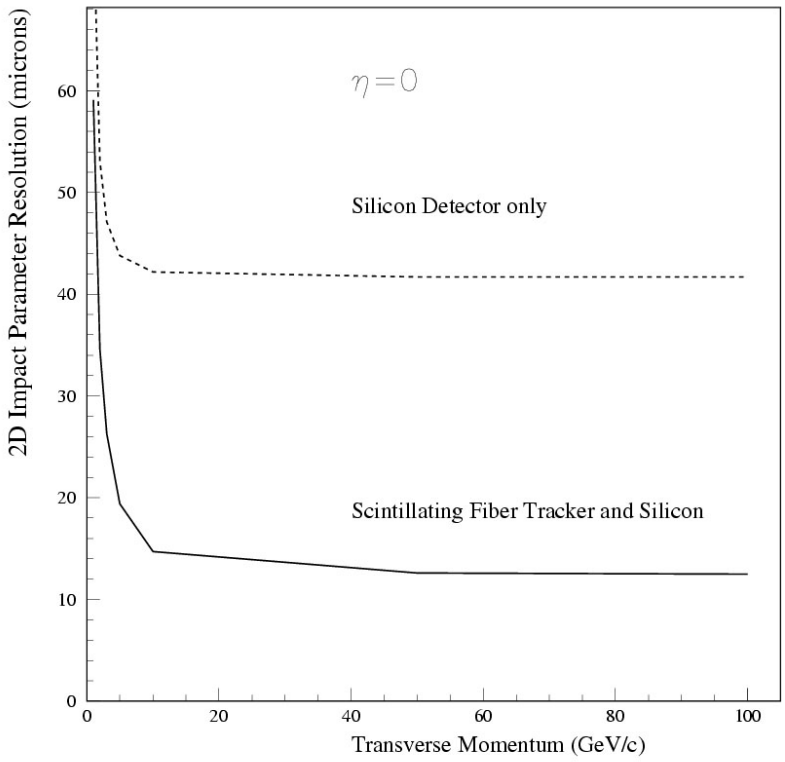

Figure 4.2: The expected resolution of 2D (x-y) impact parameter of the reconstructed tracks in simulated high-p_T top quark events as a function of track transverse momentum (at normal incident to the cylindirical surfaces of the trackers). Dashed line shows the impact parameter resolution of the tracks reconstructed only using the silicon tracker (SMT) hits. The improvement in the resolution is clearly seen from the solid line where fiber tracker (CFT) hit information is added to the track reconstruction [37].

take the shape of helices in the presence of a magnetic field along the z-axis and the curvature of the tracks provides the momentum measurement. The imperfections of the magnetic field especially toward the end of the solenoid magnet as well as the energy loss due to the detector material are well accounted for through careful surveys.

DØ currently utilizes two algorithms for track reconstruction. These are called Histogramming Track Finder (HTF) [52] and Global Tracking via Road Approach (GTR) [53].

The HTF algorithm is based on forming track templates using Hough transform technique [54] and local road finding. The technique works by tracing circular (in the transverse plane) trajectories from the origin and creating a histogram of hits in these possible trajectories. A trajectory with n points exhibits itself as a peak of height n. Each trajectory keeps track of the hits contributing to it and not shared between different possibilities. Sets of hits contributing to peaks in these histograms are taken as initial track candidates. The number of such trajectories is linearly proportional to the number of hits. In the HTF method, the track candidates are finally fitted in three dimensions and filtered using a Kalman filtering algorithm [55].

The HTF reconstruction works in two passes. The first pass begins with SMT only tracks[3] and then extrapolates these tracks to CFT hits. The second pass first builds tracks from CFT hits and extrapolates the track back to SMT. Using both sequences of track finding and combining the results increases the tracking efficiency by providing flexibility in the number of hits found in a specific tracking component.

The GTR algorithm starts the track reconstruction from the track *stubs*, curved track segments extending between two hits which are also consistent with coming

[3]Tracks with only SMT hits.

from the interaction point. The stubs are usually required to be from the two outer layers of the CFT or SMT but other special cases are allowed, especially to cover the regions with SMT disks. Each stub defines the direction of a road within which an extrapolation is made to other hits in the tracking detectors. If hits are found within the search window, the new hits are combined to the former set of hits and the track is re-fit using the Kalman filtering algorithm.

The final set of reconstructed tracks is composed of tracks found by both algorithms. In the case that two different tracks from each algorithm use a common hit point, the hit is assigned to the track with the larger number of hits and the other track is discarded. If the number of hits on both tracks is the same, then the track with the lower fit χ^2 is kept. The final candidate tracks are then re-fit to their hits and their track parameters and parameter errors are calculated.

Reconstructed tracks are represented with 5 helix parameters (as well as the 5×5 error matrix) defined at a specific space location which is usually taken as the distance of closest approach (DCA) to the (0,0,0)[4]. These track parameters are:

- r_0 : The distance of closest approach (DCA) to the z-axis in the x-y plane.
- z_0 : z-position of the track at the distance of closest approach to the origin.
- ϕ : Direction of the track in the transverse plane at the distance of closest approach.
- $\tan\lambda$: Tangent of the polar angle for the track direction.
- q/p_T : Charge (q) over transverse momentum of the track which is also called the curvature. Curvature of a track is calculated from the bending in the magnetic field.

[4]After the reconstruction of primary vertex, the track parameters are propagated to the new DCA consistent with the new vertex.

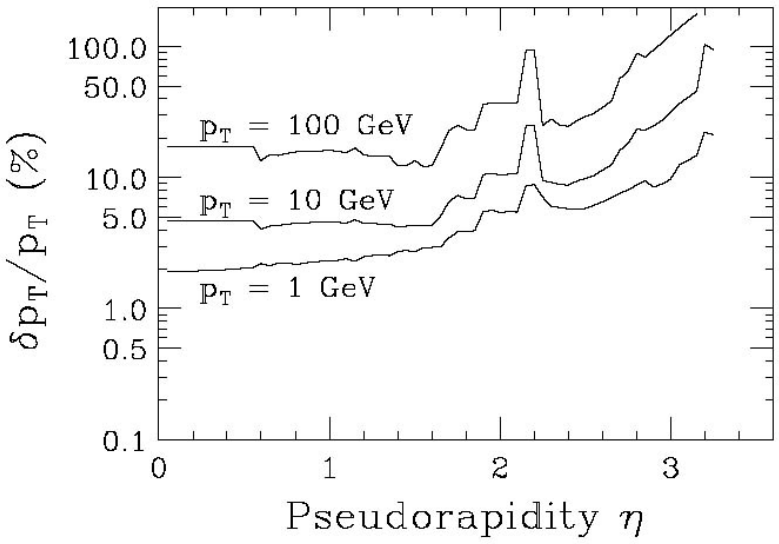

Figure 4.3: Fractional track transverse momentum resolution is given as a function of track pseudo-rapidity for three momentum ranges in the simulation, [37].

The momentum resolution of the reconstructed tracks is shown in Fig. 4.3 and can be parametrized for tracks at normal incident to the tracking detector surfaces ($\eta = 0$) by Eq. 4.1.

$$\frac{\Delta p_T}{p_T} = \sqrt{0.015^2 + (0.0014\ p_T)^2} \tag{4.1}$$

As seen in Fig. 4.3, the decrease in the momentum resolution above $|\eta| > 1.6$ is due to the limited CFT coverage (shown as an increase in the error). On the other hand, the resolution suddenly becomes better around $|\eta| \sim 2.2$ where the forward SMT disk coverage begins. The efficiency of track reconstruction for muons in the simulated decays of Z boson is also shown in Fig. 4.4. Although it is known to be higher than real data, the track reconstruction efficiency is about 96.9 % for high-p_T tracks in simulation.

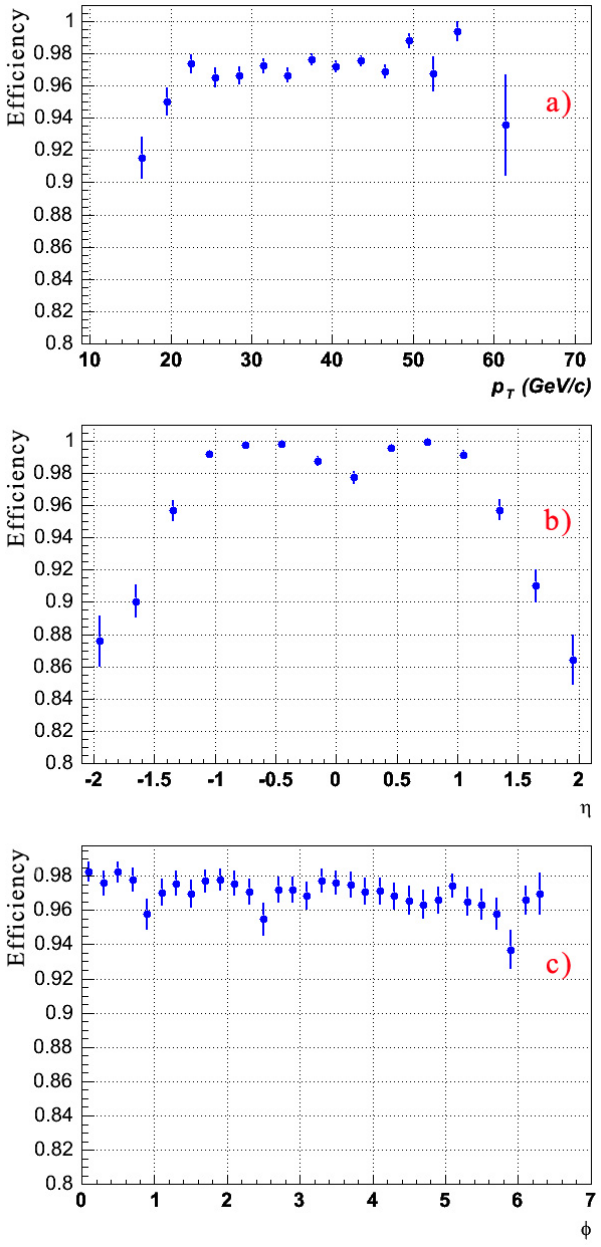

Figure 4.4: Track reconstruction efficiency for high-p_T muons in simulated decays of Z boson. Tracking efficiency as a function of muon a) p_T, b) η and c) ϕ are shown. The average track reconstruction efficiency is 96.9 %.

4.2 Primary Vertex Reconstruction

At a luminosity of about $10^{32}\text{cm}^{-2}\text{s}^{-1}$, an average of 2.5 additional minimum bias interactions are expected to occur accompanying each hard-scattering collision. Primary vertex (PV) reconstruction is performed to find and distinguish this hard-scattering vertex from the other minimum bias interaction vertices.

The reconstruction algorithm is a three-step process. In the first step, tracks are selected based on their DCA. In the second step of the reconstruction process, possible vertex candidates are assembled. Finally in the last step, the most probable primary vertex is distinguished from the other vertices and selected as the hard scatter vertex for the collision. After the primary vertex is reconstructed, track parameters which were originally computed at DCA with respect to the detector origin are recalculated with respect to the event primary vertex [56] - [58].

Track selection is performed to distinguish tracks emerging from the hard-scatter vertex from those due to the secondary decays of particles. At the track selection stage the hard-scatter vertex is not known but the nominal vertex location is known to be within the transverse beam size. For this reason, a loose two dimensonal DCA significance cut is applied to tracks in order to remove secondaries as in Eq. 4.2. These tracks are fed into the first pass of the vertex reconstruction algorithm which determines the approximate location of the beam spot.

$$\text{Significance} \equiv \frac{DCA}{\sigma_{DCA}} < 100.0 \tag{4.2}$$

The first pass vertex reconstruction makes a better choice for the origin of the collision and the track parameters are recalculated with respect to this new vertex. With the new parameters calculated for the tracks, a tighter DCA significance cut of 3 is applied to tracks. Selected tracks are fitted together and the χ^2 contribution of each individual track to the vertex is computed. If the vertex fit χ^2 is larger

than 10, the track with the highest χ^2 contribution is excluded and the vertex is re-fitted. This process is repeated until the vertex fit χ^2 becomes less than 10. Once a vertex has been found, this procedure is repeated using the remaining tracks in the event. After the reconstruction process is over, a list of reconstructed vertices is generated and passed to the vertex selection procedure.

As we mentioned before, not all the vertices found in the event represent the hard-scatter point. In order to distinguish the hard scatter vertex from other minimum bias vertices, a probabilistic method is used. This selection uses the fact that tracks from minimum bias interactions have smaller transverse momenta than tracks from the hard scattering vertex. The track transverse momentum distributions shown in Fig. 4.5 for MC tracks, are used to define a probability which describes the likelihood for a track to come from a minimum bias vertex. Only the tracks with $p_T > 0.5$ GeV are used for the construction of the probability.

The track probabilities are obtained from $Z \rightarrow \mu\mu$ events obtained in real data; the hard-scatter vertex is assumed to be the vertex reconstructed from the two high-p_T muons and other vertices found in these events are considered as minimum bias vertices. In order to create a vertex probability, the track probabilities are multiplied and the product is weighted appropriately to make it independent of the track multiplicity. This vertex probability describes the likelihood of the vertex to be produced as a result of a minimum bias interaction and the vertex candidate with the lowest probability is chosen as the primary vertex.

The combined primary vertex reconstruction and selection efficiency is about 97% in dimuon (mostly J/ψ events) data events and about 99% in Monte Carlo simulation.

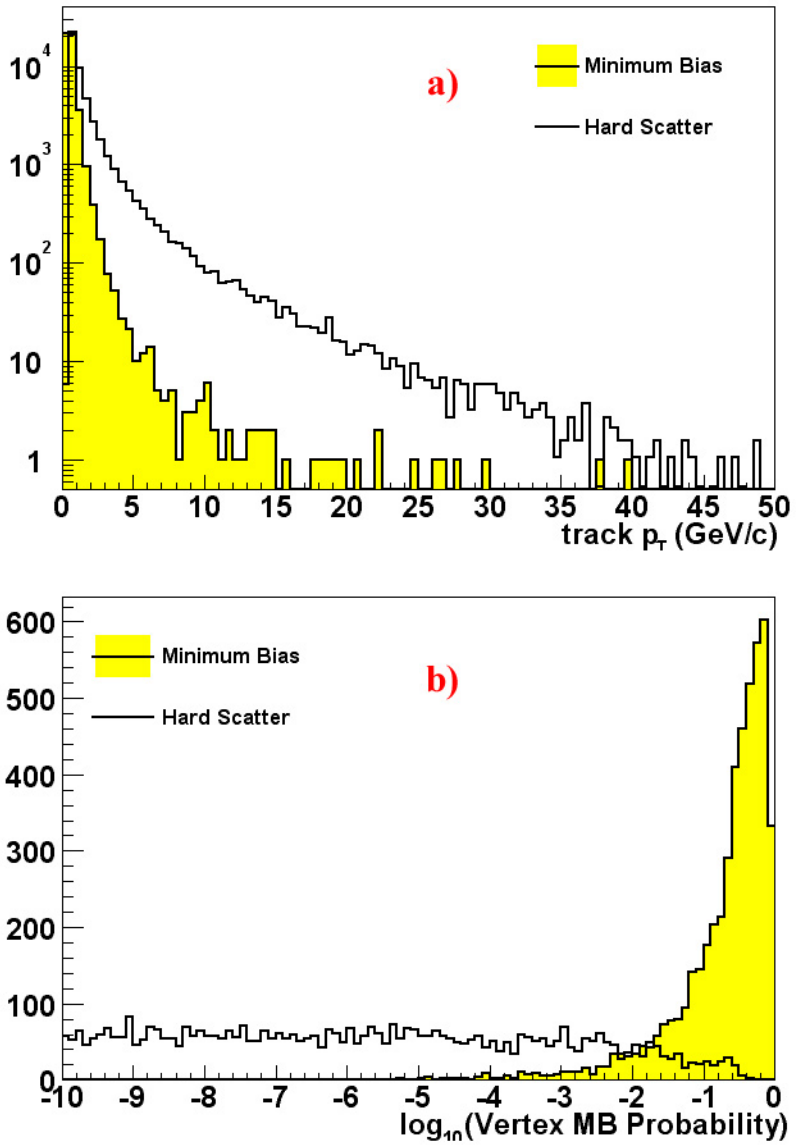

Figure 4.5: Transverse momentum distributions of tracks are compared in the upper plot (a) for tracks coming from the hard-scatter vertex and the minimum bias interaction generated by MC. This distribution is used to create a probability, as shown in the lower plot (b), that describes the probability of a track to be associated with a minimum bias vertex.

4.3 Muon Reconstruction

The reconstruction of local muon[5] tracks in the muon system start with the digital information coming from the drift tube wires and scintillator hits. This raw data is transformed into position and timing information in the scintillators and the drift wires. The combination of wire and scintillator hits in each layer of the muon system results in small tracks which are called segments. Finally, the individual layer segments are combined via fitting procedures to form local muon tracks and their momentum is measured using the magnetic field provided by the toroid [59].

4.3.1 Hit Reconstruction

As described in the previous chapter, the muon system is composed of a series of drift tube and scintillator detectors. The central region is composed of three concentric layers of proportional drift chambers (PDT) and two layers of scintillator counters (MSC). The forward region muon system is also composed of three layers of mini-drift tubes (MDT) and each drift tube layer has an associated scintillator layer called pixel counters.

Due to their different construction and operating principles, the hit reconstruction procedures also differ among these detectors. The scintillator detectors in the central and forward regions provide timing information for muon hits. Their fast response (time resolution is about 1-2 ns) enable the measurement of the arrival of the time of the signal.

The hit reconstruction in the drift tubes utilizes the information coming from the drift time of the signal reaching the wires in the middle of the detectors. The

[5] "Local muon" is a term used to describe the muons reconstructed from only the muon detector information. Similarly a "global muon" is reconstructed by using the muon detectors as well as the calorimeter and the central trackers via special matching algorithms.

relation of drift time and distance depends on the incident angle of the muon track which created the hit and for this reason, the first hit reconstruction assumes an incident angle of zero (perpendicular the the wire axis). A more precise, second-pass hit reconstruction is performed once the track segments are reconstructed and the muon trajectory is available.

4.3.2 Segment Reconstruction

The segment reconstruction finds straight[6] track sections (i.e. segments) in each layer of the muon detector. The reconstruction algorithm starts with the wire hits and these reconstructed track segments are matched to the nearby existing scintillator hits for an updated position measurement of the segments [60].

For the segment reconstruction, the central and forward muon systems are divided into two parts according to the octant positions as shown in Fig. 4.6.

- Octant # : 0, 3, 4 and 7 (WAMUS and FAMUS)
- Octant # : 1, 2, 5 and 6 (WAMUS and FAMUS)

This discrimination is based on the orientations of the wires in the corresponding octant parts of the detectors. Both in WAMUS and FAMUS, the wires are oriented along the y-axis (octant numbers 0, 3, 4 and 7) or along the x-axis (octant numbers 1, 2, 5 and 6). However, the wire plane is in the x-z or y-z plane in WAMUS while in FAMUS, this is the x-y plane. To overcome these differences in different sections of the muon detectors, the segment reconstruction is not performed in the global system but in the local muon systems. This choice of reference system requires the transformation of the reconstructed hits from global system to the local system.

The track segment reconstruction is performed in 6 steps:

[6]Magnetic field penetration at the muon layers is negligible.

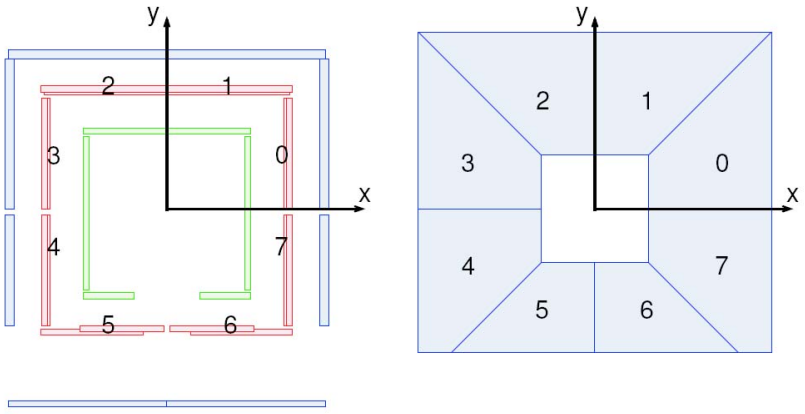

Figure 4.6: End view of the muon chambers and the octant numbering in WAMUS (left) and FAMUS (right). The wires are oriented along the y-axis in octants 0, 3, 4 and 7 whereas they are oriented along the x-axis for octants 1, 2, 5 and 6.

1. Transformation of global hits to local hits
2. Creation of links between the hits and forming local segments
3. Fitting of local segments
4. Using primary vertex constraint for A-layer segments
5. Filtering of the local segments based on the fit χ^2 and on the number of hits per segment
6. Transformation back to the global system

In the A-layer, where the chambers consist of four planes of drift tubes, the typical number of hits for a segment is 3 or 4. In the B and C-layers, where the chambers are made up of three planes of drift tubes, the typical number of hits is 2 or 3. An illustration of the segment finding is shown in Fig. 4.7. After the segment fit has converged and the direction and position of the segment have been

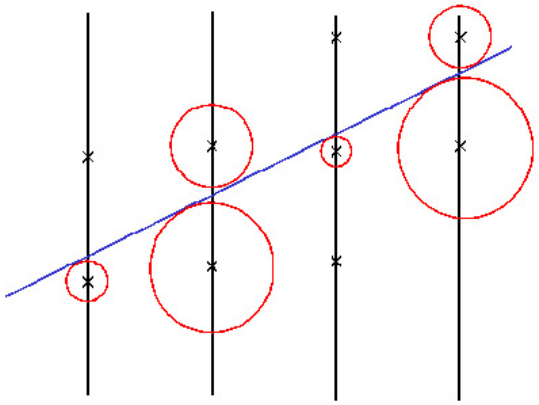

Figure 4.7: Schematic view of segment finding from a collection of wire hits in a layer. The lines represent the central planes of the muon chamber layers and wires are presented with crosses. Circles indicate the distance from the wire determined by the drift time.

calculated using the wire hits, the scintillator hits are matched to the segment by extrapolating the segment to the scintillator plane. If a matching scintillator hit is found, the segment is refitted, now using all the information coming from the wire hits as well as the scintillator hits.

Segments are initially reconstructed in the individual layers of the muon system separately (A, B and C layers). However, the segments from B and C layers are expected to be the parts of the same straight line due to the lack of the magnetic field and material in these layers. Therefore, each pair of reconstructed B and C-layer segments in the same octant and region are combined and a new fit is performed using all hits in both segments.

4.3.3 Local Track Reconstruction

The local muon track reconstruction [61] (i.e. only from the muon detectors) performs the final matching of the pair of track segments from A and BC layers

and makes a momentum measurement using the amount of bending of the muon track in the toroid magnetic field. The fitting algorithm reconstructs the track by relating the directions of the two segments in the global system and the bending through the magnetic field. The reconstruction also takes into account effects of multiple scattering and the energy loss due to the iron toroid.

The reconstruction of local muon tracks is performed in the following stages:

- Grouping of track segments. All possible segment pairs are considered starting from an A segment and defining a road which is extended to the BC segment.

- Perform first momentum estimation from the matching segments using simple toroid geometry as shown in Fig. 4.8. For this first estimate the magnetic field of the toroid is assumed to be constant at 1.8 T and the energy loss in the toroid iron is taken as $dE/dx = 0.016$ GeV /cm.

$$p = \frac{0.3\ B\ D}{|\tan\ v|} \tag{4.3}$$

  Eq. 4.3 shows the relation between the bending angle v between the two segments and the muon momentum[7] in the drift plane perpendicular to the wire direction. D is the estimated distance of the muon travel inside the toroid as shown in Fig. 4.8.

- Using the first estimate of the track parameters, perform a non-linear fit to find the best momentum compatible with A-layer and BC-layer segment positions and directions in the local frame. The track is propagated step by step from the center of BC segment to the center of A segment using helical trajectories. At each step and energy loss correction is applied using a more realistic dE/dx formula which varies as a function of the muon momentum.

[7]Momentum in units of GeV/c when magnetic field is in Tesla and distance of travel is in meters.

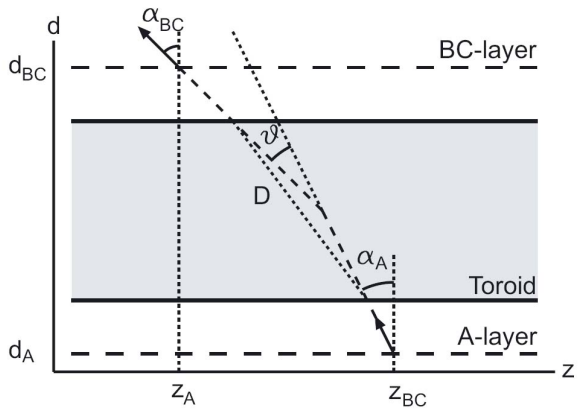

Figure 4.8: First estimation of the track momentum by calculating the amount of bending (angle v) through the toroid magnetic field.

- Reconstructed local muon tracks are filtered depending on their proximity to other found tracks and fit χ^2. A loose χ^2 cut is applied to tracks for cleaning up bad fits. If several tracks are found too close to each other, the reconstruction algorithm only keeps the one with best χ^2.

4.3.4 Global Muon Reconstruction

Besides the local muon track reconstruction performed in the muon chambers, muon tracks are also detected and reconstructed as tracks in the central tracker system. However, the central tracker alone makes no distinction between all the charged particle types and cannot provide a discrimination for any charged particle versus a muon. However, the much better momentum and position resolution provided by the central tracker detector (shown in Fig. 4.9) necessitates a clever algorithm which matches the two tracks found in these two separate detectors. This matching procedure is called the global muon reconstruction [53].

The global muon reconstruction algorithm considers the following effects;

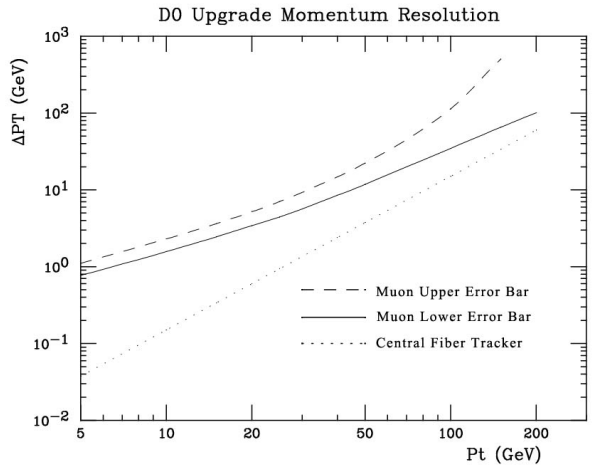

Figure 4.9: Momentum resolution of the muon system compared to the Central Fiber Tracker resolution [45].

- The magnetic field of the solenoid and full track trajectory
- Effects of multiple scattering and energy loss in the calorimeter

The matching of the central muon track and local muon track is performed at the A-layer of the muon detector. Since the central track parameters are given at the distance of closest approach (DCA) to the primary vertex, the central track parameters are propagated to the A-layer of the muon detector. The matching is performed both in ϕ and η coordinates.

$$\Delta\phi\ (\mu, track) = \phi_{\ \mu} - \phi_{\ track} \tag{4.4}$$

$$\Delta\eta\ (\mu, track) = \eta_{\ \mu} - \eta_{\ track} \tag{4.5}$$

In Eq. 4.4, $\phi_{\ track}$ is corrected for track propagation since it is generally given at DCA. The propagation is performed as in Eq. 4.6 where R_{sol} is the radius of the solenoid magnet (0.6 m) and B is the magnetic field of the solenoid (2T).

$$\phi_{A-layer} = \phi_{DCA} + 0.3 \times R_{sol} \frac{q\ B}{p_T} \tag{4.6}$$

For tracks with stereo information, $\eta_{\ track}$ is calculated from the track helix parameter $\tan\lambda$, however since there is no z information for axial tracks, the matching is only carried out by using the $\Delta\phi$ between the track and local muon.

A more detailed account of the $\Delta\phi$ and $\Delta\eta$ residuals is given in [53] and these studies show that the matching should be done as in Eq. 4.7 for tracks with stereo information or in Eq. 4.8 for axial tracks.

$$\Delta R = \sqrt{\left(\frac{\Delta\phi}{0.2}\right)^2 + \left(\frac{\Delta\eta}{0.2}\right)^2} < 1 \tag{4.7}$$

$$\Delta R = \sqrt{\left(\frac{\Delta\phi}{0.2}\right)^2} < 1 \tag{4.8}$$

In the case of two tracks matching a single muon, the track with the highest transverse momentum is used.

4.3.5 Muon Identification

After the reconstruction of local and global muons, the muon identification [62] is performed to categorize the muons for offline analysis. The muon identification classifies the reconstructed muons based on the grades of the local muon track fit and hit properties as well as the result of the global matching.

There are two sets of muon qualities, first is called "*nseg*" for historical reasons and it classifies the muons depending on their global matching status and the local muon information. Available *nseg* definitions are given below:

- ***nseg* = 3** — The local muon is reconstructed from matching A-layer and BC-layer segments. The local track is also matched to a central track as described in the previous section.

- *nseg* **= 2, 1** — The local muon track reconstruction fails for this type of muons and they are represented by a single A-layer (*nseg* = 1) or BC-layer (*nseg* = 2) segments. However, there are central tracks found matching with these type of segments making possible muon candidates.

- *nseg* **= 0** — Both the local muon track reconstruction and segment reconstruction fails for these types of muons and they are only represented by individual hits in the muon chambers. However, these hits are matched to tracks from the central tracker sytem

- *nseg* **= -1, -2** — The local muon track reconstruction fails for this type of muons and they are represented by a single A-layer (*nseg* = -1) or BC-layer(*nseg* = -2) segments. There are no matching central tracks found for this type of muons.

- *nseg* **= -3** — The local muon is reconstructed from matching A-layer and BC-layer segments. However, the local muon track is not matched to a central track.

As seen in the *nseg* descriptions given above, $nseg \geq 0$ represents different qualities of local muons with a matching central track whereas negative *nseg* values mean that there are no central tracks found for the local muons.

The second classification scheme for muons is again based on the local muon track as well as central track matching information and they represent the "grade" or the "quality" of the reconstructed muons. Available quality definitions are given below:

- **Tight Muons** — Only $|nseg| = 3$ muons can be tight and they need to satisfy the following criteria:

  - at least two A-layer wire hits

  - at least one A-layer scintillator hit
  - at least three BC-layer wire hits
  - at least one BC-layer scintillator hit
  - a converged local track fit ($\chi^2 > 0$)

- $|nseg\ | = 3$ **& Medium / Loose Muons** — If an $|nseg| = 3$ type muon fails the tight criteria above, it is considered for the looser criteria called medium and loose respectively. An $|nseg\ | = 3$ muon is medium if it satisfies the following criteria:

  - at least two A-layer wire hits
  - at least one A-layer scintillator hit
  - at least two BC-layer wire hits
  - at least one BC-layer scintillator hit

  An $|nseg\ | = 3$ loose muon is defined as a medium muon but allowing one of the above requirements to fail, with the A-wire and scintillator requirement treated as one condition, and always requiring at least one scintillator hit.

- $nseg$ **= +2 & Medium / Loose Muons** — Muons with $|nseg\ | < 3$ can only be loose or medium if they are matched to a central track. An $nseg\ = 2$ muon is a BC-layer segment only muon with matching central track and it is considered loose if it satisfies:

  - at least two BC-layer wire hits
  - at least one BC-layer scintillator hit

  An $nseg\ = 2$ muon is defined as medium if it satisfies the above conditions and if it is located in the bottom part of the detector where A-layer coverage is missing (octants 5 and 6 and $|\eta| < 1.6$.

- *nseg* = **+1 & Medium / Loose Muons** — Muons with *nseg* = 1 are made of A-layer segment only muon with matching central track and it is considered loose if it satisfies:
  - at least two A-layer wire hits
  - at least one scintillator hit

  Low momentum *nseg* = 1 muons can be defined as medium. Such a muon is considered as low momentum if its probability to reach the BC-layer is less than 70 %.

This second set of muon quality classifications are inclusive definitions; i.e. if a muon is tight it is also a medium as well as a loose muon.

4.3.6 Muon Reconstruction and Trigger Efficiencies

In the analysis of this thesis, we use central track-matched loose muons because of their higher efficiencies. In order to measure the reconstruction, as well as the trigger efficiency of muons, we study the Z boson production where Z decays into two muons. Due to their distinct invariant mass spectrum, these muons provide high purity efficiency measurements.

Before making efficiency measurements, we collect Z candidate events by requiring one central track-matched muon and a second central track with no muon-id required. The pre-selected muon which is matched to one of the tracks is called the tag muon and used to increase the purity of the selected Z candidate events. The other track in the event (probe) with no information regarding its nature (muon or another particle) is tested against the found muons in the muon chambers and the muon triggers. For measuring efficiencies, we do not consider the tracks pointing towards the bottom of the muon detector (octants 5 and 6, $|\eta| < 1.6$) where acceptance is lower as compared to other regions.

The selection of the tag muon and the probe track is illustrated in Fig. 4.10. Z candidate events are collected by requiring at least two tracks one of which is matched to a tag muon. The tag muon is required to be a central track matched loose muon. Both tracks are required to have transverse momentum p_T, larger than 15.0 GeV and pseudo-rapidity $|\eta|$ within the muon system coverage i.e less than 2.0. Both tracks are required to be isolated in the calorimeter and the central tracker [8]. The events for these two track Z candidates are required to fire single muon triggers with following conditions:

- **Level 1**: A region W (wide muon region) single muon trigger with tight scintillator and loose wire requirements.
- **Level 2**: One muon with $p_T > 3.0$ and medium quality requirements for data taken with trigger list versions before 12. For trigger list version 13, there is no L2 requirement.
- **Level 3**: At least one global track of $p_T > 10.0$ found with SMT and CFT trackers. A minimum number of 8 hits is required for the track.

In order not to bias the probe muon from this requirement, we require that the control muon is matched to a L1 muon, L2 muon and the L3 track described above. To increase the purity of the probe track even further, we require that the probe track is matched to a calorimeter energy deposition which is consistent with a muon MIP[9] signature in the calorimeter. This requirement on the probe track does not bias the efficiency measurement since the calorimeter and the muon detectors are independent.

[8]The isolation condition used for the efficiency measurements is a likelihood made up of the calorimeter energy and track momentum inside a cone around the muon. The details of this isolation criteria will be discussed in more detail in chapter 7.

[9]Minimum Ionizing Particle

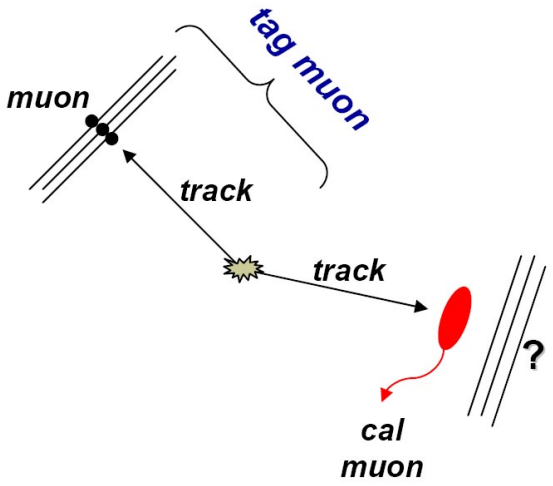

Figure 4.10: Schematic view of the tag and probe muon selection and making of the Z candidates for muon reconstruction efficiency measurement.

Real Z candidates can clearly be seen from the distinct peak around 90 GeV in the dilepton invariant mass spectrum as shown in Fig. 4.11. For making Z candidates, we only consider opposite sign pairs for the two tracks. As seen from the invariant mass plots, not all the candidates within a mass window are from Z 's. There is substantial background from continuum Drell-Yan spectrum as well as combinatoric background. To find the number of real Z candidates before and after the requirement of a reconstructed muon for the probe track, we fit the invariant mass distribution to a sum of a signal shape and a continuous background. For the signal shape, we use a convolution of a Breit-Wigner and Gaussian functions and for background, we use an exponential function.

From the fits, we find that the total number of actual Z candidates (integral of the signal) within an invariant mass window of [65, 115] GeV is 10142.9 for the tag muon and probe track combination. This number reduces to 9171.2 when the probe track is required to match a loose muon and the reduction factor is

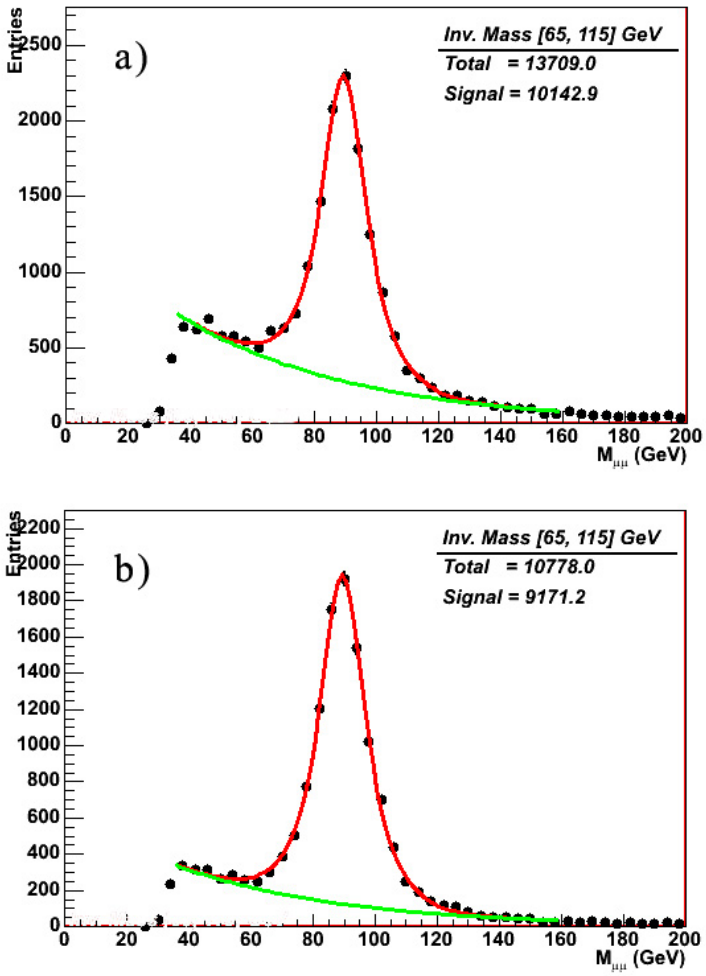

Figure 4.11: The invariant mass distributions. a) Tag muon and probe track and b) tag muon and probe track matched to a loose muon. The total number of candidate events within a mass window of [65, 115] GeV is shown on the upper right corner of the plots along with the integral of the signal function within the same window showing the number of actual Z candidates. The efficiency of the requirement of the probe track to be matched to a loose muon is the ratio of the Z (signal) candidates between the two selections.

equal to the efficiency of this requirement. We find the loose muon reconstruction efficiency to be 90.4±0.3 %. We note that this is not the pure figure for the local muon reconstruction efficiency but rather the combined effect of local track finding and central track matching efficiency.

The efficiency for the muon trigger condition can also be found from the Z candidates in a similar manner. Knowing the loose muon reconstruction efficiency we found above, we can increase the purity of the probe track by requiring a matched offline loose muon and ask whether or not this probe muon triggers a set of muon trigger conditions.

The trigger efficiency for each trigger condition can be obtained by dividing the number of dimuon candidates before and after the trigger requirement imposed on the probe muon. This way, L1 trigger efficiency is calculated with respect to the central track matched reconstructed loose muons, and L2 with respect to L1 and L3 with respect to the L2 trigger conditions. These trigger efficiencies are given as a function of probe track p_T, η and ϕ in Figs. 4.12, 4.13 and 4.14. Average efficiency for L1 condition is found to be 68.1%, for L2 it is 97.4% and for L3, it is 87.8%.

4.4 Electron Reconstruction

In the study this thesis describes, we performed our analysis using muons, but a similar analysis with electrons has also been performed in DØ . The results of the two are combined and more detail can be found in chapter 6. Therefore, in this section, we give a brief introduction of electron reconstruction at DØ .

Electrons are identified by detecting their energy depositions in the calorimeter [63] as well as showering signature in the preshower detectors and the track found in the central tracking system. The calorimeter showers from the electrons and

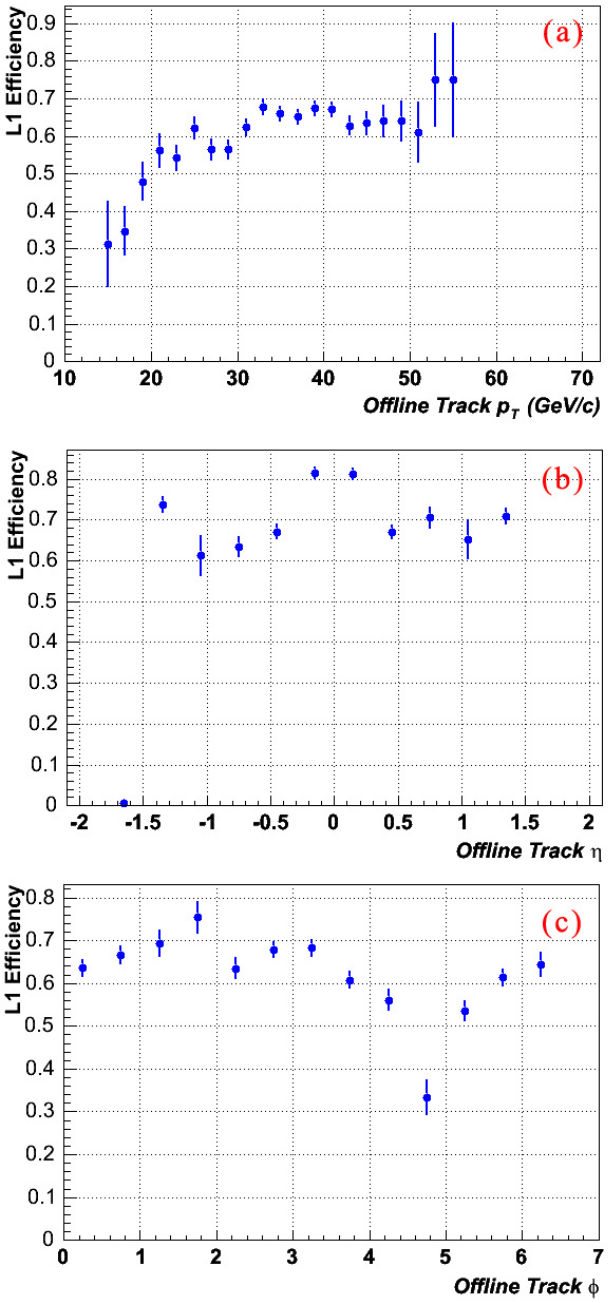

Figure 4.12: Level 1 muon trigger efficiency with respect to a central track which is also matched to a reconstructed loose muon. Trigger efficiency as a function of probe track a) p_T, b) η and c) ϕ are shown.

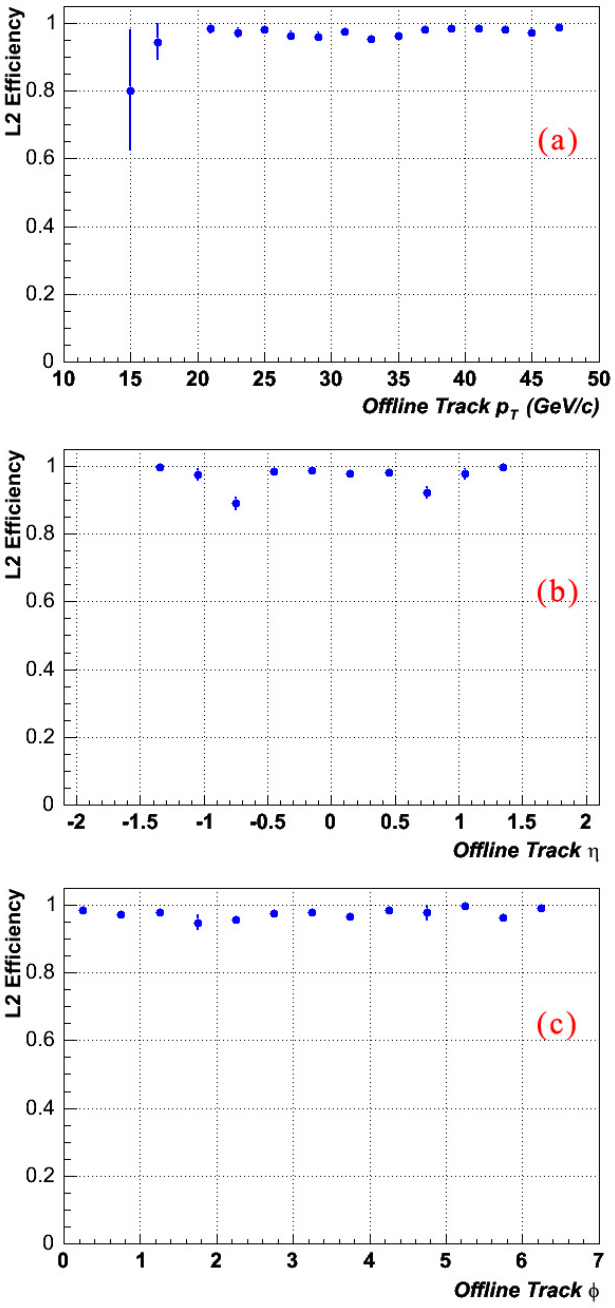

Figure 4.13: Level 2 trigger efficiency for medium muon with p_T larger than 3 GeV requirement with respect to the Level 1 trigger condition. Trigger efficiency as a function of probe track a) p_T, b) η and c) ϕ are shown.

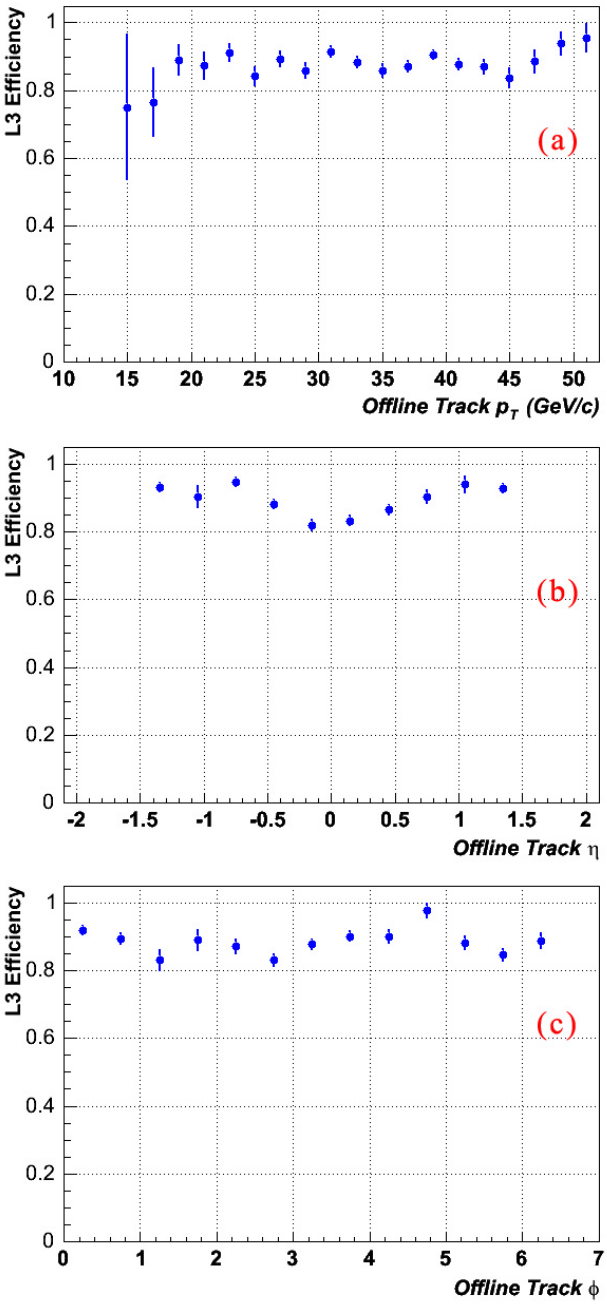

Figure 4.14: Level 3 trigger efficiency for a track above 10 GeV requirement with respect to the Level 2 trigger condition. Trigger efficiency as a function of probe track a) p_T, b) η and c) ϕ are shown.

photons are similar with energy deposited mainly in the electromagnetic (EM) layers of the calorimeter. The reconstruction of electrons [64, 65] and photons [66] use the same reconstruction algorithm with the distinction made by the presence or absence of a central track or a preshower signature. Electrons and photons are collectively called "EM" objects.

Electromagnetic clusters are reconstructed using two main approaches; a simple cone algorithm and the cell nearest-neighbor algorithm.

- **Simple Cone** — The simple cone algorithm makes clusters of calorimeter towers within a cone size of $R \equiv \sqrt{\Delta\eta^2 + \Delta\phi^2} = 0.4$. For electromagnetic object reconstruction, an electromagnetic tower consists of four EM layers and the first hadronic layer (FH1) of the calorimeter. The reconstruction algorithm starts with the highest E_T EM towers for the seed of the clusters. Adjacent EM towers above 0.5 GeV are added to the cluster if they are within a window of 0.3 $\times$ 0.3 in $\eta \times \phi$. In the next step all towers within a cone radius of 0.4 with respect to the energy weighted axis of the original cluster is added. Then the axis is recalculated and the last step is repeated until a stable cluster is reconstructed.

- **Cell Nearest Neighbor (CellNN)** — The CellNN algorithm performs electron reconstruction from calorimeter cells rather than towers as in the case of simple cone algorithm. In each calorimeter layer, the cell with highest energy is used as the seed for this algorithm. Local clustering (also called floor clustering) is performed within each calorimeter layer by adding the neighbor cells to the seed cell. Each floor cluster in EM3 (third electromagnetic layer) initiates a global cluster and layer by layer, floor clusters matching an angular requirement are added to the global cluster as shown in Fig. 4.15. If a floor cluster is shared between two global clusters, its energy is shared between the two clusters using a parametrization of the shower

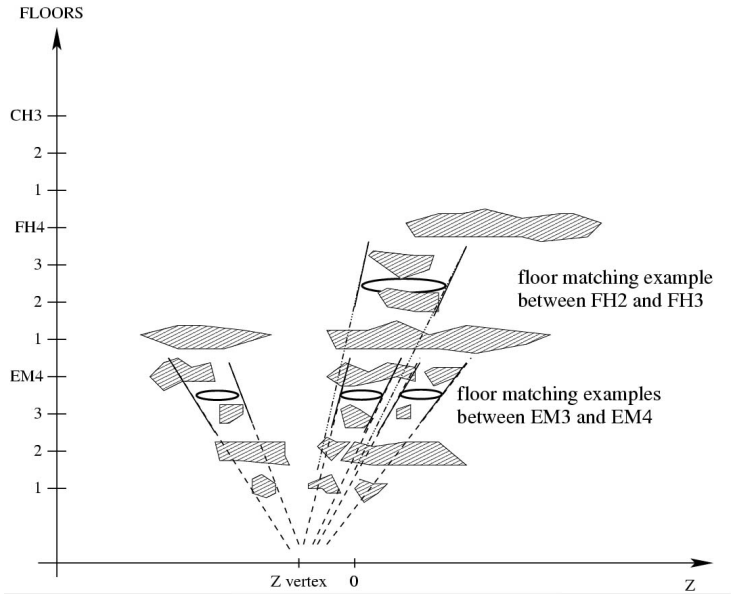

Figure 4.15: Schematic view of global cluster building from the floor (layer) clusters [65]. For electromagnetic object reconstruction, the seed floor cluster is selected from the EM3 layer of the calorimeter.

shape.

4.4.1 Electron Identification

The clustering algorithms described previously do not make a distinction between electrons and photons. This distinction is mainly done by looking for the presence of a track pointing to the calorimeter cluster. Since photons are neutral particles, their tracks are not reconstructed in the central tracking system. In order to find a track candidate for the EM cluster, a road of 0.05×0.05 in $\Delta\eta \times \Delta\phi$ is defined between the center of the calorimeter cluster and the hard-scatter vertex (primary vertex). A search for a track with transverse momentum larger than 1.5 GeV is performed within this road. If one or more tracks are found, the candidate is considered as an electron, otherwise it is accepted as a photon candidate.

A more detailed χ^2 track and cluster matching is then performed for electron candidates as a part of the electron identification procedure. There are more standard electron identification criteria used in DØ and these are summarized below.

- Electromagnetic Energy Fraction (EMF) — EMF is the fraction of the total energy of the cluster deposited in the EM layers of the calorimeter. An EM object candidate is required to have an EM fraction of larger than 90%.

- Isolation — In order to reduce the fake rate of EM objects found in the calorimeter mainly caused by the jets which deposit non-collimated energy in EM layers, an isolation criteria is defined. The isolation is defined as in Eq. 4.9 and provides optimum levels of EM object reconstruction.

$$f_{iso} = \frac{E_{TOTAL}(0.4) - E_{EM}(0.2)}{E_{EM}(0.2)} \tag{4.9}$$

  where $E_{TOTAL}(0.4)$ is the total energy contained in a cone of radius 0.4, and $E_{EM}(0.2)$ is the electromagnetic energy contained in a cone of radius 0.2 around the electron candidate. Electromagnetic candidates are generally required to have isolation values of less than 15% to be identified as electromagnetic objects (i.e. $f_{iso} < 0.15$).

- H-Matrix Technique — Another criteria used to distinguish electrons and photons from hadronic jets is the shape of the showering in the calorimeter. In order to obtain the best discrimination against jets, both longitudinal and transverse shower shapes as well as the correlations between the cell energies are used. This is done using a simple covariance matrix, M, of 8 variables to characterize the discrimination between electromagnetic and hadronic objects as shown in Eq. 4.10.

$$M_{ij} = \frac{1}{N}\sum_{n=1}^{N}(x_i^n - \langle\ x_i\ \rangle)(x_j^n - \langle\ x_j\ \rangle) \tag{4.10}$$

where n is the event index and i represents the index of the shape variable. The covariance matrix is derived from N Monte Carlo generated electrons using 8 shower shape variables. An H matrix is defined as the inverse of this covariance matrix as shown in Eq. 4.11. Using this matrix, one can find the χ^2 of a test object representing the likelihood of having similar shower shape as the electrons in the covariance matrix. A test object, $\vec{x_k}$ can be tested for being consistent with an electromagnetic object as in Eq. 4.12.

$$H \equiv M^{-1} \tag{4.11}$$

$$\chi^2 = \sum_{ij}(x_i^k - \langle\ x_i\ \rangle)\ H_{ij}\ (x_j^k - \langle\ x_j\ \rangle) \tag{4.12}$$

The eight variables fed as input to the H-matrix technique are listed below:

1. Fraction of shower energy in the 1^{st} EM layer of calorimeter.
2. Fraction of shower energy in the 2^{nd} EM layer of calorimeter.
3. Fraction of shower energy in the 3^{rd} EM layer of calorimeter.
4. Fraction of shower energy in the 4^{th} EM layer of calorimeter.
5. Size of the cluster in the third EM layer along the radial axis for the end calorimeters and z-axis for the central calorimeter.
6. Size of the cluster along $r - \phi$ axis in the third EM layer.
7. Total shower energy.
8. Primary vertex position.

The first four variables, shower energies taken from the corresponding EM layers of the calorimeter represent the longitudinal development of the shower. The next two variables describe the transverse development of the shower by providing a description of the cluster sizes in the third EM layer. The last two parameters are added to provide a parametrization of the total energy and the impact parameter dependence on the matrix.

A typical electron selection requires the H-matrix χ^2 to be lower than 20.

4.5 Jet Reconstruction

Reconstruction of jets is performed by clustering of calorimeter energy deposited by the particles within the jet[67]. The reconstruction algorithm is composed of the following steps [68]:

1. The 0.1×0.1 $\eta \times \phi$ calorimeter towers are reconstructed from the calorimeter cells. The towers are the basic building blocks for jet clustering algorithm used in DØ . Towers with transverse energy (E_T) less than 0.5 GeV are ignored to reduce the instrumental background.

2. The tower with highest transverse energy is used as the seed for preclustering. Preclusters are formed in a cone of $R = \sqrt{(\Delta\ \eta)^2 + (\Delta\ \phi)^2} = 0.3$ around the seed tower. Preclusters with total transverse energy less than 1 GeV are discarded. Towers belonging to an accepted precluster are removed from the list of towers and another preclustering is performed to find other jets in the event. The precluster axis is defined to be the E_T weighted centroid of the precluster towers as in Eq. 4.13 and Eq. 4.14 [69]

$$E_T \equiv \sum_i E_T^i = \sum_i E_i \times \sin\theta_i$$

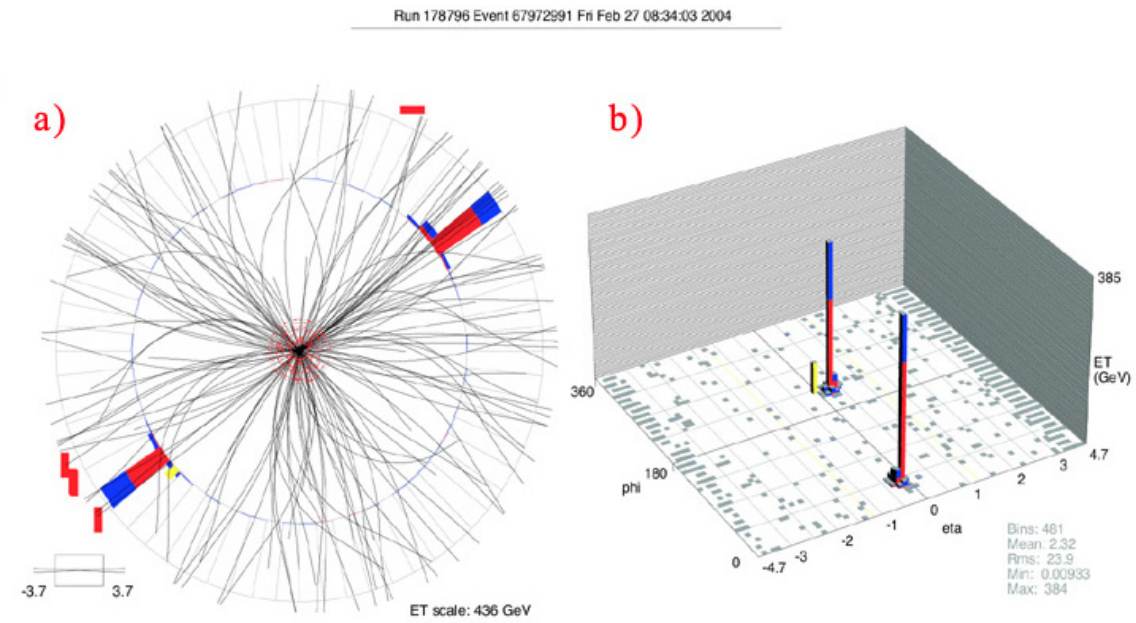

Figure 4.16: An event display of a recorded dijet event in DØ detector. Two views are shown. The picture on the left (a) shows an $r-\phi$ view of the event emphasizing the tracks found in the central tracker and the jets found in the calorimeter with blue and red colors (red color block histogram represents the energy in the electromagnetic and blue on top of that is the energy found in the hadronic layers of the calorimeter). The right picture (b) shows the same event in a lego plot showing the same jets in $\eta-\phi$ view. The yellow peak represents the missing energy calculated for the event.

$$\eta_{precluster} = \frac{\sum_i E_T^i \ \eta^i}{\sum_i E_T^i} \tag{4.13}$$

$$\phi_{precluster} = \frac{\sum_i E_T^i \ \phi^i}{\sum_i E_T^i} \tag{4.14}$$

3. Jet clustering starts with all preclusters with $E_T > 1.0$ GeV and adding all calorimeter cells within a fixed cone of radius $R = 0.5$ or 0.7. All jets in this document are reconstructed with a cone size of 0.5 unless mentioned otherwise. A new cluster (jet) axis and energy is calculated according to Eq. 4.13 and Eq. 4.14. This step is repeated until the jet axis becomes stable. Each jets found in this manner are required to have a total transverse energy larger than 8 GeV , and otherwise discarded.

4. If two stable reconstructed jets share calorimeter towers, they are merged if the shared energy between the two jets is larger than 50 % of the lower E_T jet. If the shared energy is lower than 50 %, then each shared tower is assigned to the jet which is closest.

5. Final reconstructed jets are required to have $E_T > 8$ GeV and discarded otherwise.

Before reconstructed jets are used as an input in a physics analysis, they are required to satisfy a set of quality cuts. These cuts are summarized below:

- **Electromagnetic Fraction (EMF)** — As we discussed for the electron reconstruction, EM fraction is a criteria used to distinguish between the hadronic jets and electromagnetic energy clusters. Electromagnetic objects tend to deposit most of their energy in the EM layers of the calorimeter whereas the shower shape of the jets are more uniform accross calorimeter layers. In order to make this distinction, reconstructed jets are required to have EM fractions between 5 and 95 %.

- **Coarse Hadronic Fraction (CHF)** — Coarse hadronic fraction is the fraction of transverse energy of the jet in the coarse hadronic layers of the calorimeter. The jets are required to have CHF values less than 40 %.

- **Hot Fraction** — The hot fraction is the ratio of transverse energy in the most energetic tower to that of the next leading tower in the jet. This fraction provides a control for the fake jets created when some towers systematically report high energy depositions due to problems in the corresponding read-out electronics etc. Reconstructed jets are required to have hot fractions of less than 10.

- **n90** — *n90* variable serves a purpose similar to that of hot fraction. It is the number of towers making up the 90 % of the jet energy. If more than 90% of the jet energy is contained in a single tower, the jet is almost certainly reconstructed due to a single hot calorimeter tower or cell. Therefore, reconstructed jets are required to have *n90* values larger than 1.

- **L1 Confirmation** — Due to the undesired noise levels in the precision readout of calorimeter cells, the trigger calorimeter readout is used to provide a confirmation of the readout measurements. The comparison of the precision readout and the trigger readout is not straightforward due to differences between the two, and adjustments have to be made. The trigger readout happens at the calorimeter tower level rather than calorimeter cells and not all the calorimeter layers are read out at Level-1. Therefore a new variable, called *L1conf* is created to even out the differences as shown in Eq. 4.15.

$$L1conf = \frac{\sum\limits_{Trigger} E_T^i}{E_T^{jet} \times (1 - CHF)} \tag{4.15}$$

Jets are required to have $L1conf > 0.4$ in the central and end calorimeter

regions (CC and EC) and $L1conf > 0.2$ in the inter-cryostat region (ICR).

4.5.1 Jet Reconstruction Efficiencies

The jet reconstruction efficiency (combined with the efficiency of selection requirements) in Monte Carlo is shown in Fig. 4.17 alone with the reconstruction efficiency scale factor between MC and real data. The MC efficiency is obtained from dijet production in Z decays whereas data/MC scale factor is obtained using photon plus jet events.

4.5.2 Jet Energy Scale

There are known systematic effects contributing to a discrepancy between the measured jet energies and the expected particle level jet energy in DØ . Reconstructed jet energies are corrected for these factors and this correction procedure is called the Jet Energy Scale (JES) [70]. Major systematic effects known to effect the measured jet energies can be listed as the calorimeter offset energy (E_{offset}), the calorimeter jet response (R_{jet}) and out-of-cone showering for cone jets (F_S, showering correction factor). All these factors contribute in a different way and parametrized as a function of jet energy and location in the detector. The relation between the measured energy of the reconstructed jet ($E_{jet}^{calorimeter}$) and the particle level energy ($E_{jet}^{particle}$) can be represented as in Eq. 4.16.

$$E_{jet}^{particle} = \frac{E_{jet}^{calorimeter} - E_{offset}}{R_{jet}\ F_S} \tag{4.16}$$

- **Offset Energy** — The offset energy term is used to describe the energy in the calorimeter from sources not related to the physics processes responsible for creating the jet. Some of the sources for this offset energy are the inelastic collisions in the bunch crossing other than the hard-scatter colli-

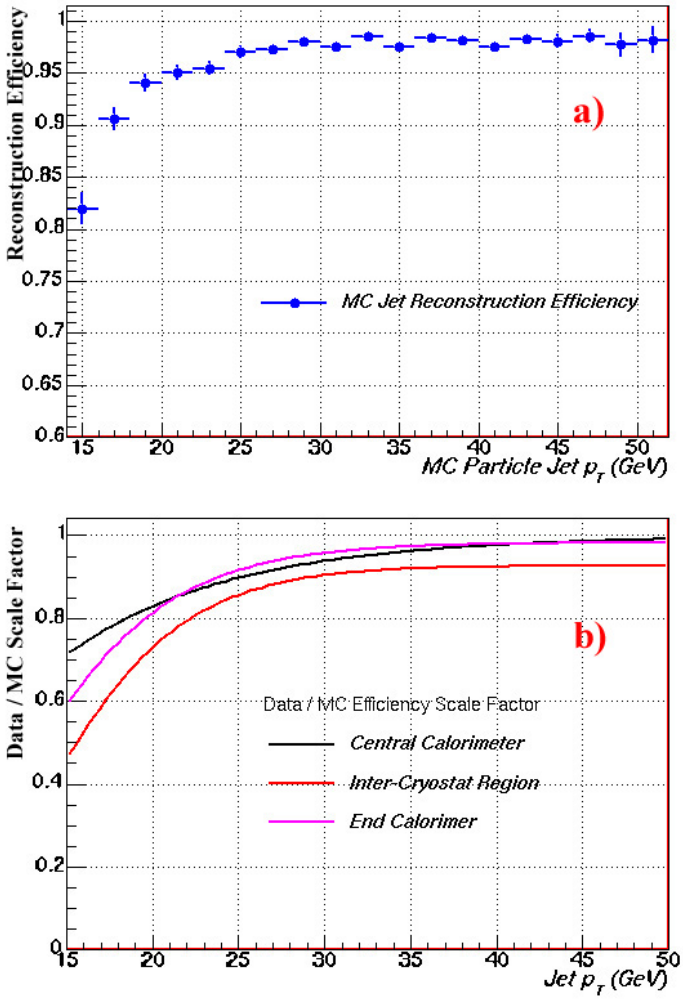

Figure 4.17: Jet reconstruction efficiency in Monte Carlo ($Z \rightarrow jj$) is shown as a function of jet transverse momentum in the upper figure (a). The efficiency is measured with respect to the particle jets formed using the individual particle information available in MC. Bottom figure (b) shows the efficiency difference for jets in data versus MC represented with a parametrized scale factor ($SF \equiv \epsilon_{DATA}/\epsilon_{MC}$) given for three regions of the calorimeter; central region ($|\eta| \leq 0.8$), the two inter-cryostat ($0.8 < |\eta| \leq 1.5$) and end regions ($|\eta| > 1.5$).

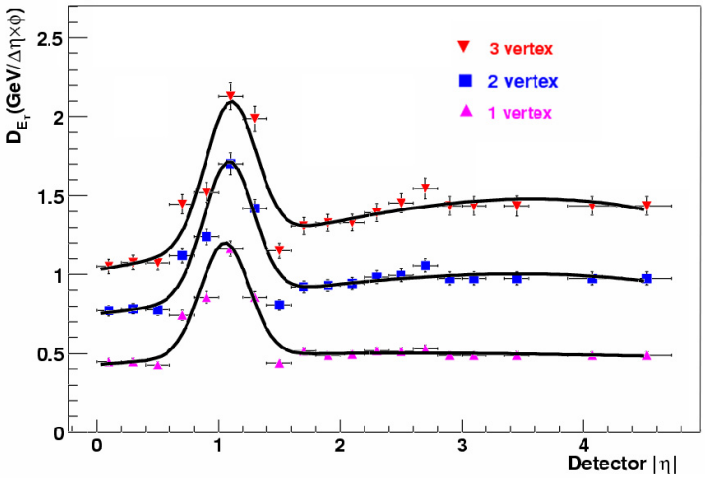

Figure 4.18: Offset energy parametrized as a function of calorimeter pseudo-rapidity [71]. The amount of offset energy present in the calorimeter is also strongly correlated with the number of interaction vertices found in the event which is then correlated with the instantaneous luminosity.

sion (minimum bias interactions or underlying event), radioactive noise due to the decaying of the uranium absorber plates of the calorimeter and the pile-up energy which is the left over signals present in the calorimeter from previous collisions occuring in the detector. In order to arrive at the corrected jet energy, this default energy present in the calorimeter must be calculated over calorimeter pseudo-rapidity regions and subtracted from the reconstructed jet energies.

Measured offset energy as a function of calorimeter pseudo-rapidity is shown in Fig. 4.18, as expected the offset correction is also highly correlated with the number of interaction vertices found in the event which is then correlated with the instantaneous luminosity for the collisions.

- **Jet Response** — Jet response is the major factor contributing to the mismeasurement of the jet energy. It is basically defined as the ratio of the

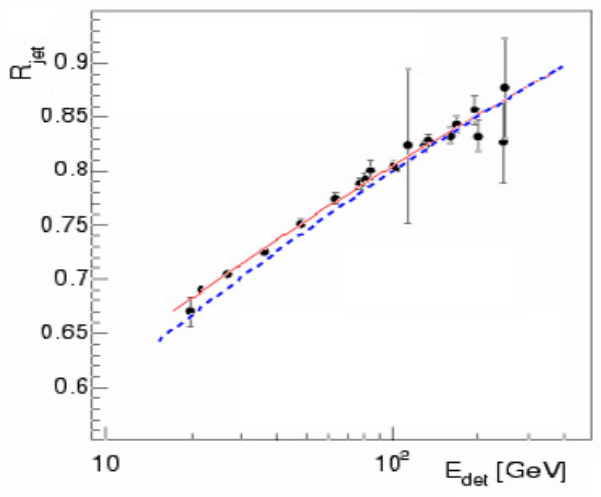

Figure 4.19: Jet response parametrized as a function of jet energy [71]. The jet energy response of the calorimeter is better for more energetic jets.

measured energy to the true energy deposited in the calorimeter. The response is generally less than 100 % due to the uninstrumented regions and dead material in the calorimeter. The jet response is measured by requiring energy balance in the transverse plane for photon+jet events where photon energy is measured to a higher accuracy than that of jets. The energy scale of the photons is well known due to the EM energy calibrations obtained from $Z \rightarrow e^+e^-$ events which are in turn calibrated using the precise tracking system measurements. The jet response is parametrized as a function of jet energy as shown in Fig. 4.19 as well as detector pseudo-rapidity of the jet.

- **Showering Correction** — Unlike the previous two corrections, the showering correction is less related to instrumental effects but is a consequence of the jet formation and hadronization process. Therefore, this correction is performed after the two previous corrections are applied for the jet energy

scale. The showering factor basically corrects for the typical energy radiated outside the jet cone and is not accounted in the measured jet energy. The correction amount is estimated by looking at the total amount of energy in concentric cones around the jet axis with radius varying from 0.1 to 2.0. This is called the *shower profile* is used to find the energy correlated with the jet, but left outside the jet reconstruction cone size. This correction is again parametrized as a function of jet energy.

The effect of all the jet energy scale corrections are shown in Fig. 4.20 as a function of jet energy and pseudo-rapidity. The total and statistical errors associated with the correction factor are also given as a function of jet energy and pseudo-rapidity in Fig. 4.21. Major systematic sources contributing to the error on the correction can be listed as the variation in the instantaneous luminosity (and hence the number of interactions per event), errors from the fits used to parametrize the correction, primary vertex selection criteria and the differences observed when dijet data is used instead of photon+jet data when estimating the corrections.

4.6 b-tagging Methods

Jets are experimental signatures for quarks and gluons but one missing item in the process of finding the jets is the classification with respect to the nature of the original parton creating the jet. There have been several studies to distinguish between the gluon and quark jets [72] - [74], but another important discrimination is necessary to identify the flavor of the quark jets to find whether or not it is generated by a light quark (up, down, strange) or a charm and a b quark. The latter process of classifying jets as coming from a light quark or a b quark is called b-tagging.

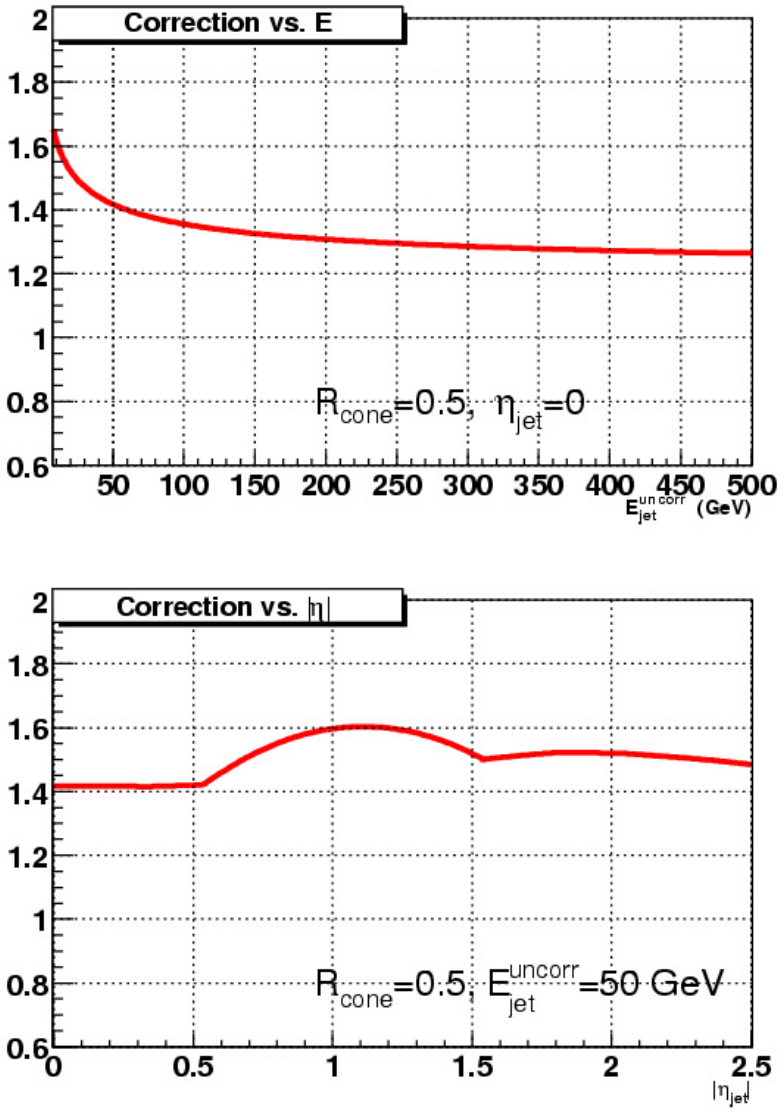

Figure 4.20: Jet energy scale correction parametrized as a function of jet energy (upper) and pseudo-rapidity (lower).

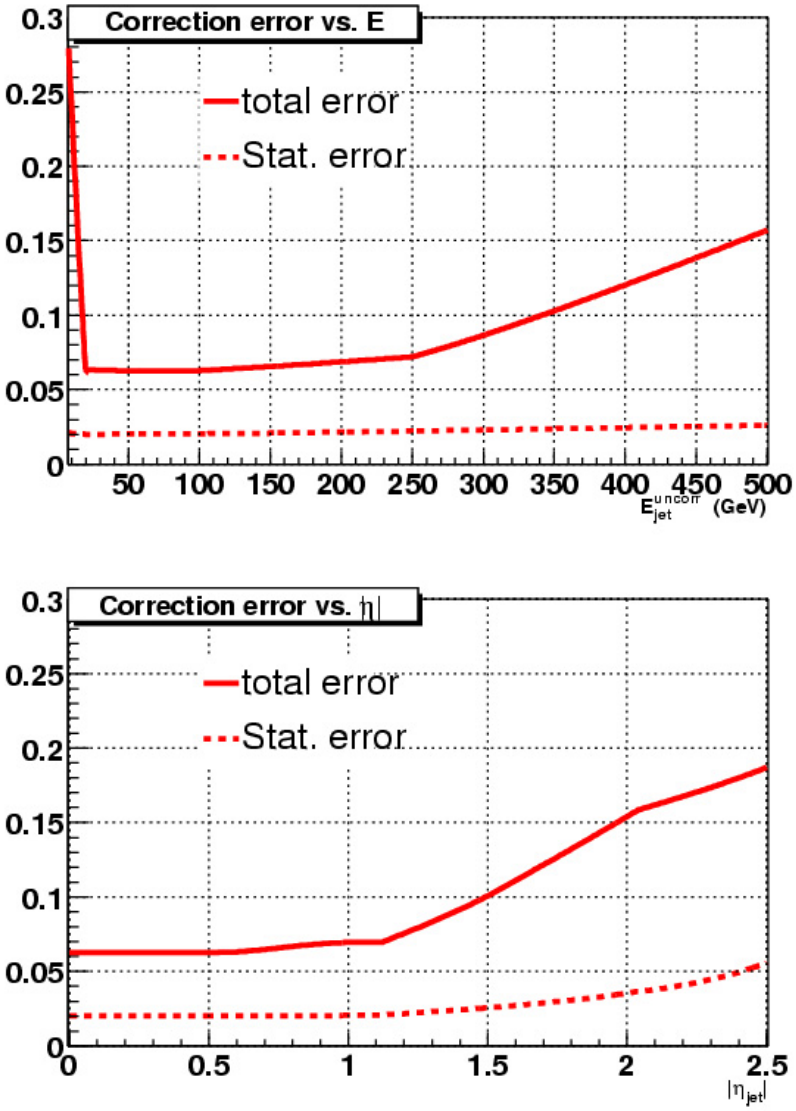

Figure 4.21: Jet energy scale correction error parametrized as a function of jet energy (upper) and pseudo-rapidity (lower).

The information from the DØ calorimeter alone is not sufficient to make such a distinction. One of the most common ways of doing b-tagging relies on the fact that B hadrons carrying b quarks have long lifetimes. A B hadron decay lifetime is on the order of a few picoseconds and the decay vertex can be a few millimeters away from the hard-scatter vertex making it possible to distinguish.

The particles coming from the decay of the heavy quark tend to have high-p_T and the charged ones can be detected with the central tracker. Due to the considerably displaced parent vertex, these tracks generally have large impact parameter with respect to the primary vertex. This knowledge is exploited in two ways in the identification of b quarks. The tracks are used to perform a secondary vertex fit separated from the primary vertex is reconstructed. The presence of the secondary vertex within a jet identifies that the jet has a high probability to be a heavy quark produced jet. Another way to identify the heavy jets is to look at the impact parameters of the tracks within a jet rather than reconstructing the vertex. Large impact parameter of the tracks hint at the existence of heavy quark signature and this information is transformed into a likelihood to define the probability to be a b quark produced jet. These two methods will be explained in more detail in the following two sections.

Before we proceed, we need to introduce an important definition which will be used widely in this analysis. In order to reduce the fake rate of jet reconstruction and have a better measure of the effectiveness of the b-tagging algorithms, reconstructed jets are required to meet further selection criteria called jet *taggability*. Before b-tagging is applied to calorimeter jets, all jets are first required to be *taggable*. For testing the calorimeter jets against taggability, a new type of jets is reconstructed from tracks (called *track jets*) [75]. These track jets are reconstructed from tracks with at least 2 SMT hits, $p_T > 0.5$ GeV , $|DCA_r| < 0.15$ cm and $|DCA_z| < 0.40$ cm, using a three dimensional cone clustering algorithm

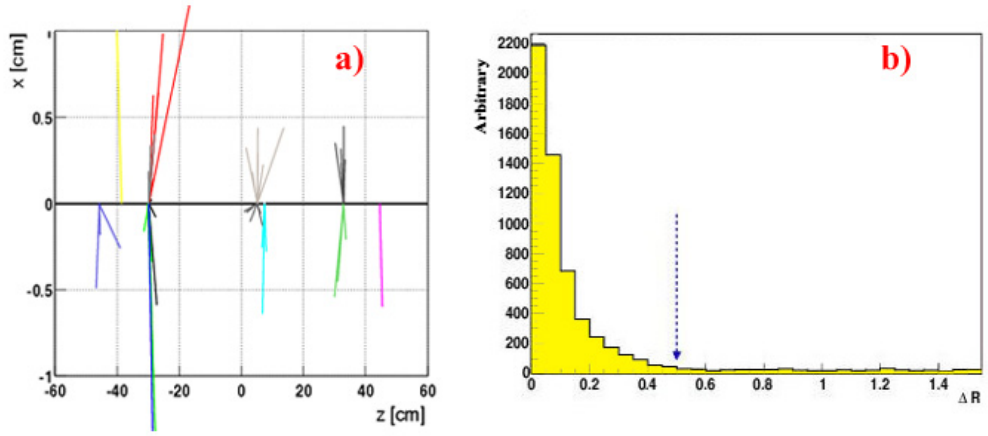

Figure 4.22: 3 dimensional track-jet clustering is shown in the x-z event display on the left (a). The ΔR distance between a calorimeter jet and the reconstructed track jet is shown on the right (b) with the cut value (0.5) emphasized.

of radius 0.5. In order to be taggable, we require that there must be a track-jet matching to a calorimeter jet within its cone size, or geometrically speaking, the two axes of calorimeter jet and the track-jet should not be separated larger than 0.5 in δR. This taggability condition can more easily be seen in Fig. 4.22.

Average taggability efficiency of the reconstructed calorimeter jets with $p_T >$ 20 GeV and $|\eta| < 2.5$ is measured to be about 79% in data. Taggability efficiency varies slightly (about $\sim 2\%$) with the underlying quark nature of the jet and this difference will be investigated later in this text.

4.6.1 Secondary Vertex b-tagging

The secondary vertex (SV) b-tagging algorithm identifies the b-jets by reconstructing the displaced vertex where B hadron decays. The reconstructed displaced vertex is then required to match to the calorimeter jets [76]. The algorithm works in three steps; a long-lived light particle removal procedure called V_0 removal, re-

construction of the track jets and secondary vertices and lastly the association of secondary vertices with the calorimeter jets.

1. V_0 removal procedure is performed to reduce the number of jets that are b-tagged because they contain long-lived particles other than B hadrons. This procedure explicitly removes the two track vertices which are due to particles like K_s^0, Λ or a photon conversion into an e^+e^- pair. The V_0 removal algorithm finds these vertices by comparing the mass of the two-track vertex to the known masses of these long-lived particles. If consistent, the tracks are removed from the list of available tracks for secondary vertex reconstruction.

2. As we briefly discussed for the definition of the taggability condition, clustering of the tracks into track jets is also used as seed for the secondary vertex reconstruction. The track-based jet finding starts by clustering of the tracks in the z-direction. Tracks are formed in pre-clusters if $\Delta z < 2$ cm for the tracks within the pre-cluster, where z is measured with respect to the distance of closest approach. In each pre-cluster, the tracks are required to meet the following conditions;

   - $p_T > 0.5$ GeV
   - $N_{SMT} \geq 2$
   - $DCA_r < 0.15$ cm
   - $DCA_z < 0.40$ cm

   For every pre-cluster, the tracks passing these cuts are clustered using a three dimensonal cone algorithm with radius 0.5, starting from a seed track with $p_T > 1.0$ GeV . The seed track momentum cut is required to reduce the number of track jets from the low momentum underlying event.

After the track-jets are formed, tracks are passed through a second set of selection to identify the displaced tracks and prepare them for the vertex fitting. The tracks are filtered by requiring an impact parameter significance larger than 3 ($DCA_r/\sigma_{DCA_r} > 3$) and CFT hit requirement of at least 7 ($N_{CFT} \geq 7$).

For every track jet with at least two selected tracks, the secondary vertex fitting procedure is performed. Two track seed vertices are formed from the selected tracks in each track-jet if the vertex χ^2 is less than 100. Additional tracks existing in the track-jet are attached to the seed if the combined vertex χ^2 is less than 15.

Resulting secondary vertices must then pass the following selection criteria;

- The 2D decay length, $|\vec{L}_r|$ (projection of the 3D decay length in the transverse plane) of the secondary vertex must be smaller than 2.6 cm. The decay length vector is defined to be the vector extended from the reconstructed primary vertex to the secondary vertex point.
- The collinearity of the secondary vertex must be larger than 0.9. Collinearity is defined to be the cosine of the angle between the decay axis and the direction of the vectorial sum of the momentum of tracks associated to the secondary vertex. The momentum of the secondary vertex is calculated as the vector sum of the momentums of the attached tracks. The collinearity criteria helps select the secondary vertices consistent with coming from the primary vertex since the B hadron creating the secondary vertex would have a momentum along the direction of its decay length vector, yielding a small angle (large cosine value) between the two vectors.
- The decay length significance, $|\vec{L}_{xy}|/\sigma_{|\vec{L}_{xy}|}$ of the vertices should be at

least 5.

Secondary vertices selected with above cuts are considered to be the *LOOSE* vertices and tighter selections are also applied to provide a flexible signal efficiency versus background rate control. The list of other types of secondary vertices are given in Table 4.1 and compared to the default LOOSE vertices.

	LOOSE	**MEDIUM**	**TIGHT**
Track IP Significance Cut	3.0	3.5	3.5
$\|\vec{L}_r\|$ (cm) Cut	2.6	2.6	2.6
Vertex Collinearity Cut	0.9	0.9	0.9
Decay Length Significance Cut	5	6	7

Table 4.1: Different selection criteria used for the reconstruction of three types of secondary vertices.

3. Finally, for b-tagging the jets, reconstructed secondary vertices are matched to the taggable calorimeter jets. The matching criterion is a simple geometrical requirement such that the ΔR distance between the calorimeter jet axis and the momentum vector of the vertex should be less than 0.5. Using this requirement, calorimeter jets might have a positive or a negative match. The sign of the matching is taken from the following observation; if the angle between the secondary vertex decay length vector and its momentum is smaller (larger) than 90 degrees, the match is defined to be positive (negative). Only the positive tags are considered to be the real b-tagged jets whereas negative tags are mostly due to the finite resolution of the primary vertex measurement.

The performance of the secondary vertex b-tagging as measured in data is shown for the three types of vertices in Fig. 4.23 as a function of fake (or *mistag*)

rate which describes the b-tagging rate for light quark jets [77]. The efficiency and mistag rate are also parametrized as a function of jet transverse momentum and psuedo-rapidity.

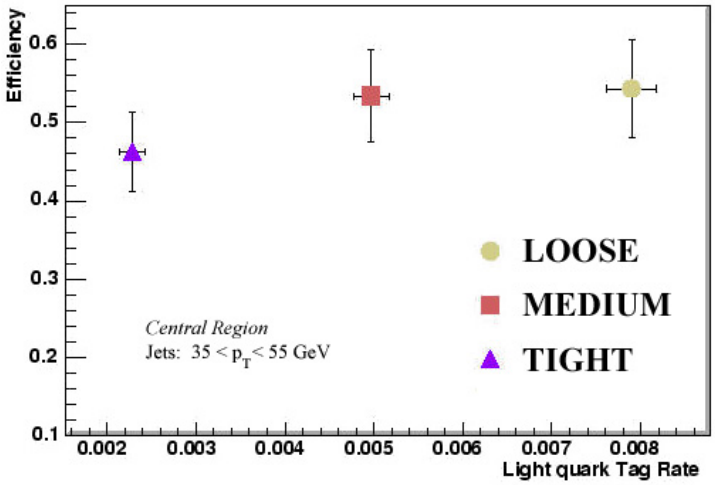

Figure 4.23: Performance of the secondary vertex b-tagging measured in data for three types of vertices as a function of fake rate which describes the b-tagging rate in light quark jets. The efficiency is shown for jets within the central region of the calorimeter and transverse momentum between 35 and 55 GeV .

4.6.2 Impact Parameter b-tagging

For the impact parameter (IP) b-tagging method, there is no need to fully reconstruct the displaced vertex of the B hadron. However, exploiting the same physical observation that the tracks from the decay of the heavy hadrons appear displaced from the primary vertex, the impact parameter method is used to identify jets produced by b quarks.

As we discussed for the sign of the secondary vertices, the impact parameter of a track is also considered to be a signed quantity with respect to a given jet. The assignment of the sign of a track impact parameter is more clearly shown in

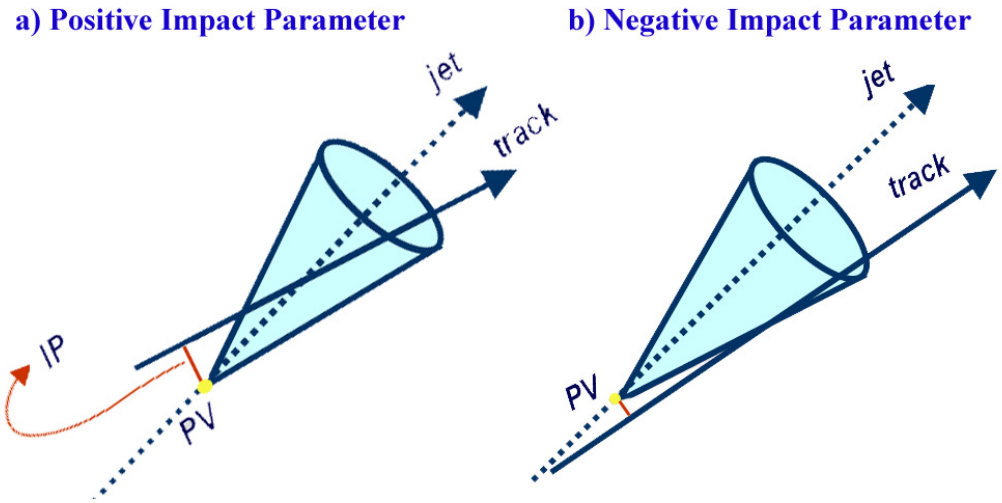

Figure 4.24: Schematic description of the track impact parameter sign. The track gets a positive impact parameter with respect to the jet if the track crosses the jet axis in front of the PV (towards the jet) and gets a negative impact parameter if it crosses behind the PV.

Fig. 4.24. Positive and large IP tracks are thought to be the tracks coming from the decays of the heavy hadrons however negative IP tracks are actually coming from the primary vertex but appear displaced due to the finite vertex and track resolutions.

In the IP b-tagging method, the negative IP tracks are used to form a likelihood to describe the tracks belonging to the primary vertex and hence not coming from a heavy hadron decay [78]. The likelihood probability ($\mathcal{P}(S_{IP})$) is in fact generated from the negative side of the impact parameter significance distribution (S_{IP}, used as the probability density distribution) shown in Fig. 4.25. The probability is mathematically defined as in Eq. 4.17.

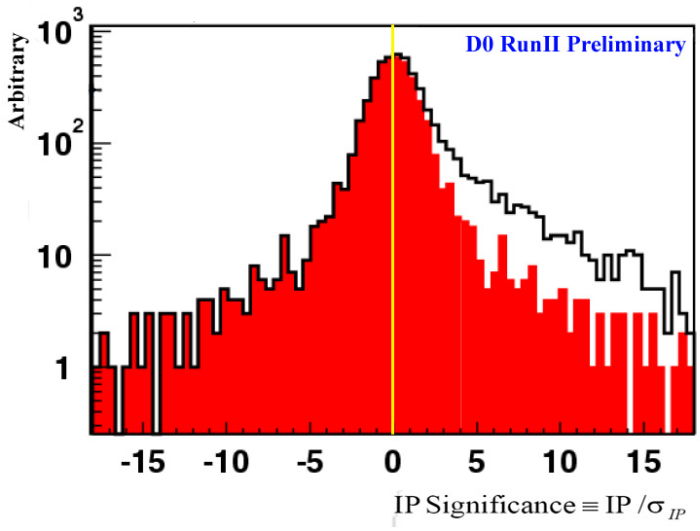

Figure 4.25: Signed IP significance distribution (black histogram). Red fill shows the mirror image of the negative side of the distribution on the positive side (with respect to yellow zero-line). The excess amount of tracks on the positive side is a signature of displaced tracks coming from the decays of heavy particles.

$$\mathcal{P}_{trk}(S_{IP}) = \frac{\int_{-30}^{-|S_{IP}|} f(S_{IP})\, dS_{IP}}{\int_{-30}^{0} f(S_{IP})\, dS_{IP}} \tag{4.17}$$

The probability given in Eq. 4.17 describes the probability of a track to come from a primary vertex. The probabilities of tracks associated with a jet (within a jet cone) are converted to a single jet probability using the relation in Eq. 4.18. The impact parameter probability distributions for MC light jets and b-jets are shown in Fig. 4.26. By construction, the light jets homogenously occupy all probability values between 0 and 1 (giving a flat distribution) while b-jets are distinguished by small probability values.

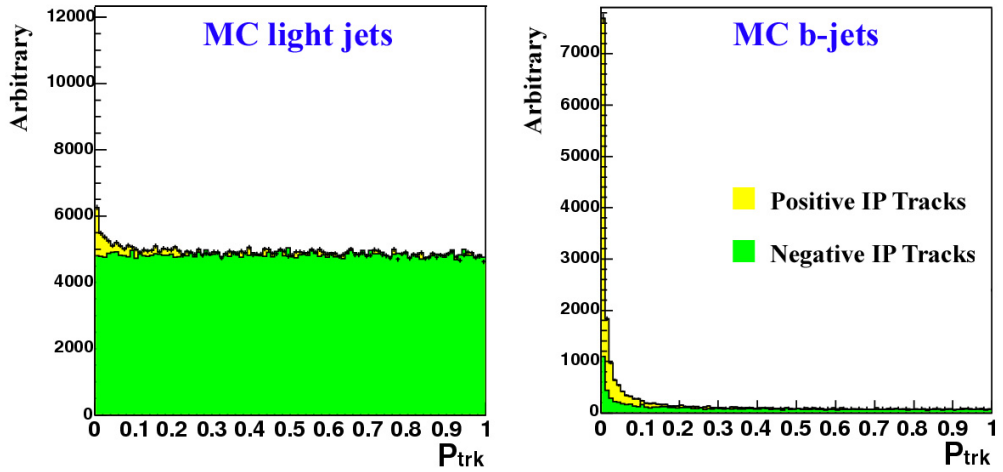

Figure 4.26: IP parameter probability of jets in MC reconstructed using only positive (yellow fill) and negative (green fill) impact parameter tracks. The small excess near zero in the light jet distribution is due to V_0 particles not removed effectively.

$$\mathcal{P}_{jet} = \prod \cdot \sum_{i=0}^{N_{\text{tracks}}-1} \frac{(-\log \prod)^i}{i!} \tag{4.18}$$

$$\prod \equiv \prod_{j=1}^{N_{\text{tracks}}} \mathcal{P}^j_{trk}\,(S_{IP})$$

With the IP b-tagging method, the taggable jets are assigned the IP parameter probability which describes the probability of being associated with the primary vertex. Jets are identified as b-jets simply by requiring this probability to be smaller than a preset value. As in SV b-tagging method, there are three types of IP b-tagging operating points commonly used in DØ that correspond to different signal efficiency and mistag rate levels. These points are $\mathcal{P}_{jet}$ <0.014, 0.007 and 0.004, which are called LOOSE, MEDIUM and TIGHT b-tagging respectively.

The performance of the impact parameter b-tagging as measured in data is shown in Fig. 4.23 as a function of the *mistag* rate [79]. The efficiency and mistag rate are also parametrized as a function of jet transverse momentum and psuedo-

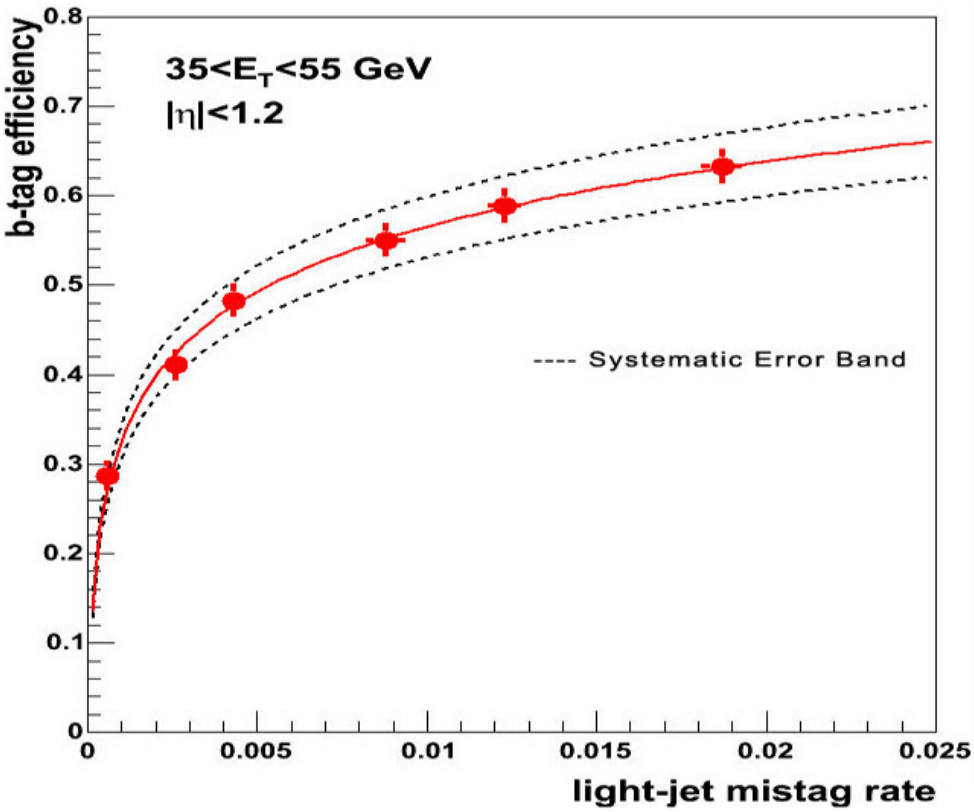

Figure 4.27: Performance of the impact parameter b-tagging measured in data as a function of fake rate which describes the b-tagging rate in light quark jets. The efficiency is shown for jets within the central region of the calorimeter and transverse momentum between 35 and 55 GeV .

rapidity.

Chapter 5

Production of $Z + b$-jet in Dimuon Channel

5.1 Introduction

The production of b-quark(s) associated with the W/Z boson constitutes the essential signature for several processes currently searched for and studied at DØ such as Higgs boson production. Understanding of all the processes giving rise to these signatures has paramount importance for the completeness of the Higgs searches, which are currently limited only due to the low production probabilities. Observation of events with b-jets and W/Z bosons will be of primary importance for the Higgs boson discovery.

Furthermore, the current theoretical understanding of the processes which yield b-jets in association with EW bosons are not very precise due to significant contributions from higher order interactions and the uncertainties regarding the b-quark density in protons. So the observation of these events provides a critical test of our current knowledge regarding these processes.

We study b-jet production associated with Z boson in this thesis and in particular, measure the ratio of inclusive cross sections for the $Z + b$-jet and Z+jet processes, where the Z boson decays to two muons i.e. $\sigma(Z(\mu\mu)+b\text{-jet}) / \sigma(Z(\mu\mu)+$ jet). A similar analysis was also performed in the Z decay di-electron channel and the combination of the two results will be discussed in the next chapter.

5.2 Event Selection

The dataset we used for this analysis was collected with the DØ detector between August 2002 and September 2003. Rather than measuring the cross-section for a specific process, we measure the ratio of cross-sections, therefore the exact value of the integrated luminosity for our data sample is not necessary as an input to this study. For this reason, we relax the requirement on the trigger selection for the data sample and we require any L3 trigger with associated muon triggers for the selected events. In order to suppress any bias from triggers associated with jets, we ignore those triggers that require both jets and muons. The total recorded luminosity for the period of runs is reported to be about 180 pb^{-1} .

The data set consists of events which are preselected (or so-called *skimmed*) with a requirement of two high p_T muons, reconstructed with version p14 of DØRECO and reformatted with top_analyze package[1], version Nefertiti [80]. The two high p_T muon preselection condition is imposed by requiring at least two muons of "loose" quality, both matched to central tracks and each with central track transverse momentum larger than 15.0 GeV .

To remove data declared unusable by the data-quality experts due to problems with the detector and/or trigger, we used top_dq package, version v00-04-00

[1]top_analyze is a basic software utility used to change the data output format from binary to more user friendly and object oriented ntuple format. This utility is also used to perform post-reconstruction level corrections on data.

Sample	MC Generator	Sam Req. ID	Events
$Z(\mu\bar{\mu}) + b\bar{b}$	ALPGEN +PYTHIA	11409-11410	100000
$Z(\mu\bar{\mu}) + jj$	ALPGEN +PYTHIA	10721-10724	200000
$Z(\mu\bar{\mu}) + j$	ALPGEN +PYTHIA	11304-11305	150000
$Z(\mu\bar{\mu}) + b$	PYTHIA	11642	15000
$Z \rightarrow b\bar{b}$	PYTHIA	8847	10000
$Z \rightarrow c\bar{c}$	PYTHIA	8935	10000
$Z \rightarrow q\bar{q}$ $(q = uds)$	PYTHIA	8846	10000

Table 5.1: Information on the MC samples used in this analysis. Sam request id number is the index of the MC files in the Fermilab data storage framework.

[81]. We create a list of runs (*good run list*) corresponding to the usable data for physics analysis purposes and feed this list to the top_dq package for the automatic selection of runs consistent with the list. The good run list for this analysis was created with the following conditions on detectors: no "bad SMT", no "bad CFT", no "bad CAL" and "reasonable" MUON detector quality. A "bad" detector component is usually due to data acquisition problems, specific hardware problems or expert manipulated readout conditions related to this detector.

The Monte Carlo (MC) samples used in this analysis are shown in Table 5.1. These samples are generated with ALPGEN v1.3 [82] [83] and PYTHIA v6.2 [84] [10] leading order MC generators.

5.2.1 Muon Selection

The candidate $Z \rightarrow \mu\mu$ events are selected using dimuons satisfying the following muon selection criteria:

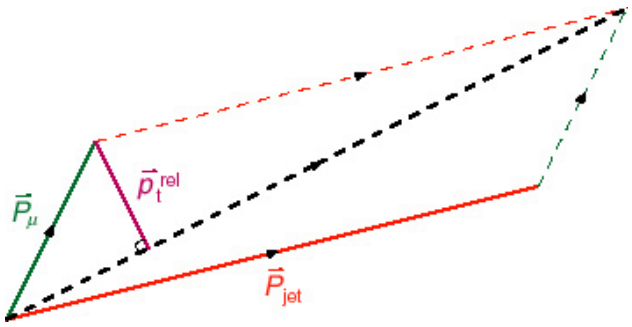

Figure 5.1: Schematic representation for the definition of the p_T^{rel} variable used for muon isolation.

- Local muons in the muon detector must be matched to a central track with;
  - $p_T^{central} > 15.0$ GeV
  - $|\eta| < 2.0$
  - Track transverse DCA < 0.25cm
- At least LOOSE quality
- Must be isolated with respect to the reconstructed calorimeter jets. The muon isolation is quantitatively described by the p_T^{rel} variable shown in Eq. 5.1 and defined to be the transverse component of the muon momentum with respect to the combined muon and the nearest calorimeter jet axis.

$$p_T^{rel} = \frac{|\vec{p}_\mu \times (\vec{p}_\mu + \vec{p}_{jet})|}{|(\vec{p}_\mu + \vec{p}_{jet})|} \tag{5.1}$$

  A schematic representation of the p_T^{rel} variable is given in Fig. 5.1 and in this analysis, muons are required to have p_T^{rel} larger than 10 GeV .

The isolation requirement is applied in order to reduce background due to the semi-leptonic decays of heavy quarks which provide muon and the jet signature

for the events we are interested in. These muons appear to be close to the axis of the jet associated with heavy quark and they tend to have lower momenta than the muons from Z bosons. Both effects are incorporated into our signal muon selection by the choice of the isolation criteria. As seen in Fig. 5.1, requiring large p_T^{rel} muons discriminates against the low momentum muons as well as the ones close to the jets.

In Fig. 5.2, we show the p_T^{rel} distribution of muons. The motivation behind the 10 GeV cut for p_T^{rel} is clearly seen in this plot. The peak near zero is due to the background muons and the flat distribution at high p_T^{rel} corresponds to the signal muons expected to come from Z bosons.

For selecting Z candidates, we require two preselected muons with the following criteria;

- Opposite electric charge i.e. $Q_{\mu_1} \neq Q_{\mu_2}$
- Opening angle in transverse plane: $\Delta\phi > 0.4$
- Invariant mass window: 65 GeV $< M_{\mu_1\mu_2} <$ 115 GeV

Using the Z candidates, we can also measure the efficiency of the muon isolation requirement. We create two samples of Z events for this purpose, one with exactly two isolated muons (N2) and another with one and only one isolated muon (N1). The number of real Z candidates in these samples are related to the isolation efficiency, ϵ, in equations 5.2, 5.3 and 5.4.

$$N_2 = \epsilon^2 \, N_Z \tag{5.2}$$

$$N_1 = 2 \, \epsilon \, (1 - \epsilon) \, N_Z \tag{5.3}$$

with solution

$$\epsilon = \frac{2 \, N_2}{2 \, N_2 + N_1} \tag{5.4}$$

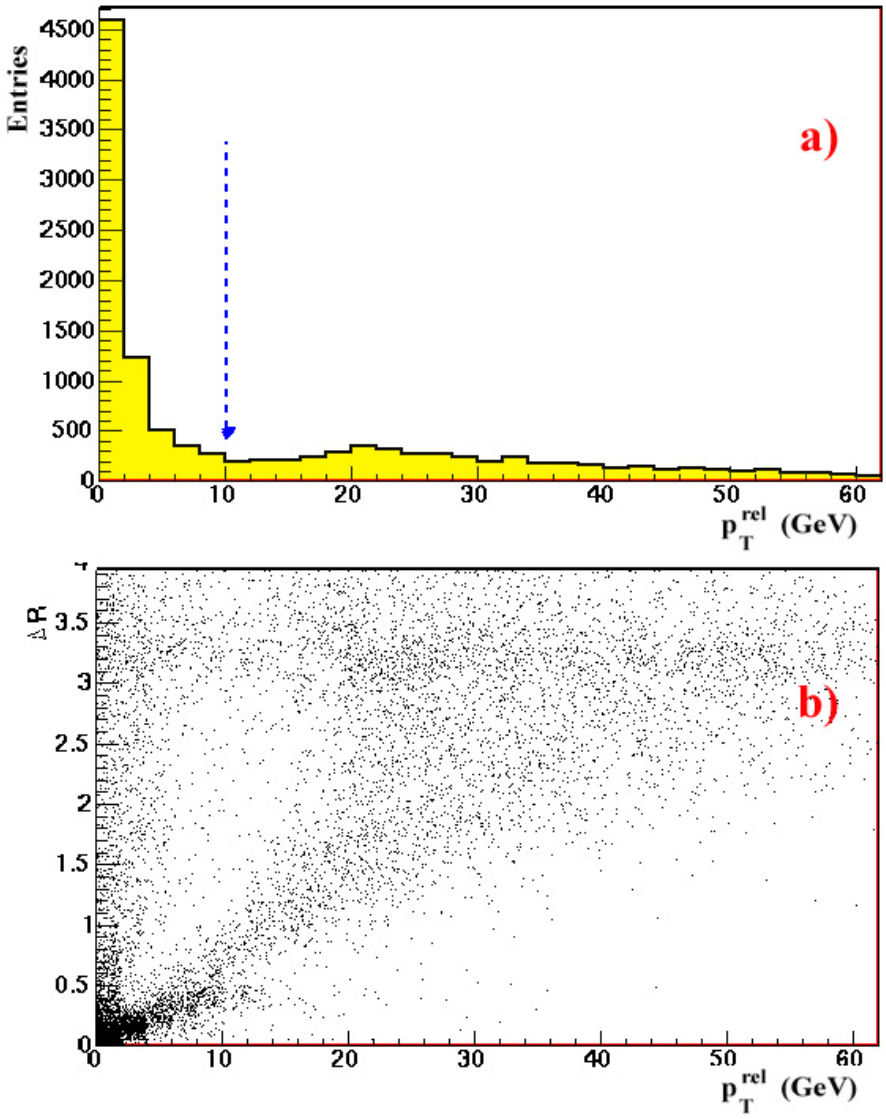

Figure 5.2: The p_T^{rel} distribution for muons in the data is shown in the upper plot (a) with the cut value is shown by the vertical arrow. The lower p_T^{rel} peak is expected to be due to the low momentum muons contained within or nearby the jet cone. The relation of the muon p_T^{rel} and the $\Delta\ R$ distance between the muon and the closest jet axis is also shown in the lower plot (b).

In order to find the number of Z candidates in these samples with different numbers of isolated muons, we employ a method we used in the previous chapter. We fit the invariant mass distributions of the dimuon candidates and extract the number of events consistent within the Z peak and the underlying background events. We use fits which are a convolution of Breit-Wigner and Gaussian functions for the signal and exponential for the background. The fits to dimuon invariant distributions are shown in Fig. 5.3. Solving Eq. 5.4, we obtain that the isolation efficiency for signal muons from Z boson decays is 96.1 %. This efficiency is for inclusive Z muons and therefore artificially high due to the large fraction of events without any jets. We will re-calculate the isolation efficiency for Z candidate events with ≥ 1 jets when we discuss the background estimation.

5.2.2 Jet Selection and b-tagging

For this analysis, we use calorimeter jets reconstructed with the cone algorithm of radius size 0.5. The jet selection cuts are summarized below:

- Pass L1 confirmation (defined in chapter 4)
- $0.05 <$ EM-fraction < 0.95
- CH-fraction < 0.4
- n90 > 1
- Jet energy scale (JES) corrections (v05-01-00)
- $E_T \geq 20.0$ GeV (corrected energy)
- $|\eta| \leq 2.5$

The selected calorimeter jets are required to be *taggable* before the b-tagging as described in chapter 4. Jets are required to match the reconstructed track

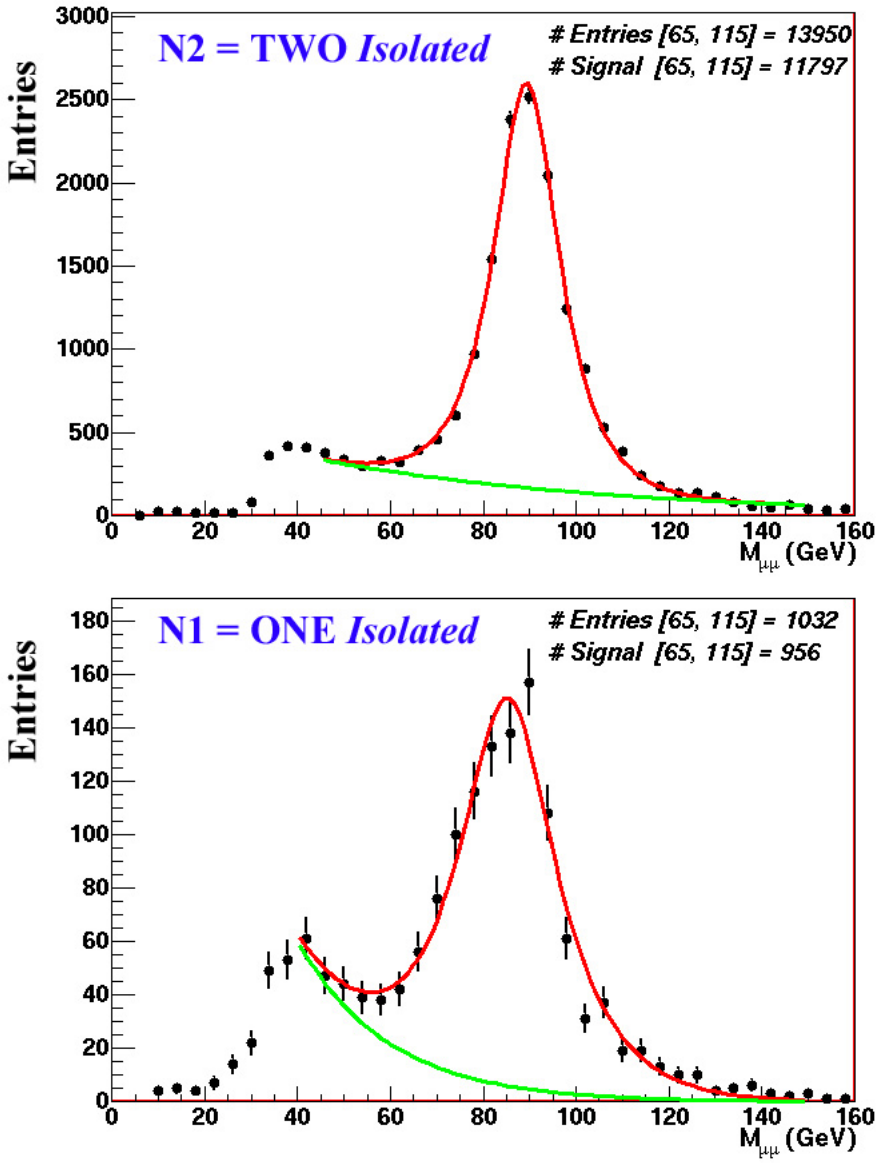

Figure 5.3: The invariant mass distributions for the dimuon candidates with both muons isolated (upper plot) and one and only one of the muons isolated (lower plot) Total number of candidate events within a mass window of [65, 115] GeV is shown on the upper right corner of the plots along with the integral of the signal function within the same window showing the number of actual Z candidates. The isolation efficiency is obtained using the relation in Eq. 5.4 and using the fit results, it is estimated to be 96.1 %.

jets within a matching $\Delta R_{track-jet,cal-jet}$ of 0.5. For tagging b-jets, we use the secondary vertex b-tagging method and consider TIGHT secondary vertices, which have a decay length significance larger than 7. The taggable calorimeter jets are matched to secondary vertices if ΔR between the jet axis and the secondary vertex momentum vector is smaller than 0.5.

The jet multiplicity distributions for all jets, taggable jets and b-tagged jets are shown in Fig. 5.4 for events with selected Z candidates. The jet reconstruction efficiency does not have a direct effect on the cross-section ratio and cancels out completely if the heavy quark and light quark jet reconstruction efficiencies are the same. We investigated this hypothesis with the simulation and measured the calorimeter jet reconstruction efficiencies for different types of quarks with respect to particle jets[2]. The jet reconstruction efficiencies for heavy and light quarks are shown in Fig. 5.5, obtained from $Z \to b\bar{b}$, $Z \to c\bar{c}$, and $Z \to q\bar{q}$ (where $q = uds$) simulation.

The lower plots on Fig. 5.5 show the ratio of jet reconstruction efficiencies for b quarks compared to light quarks (lower left) and c quarks (lower right). We observe a 2 % difference in the jet reconstruction efficiencies of b and light quark samples but see almost no difference in b and c quark samples. Since our understanding of these differences are rather unsophisticated at this time, we prefer using the hypothesis of cancelling the jet reconstruction efficiency differences in the ratio calculation but treat the difference observed in MC as a systematic source of uncertainty. Systematic effects will be investigated later in this chapter.

We also measured the efficiency of the taggability requirement in our data to be 78.6 $\pm$ 0.9% per jet. The same taggability efficiency is measured to be in 88.2 $\pm$ 0.3% in $Z+j$ MC and 90.6 $\pm$ 0.4% in $Z+b$ MC. Assuming that most of the

[2]MC particle jets are clusters of generated stable particles reconstructed using an algorithm similar to calorimeter jet reconstruction.

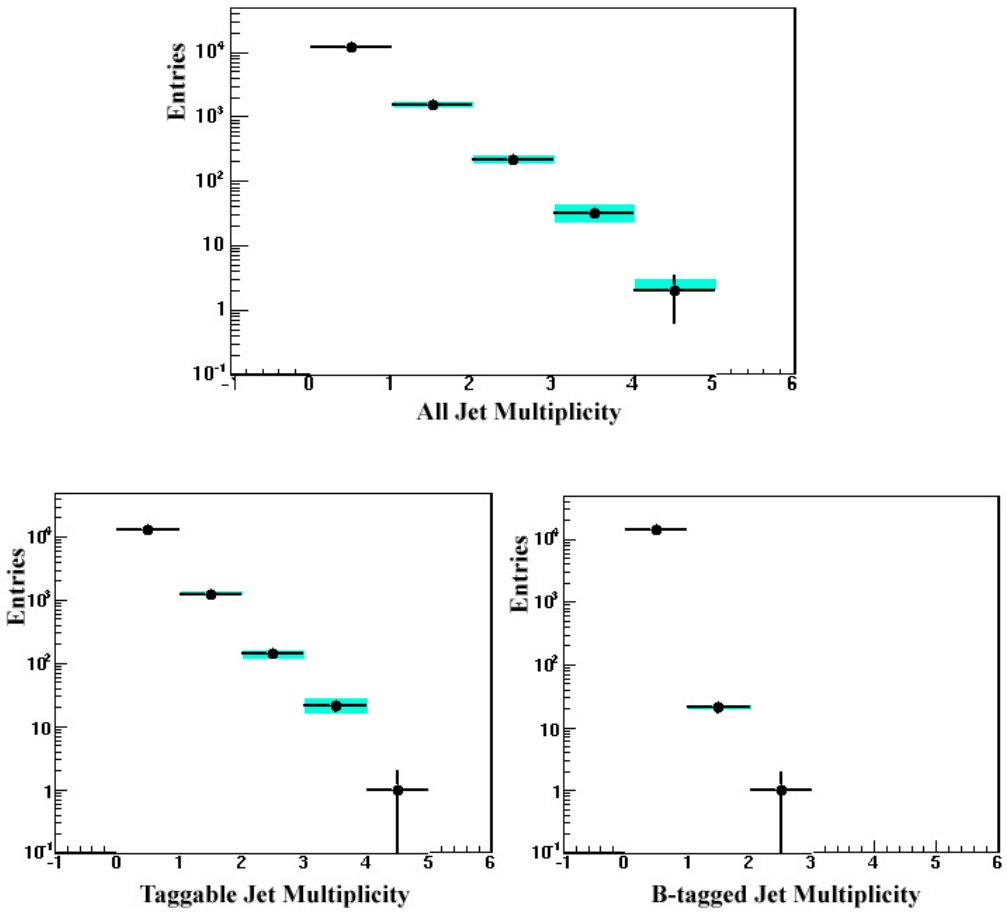

Figure 5.4: Jet multiplicity in data for all jets (upper plot), taggable jets (lower left) and b-tagged jets (lower right). The filled bars represent the uncertainty from the error in jet-energy scale.

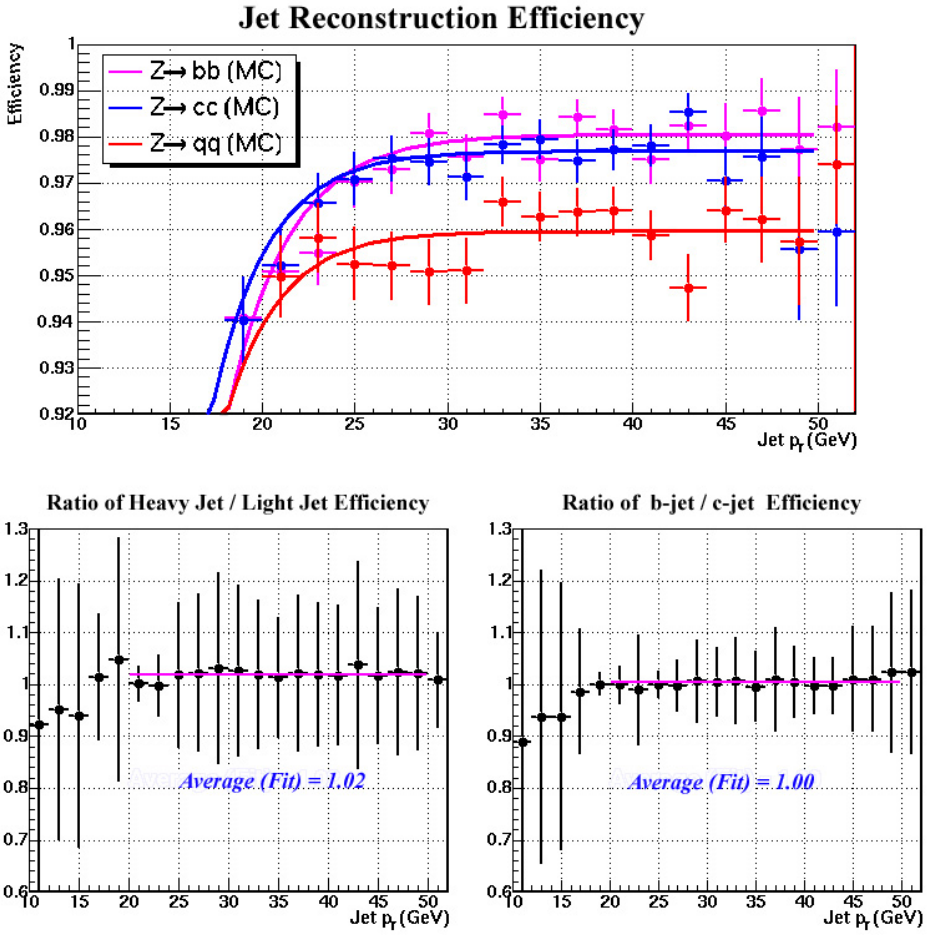

Figure 5.5: The jet reconstruction efficiencies for b/c and light quarks as measured in $Z \to b\bar{b}$, $Z \to c\bar{c}$, and $Z \to q\bar{q}$ (where $q = uds$) simulation with respect to particle jets (abscissa of the plots represent the particle jet momentum). The lower plots show the ratio of reconstruction efficiencies for b vs light quark (lower left) and b vs c quark (lower right). Although the jet reconstruction efficiencies for b and c quarks are similar, they are about 2 % higher than the light quarks.

jets in data are light-quark jets, we take the difference in data and $Z + j$ MC to scale the taggability of jets in $Z+b$ MC and find the heavy jet (i.e. b/c) taggability in data as shown in Eq. 5.5. Therefore, we estimate the heavy jet taggability in data to be 80.7 ± 0.5(stat) ± 0.4(syst)% where the systematic error is obtained by comparing the taggability in $Z + b\bar{b}$ MC, with the one from $Z + b$ MC.

$$t_B^{data} = t_L^{data} \times \frac{t_B^{MC}}{t_L^{MC}} \tag{5.5}$$

The b-tagging efficiencies in data for b and light jets have been estimated by others as functions of jet p_T and η [77] and [85]. Similar parametrizations are also available for the b-tagging differences as observed in data and MC (scale-factor) due to the imperfections in the simulation. The contribution from c quarks (hence c-jets) to our final data sample is non-negligible, and since there is no available way of measuring the c-jet tagging efficiency in data, we rely on simulation to estimate c-jet tagging efficiency and scale it using the same scale factor derived for b-jets. For the kinematics of the jets in our dimuon candidate events, we obtain an average b-tagging efficiency of 33.13 ± 1.12(syst)% for b-jets, 8.42 ± 0.06(syst)% for c-jets and mistag rate of about 0.24 % for light jets.

The heavy quark (b and c) tagging efficiencies quoted above incorporate a correction factor applied for jets that do not contain muons inside their cone (i.e. non-muonic jets). This correction factor is applied since the original efficiency measurements are obtained for jets that contain a muon within their cone (i.e. muonic jets). We relied on simulation to obtain the ratio of the tagging efficiencies of non-muonic jets to muonic jets and measured this factor to be 85.7 ± 1.6% [86].

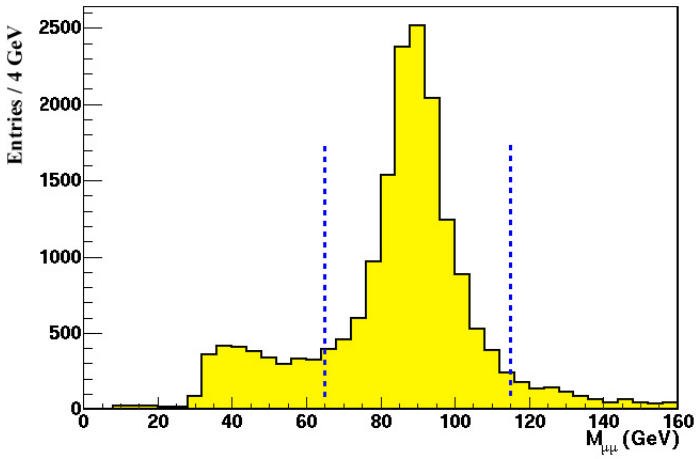

Figure 5.6: The $\mu^+\mu^-$ invariant mass for Z candidates in data. The number of Z candidates from the fit to this sample yields about 11543 within the invariant mass window of [65.0, 115.0] GeV . For the fit, we used an exponential function to model the background and then subtracted the fit from the original histogram to calculate the Z contribution.

5.3 Candidate Events

The dimuon mass distribution in Fig. 5.6, shows that there are about 11797 Z candidates in our data-set, as subtracted from the background fit in the invariant mass distributions (shown in Fig. 5.3). After the dimuon invariant mass window cut and requiring at least one calorimeter jet, this sample is reduced to 1754 events. The taggability requirement on the calorimeter jets reduces the number of Z candidate events with one or more jets to 1406 events. Finally, applying b-tagging on the taggable jets leaves only 22 dimuon events with one or more b-tagged jets. The summary for the number of candidate events is given in Table 5.2 and the dimuon mass distributions for events with one or more taggable jets and b-tagged jets can also be seen in Fig. 5.7

The taggable jet transverse momentum (p_T) and pseudo-rapidity (η) distributions are shown in Fig. 5.8 and 5.9 from Z+jet candidate events respectively,

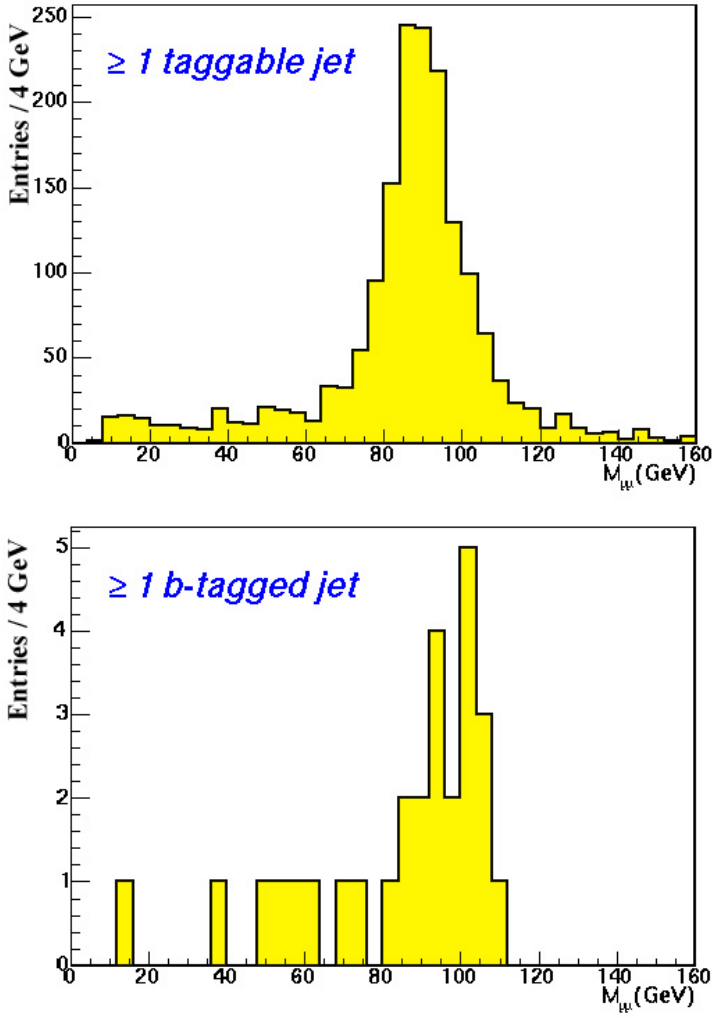

Figure 5.7: Dimuon invariant mass distribution in data, where both muons are required to be isolated. In the upper plot, at least 1 taggable jet present in the event, whereas lower plot requires at least 1 b-tagged jet present in the event along with the dimuon candidate. The distributions are shown with no cut on the dimuon invariant mass.

Event Selection	# Events
$Z(\mu\mu)+ \geq 1$ jet	1754
$Z(\mu\mu)+ \geq 1$ taggable jet	1406
$Z(\mu\mu)+ \geq 1$ b-tagged jet	22

Table 5.2: The number of events left after successive selections of candidate events in the Z mass region. The number of events after the b-tagging jet selection is almost exclusively formed of $Z + 1b$-jet events except for one event, which has 2 b-jets.

overlayed with similar distributions from Z+jet MC. The MC and data plots are normalized to the same number of Z bosons and the MC jets are further scaled with data to MC jet reconstruction efficiency difference as discussed in the previous chapter. These kinematic distributions are also overlaid with the expected dimuon background which will be discussed in the next section. We observe that the taggable jet kinematic properties are consistent with the expectations from the simulations within the known uncertainties such as the jet energy scale correction uncertainty shown as the colored bars around the data points.

A schematic two dimensional (transverse plane) view of a dimuon candidate event with a b-tagged jet can be seen in Fig. 5.10.

5.3.1 Background Calculations

In the selection of the Z boson candidate events, we require two high-p_T isolated muons, but due to the inefficiencies in our selection criteria, not all of the selected events are real Z boson candidates even though the invariant mass of the dimuon is close to the Z mass. Most of the background events are due to the semi-leptonic decays of heavy quarks and some of these muons pass the isolation criteria and appear as muons from Z boson. Since this multi-jet background is mostly a result

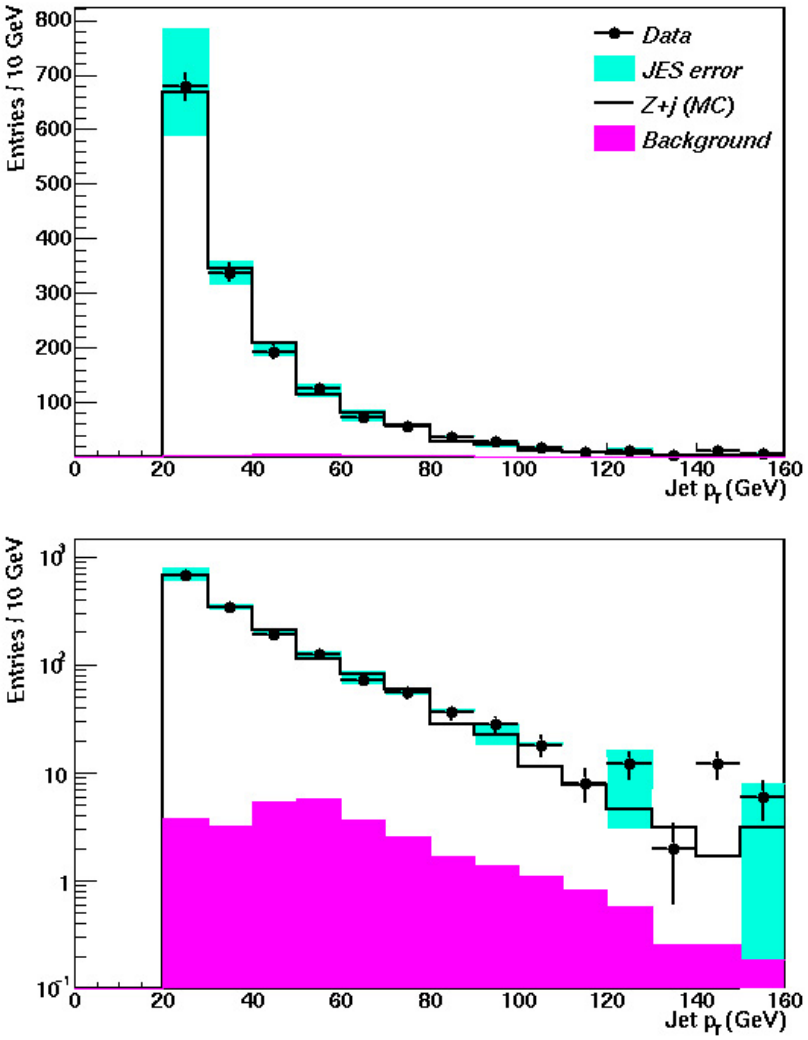

Figure 5.8: The comparison of taggable jet p_T in Z candidate events (bars) and expectation from Z+jet (black line) and dimuon background (magenta-filled histogram). Upper plot is on linear and lower on logarithmic scale. The normalization of the QCD background is calculated in the text and the shape of this background is obtained from the jets in the anti-isolated dimuon data sample. The simulation is normalized to the same number of dimuon candidates as observed in the data within the mass region [65.0, 115.0] GeV . The number of simulated jets are also corrected by the data versus MC jet reconstruction efficiency difference.

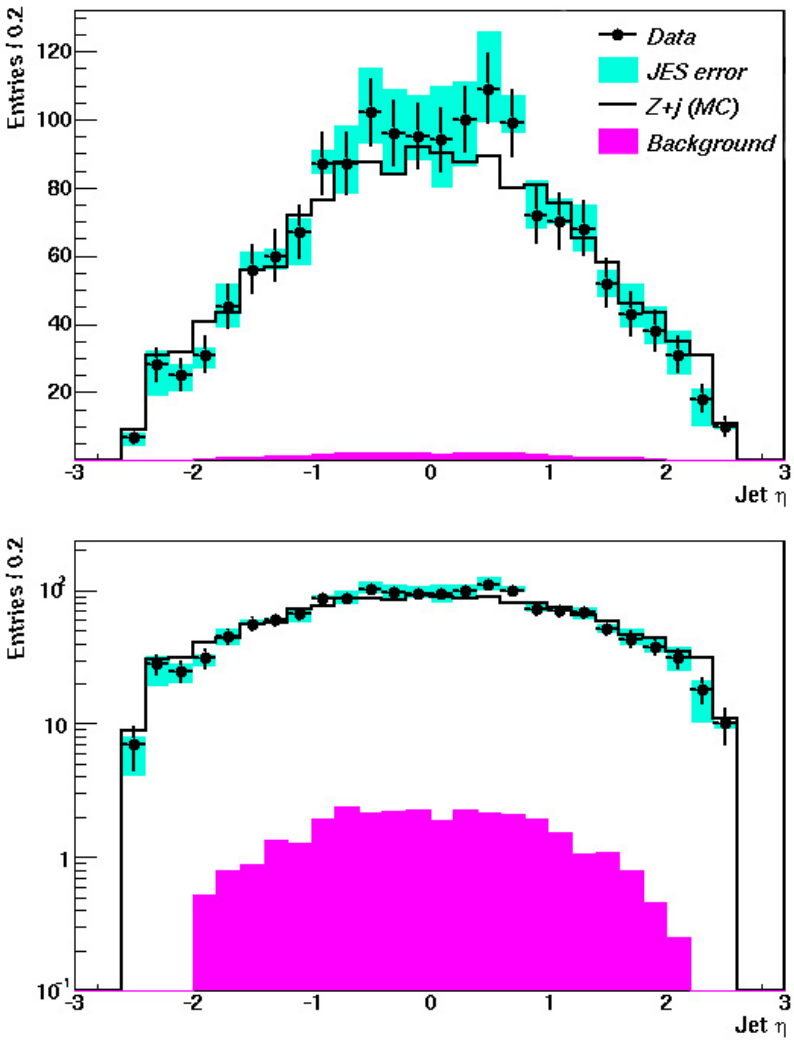

Figure 5.9: The comparison of taggable jet η in Z candidate events (bars) and expectation from Z+jet (black line) and dimuon background (magenta-filled histogram). Upper plot is on linear and lower on logarithmic scale. The normalization of the QCD background is calculated in the text and the shape of this background is obtained from the jets in the anti-isolated dimuon data sample. The simulation is normalized to the same number of dimuon candidates as observed in the data within the mass region [65.0, 115.0] GeV . The number of simulated jets are also corrected by the data versus MC jet reconstruction efficiency difference.

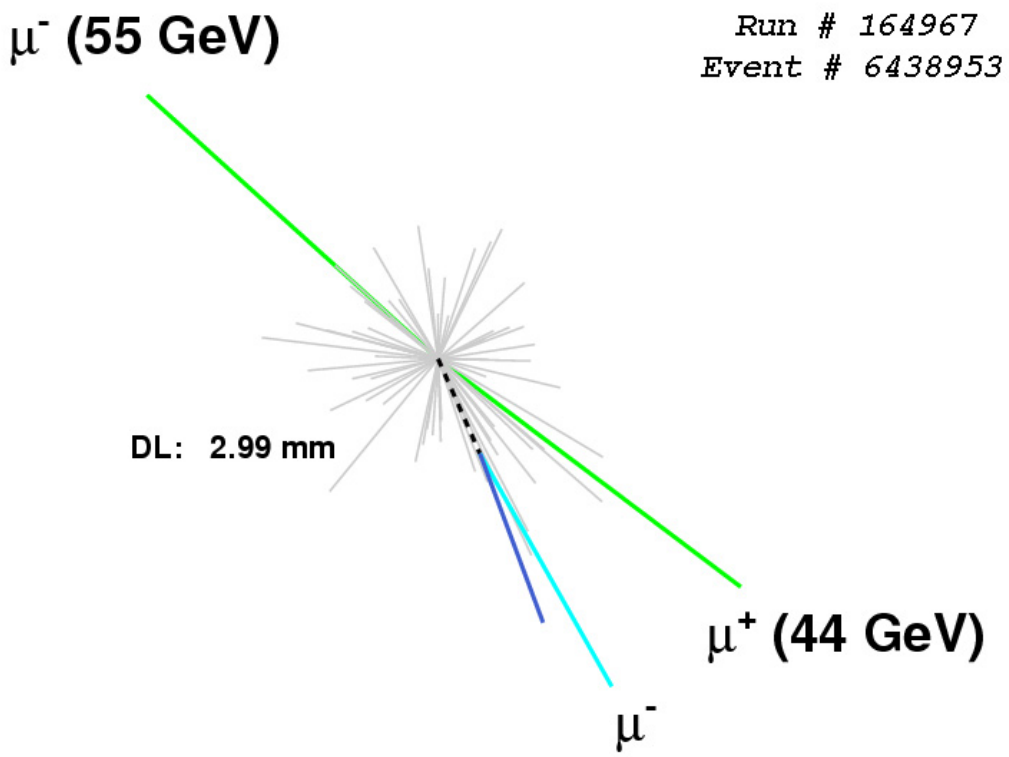

Figure 5.10: A schematic two dimensional $(r - \phi)$ view of a dimuon candidate event with a b-tagged jet. The two green tracks indicate the muons making the Z candidate and the dark blue line shows the direction of the calorimeter jet which happens to be tagged by an existing secondary vertex with a decay length of about 3 mm and also contains a soft muon.

of the inefficiency of the isolation criteria, we use this selection for the estimation of the multi-jet contamination in the selected dimuon candidate events with one or more taggable jets. This method, explained below, is called the "*matrix method*".

As we discussed in the beginning of this chapter, the efficiency for satisfying the isolation criteria can be calculated for Z muons using the fits to the invariant mass distributions for dimuon candidates of one (N_1) and two isolated muons (N_2). Using the same technique, we find that the isolation efficiency for Z muons is 84.9 $\pm$ 0.2 %. We note that this efficiency is lower than the previously quoted value of 96.1 % since this measurement is for muons in dimuon events with one or more taggable jets. Our previous measurement was for the inclusive jets which includes a large fraction of dimuon events with no reconstructed jets. The error on our measurement is derived from the variations of the fit resulting from modified fitting regions. This uncertainty is propagated as a systematic uncertainty in the background estimations discussed below.

We argue that the isolation efficiency for the real Z muons also represents the efficiency for muons from Drell-Yan sources (Z/γ^* continuum) within the same dimuon mass window. The underlying physics process is similar for these two types of events and given the similar kinematics due to the same invariant mass window, we expect these muons to have similar efficiencies for isolation with respect to the reconstructed jets. Therefore, we collectively call the calculated efficiency the isolation efficiency for DY (Drell-Yan) muons (ϵ_{DY}). However, it is very natural to expect that the isolation efficiency of muons from multi-jet/QCD sources (ϵ_{QCD}) should be significantly different due to the differences in the production and kinematics of muons with respect to jets in such events.

In order to estimate the multi-jet background contribution in our $Z+\geq$ 1-jet and b-tagged jet samples, we first calculate the isolation efficiency for background-like muons. The equations 5.6, 5.7 and 5.8, give the relation between the number of

candidates observed in the dimuon samples with no consideration for their isolation (N_{TOTAL}), for two isolated muons (N_2) and absolutely no isolated muons (N_0), respectively.

$$N_{TOTAL} \equiv N_{QCD} + N_{DY} \tag{5.6}$$

$$N_2 = \epsilon_{QCD}^2 N_{QCD} + \epsilon_{DY}^2 N_{DY} \tag{5.7}$$

$$N_0 = (1-\epsilon_{QCD})^2 N_{QCD} + (1-\epsilon_{DY})^2 N_{DY} \tag{5.8}$$

The labels in the matrix-method equations have the following meanings (event numbers, N_x, represent the event counts of dimuon events with invariant masses within the mass window we use for the analysis. The events are also required to have at least 1 taggable jet, or a b-tagged jet present in the event if the corresponding label is superscripted with letter "B"):

- N_{QCD} = Number of multi-jet (QCD) background events
- N_{DY} = Number of events from DY and Z processes
- ϵ_{QCD} = Efficiency of isolation requirement for muons in QCD events
- ϵ_{DY} = Efficiency of isolation requirement for muons from DY/Z sources
- N_2 = Number of events where both muons are isolated
- N_0 = Number of events where none of the muons are isolated

The unknowns to be solved for are N_{DY}, N_{QCD} and ϵ_{QCD}. Given the isolation efficiency for Z muons (ϵ_{DY}) calculated above and the number of observed events with all types of muons ($N_{TOTAL} = 2134$), exactly two ($N_2 = 1406$) and no isolated muons ($N_0 = 132$), we calculate the contributions from DY and QCD sources using the matrix-method equations presented in equations 5.6 through 5.8. In order to

Derived Quantity	Value
N_{DY}	1950.61 ± 390.12(stat) ± 26.05(syst)
N_{QCD}	183.39 ± 36.68(stat) ± 9.50(syst)
ϵ_{QCD}	30.92 ± 1.24(syst) %

Table 5.3: The derived quantities of the matrix method, the descriptions are given within the text.

solve these equations, we have to make an initial assumption that the contribution from QCD to the events with two isolated muons (N_2) is negligible as compared to the DY contribution. This is a legitimate assumption given the small levels of non-resonant contribution in the dimuon invariant mass as seen in Fig. 5.7 and the fact that the efficiencies contribute in quadrature to Eq. 5.7. In any case, since this is an assumption in our background calculations, we estimate its effect as a source of systematic uncertainty. This uncertainty is calculated by treating the difference in the first-pass result for N_2 (given by Eq. 5.7) and the actual observed number of dimuon candidates with two isolated muons. Without our initial assumptions, these numbers should perfectly agree but in the presence of the initial assumption, there is a difference of 1.25 % in N_2 and this factor is propagated to all other calculations. This procedure provides a feed-back of the first-pass estimation to the final calculation in the form of a systematic uncertainty and enables the result to be within a stable value established in an iterative way.

The results of the background calculation are summarized in Table 5.3. We find that of 1406 Z+taggable jet events (N_2), 17.53 ± 3.51(stat) ± 2.20(syst) events are from multi-jet background sources (i.e. $\epsilon^2_{QCD} N_{QCD}$).

Furthermore, we calculate the multi-jet contribution to the b-tagged sample of 22 events by looking at the sample where both of the muons are anti-isolated

(N_0^B) and at least 1 b-tagged jet is present in the event.

$$N_0^B = (1-\epsilon_{QCD})^2 N_{QCD}^B + (1-\epsilon_{DY})^2 N_{DY}^B \quad (5.9)$$

$$N_{QCD}^B \simeq \frac{N_0^B}{(1-\epsilon_{QCD})^2} \quad (5.10)$$

As mentioned before, the superscript "B" represents that the numbers are relating the contributions in the b-tagged samples (eg. N_{QCD}^B represents the contribution from multi-jet/QCD background in the $\geq$ 1 b-tagged-jet sample). In order to arrive at Eq. 5.10 from Eq. 5.9, we apply the same assumption we used earlier (i.e. $(1-\epsilon_{QCD})^2$ is small with respect to $(1-\epsilon_{DY})^2$) and estimate the effect of this assumption in our result as a systematic uncertainty. Given our observation that N_0^B is 25 events, i.e. the number of events where there are two anti-isolated muons and at least 1 b-tagged jet, we can calculate the QCD contribution to 2 isolated muon & b-tagged jet sample.

$$N_2^B = \epsilon_{QCD}^2 N_{QCD}^B + \epsilon_{DY}^2 N_{DY}^B \quad (5.11)$$

$$\text{QCD Background} \equiv \epsilon_{QCD}^2 \; N_{QCD}^B \quad (5.12)$$

$$\text{QCD Background} = \frac{\epsilon_{QCD}^2 \; N_0^B}{(1-\epsilon_{QCD})^2} \quad (5.13)$$

Plugging in the relation for N_{QCD}^B derived in Eq. 5.10 to Eq. 5.12, we arrive at Eq. 5.13. Using the isolation efficiency we calculated for the background muons and the value for N_0^B (25 events), we finally estimate the number of multi-jet/QCD contribution to the $Z + b$-jet sample as 5.01 $\pm$ 1.00(stat) $\pm$ 0.56(syst) events.

A summary of multi-jet background calculation results can be found in Table 5.4.

Background	Expected Contribution (# events)
QCD in $Z+ \geq 1$ taggable-jet	17.53 ± 3.51(stat) $\pm$ 2.20(syst)
QCD in $Z+ \geq 1$ b-tagged jet	5.01 ± 1.00(stat) $\pm$ 0.56(syst)

Table 5.4: Multi-jet/QCD background contributions to untagged (Z + taggable-jet) and b-tagged ($Z + b$-jet) samples.

5.4 Tests for b-tagging

To test the validity of b-jets, tagged with secondary vertices (SVTX), we utilized a different tagging method, namely the impact parameter b-tagging method (JLIP) discussed in the previous chapter. Out of the 22 events which at least one SVTX tagged jet, we observe that only 14 of these events are also tagged by the JLIP method.

These numbers alone do not give us much information if we do not have a quantitative and independent way of measuring the correlations of the two algorithms and it is quite natural to expect that these correlations will be strongly dependent on the nature of underlying quark type. Measuring the correlations for b, c and light quarks is only possible with simulation but due to the slight differences in tracking in MC and data, it is not guaranteed that the correlations found in MC will also apply to data.

In order to put this hypothesis to test, we analyzed the *MuJet* skim as an independent data to measure the correlations. The skim is made of collider data consisting events with at least one jet of transverse momentum larger than 15 GeV and a MEDIUM quality muon of $p_T > 4$ GeV in the event where the muon is also required to be near the jet axis specified by a ΔR cut smaller than 0.7.

In order to select the b-jets, we used the tag and probe method and further skimmed the original sample for events with 2 back to back jets ($\Delta\phi > 2.5$). To

Quark Type (MC)	JLIP & SVTX Correlation
b quark jets	79.2 % (C_B)
c quark jets	56.1 % (C_C)
light-quark jets	22.4 % (C_L)

Table 5.5: Correlations of JLIP and SVTX b-tagging algorithms in MC for different quark types.

increase the purity of the selected events for being b-jet events, we required the tag jet to be tagged by both soft-lepton tagging[3] (lepton is muon, in this case) and SVTX algorithms, and analyzed the away-side jet (probe jet) in these events. Since the first tag jet is b-tagged by two independent algorithms, the probability that this is a real b-jet is high (an approximate calculation yields that this probability is higher than 95 %). We measure the correlation of the SVTX and JLIP algorithms using this away-side jet and find that 77.1 $\pm$ 1.4 % of the SVTX tagged away-side jets are also tagged by JLIP algorithm.

The similar measurement in MC, this time using the generated B-hadrons in $Z + b$ MC to increase the purity, gives us 79.2 % for the same correlation. These two results are statistically consistent and increase the confidence in the hypothesis that the b-tagging correlations for JLIP and SVTX algorithms are similar in data and MC.

The correlations using different samples are summarized in Table 5.5. Using these correlations, we can arrive at the expected number of JLIP tagged events in the $Z + b$-tagged jet sample of 22 events and these are shown in Table 5.6. Out of 22 events tagged with SVTX algorithm, we expect 14.33 $\pm$ 3.38(stat) events

[3]Soft lepton tagging is another b-tagging method where the p_T^{rel} of the muon found in the jet is used to discriminate b-jets agains other type of jets.

Source of Contribution	Expected Events
$Z + b$ contribution	$9.19 \times C_B = 7.28$ events
$Z + c$ contribution	$3.95 \times C_C = 2.22$ events
$Z + j$ contribution	$3.85 \times C_L = 0.86$ events
QCD contribution	$5.01 \times C_B = 3.97$ events
Total expected	14.33 ± 3.38(stat) events out of 22 events

Table 5.6: Using the correlations found between the two b-tagging methods, we multiply these correlations with the expected contributions from light quark, b and c quark as well as background contributions in the 22 b-tagged jet events. Since we expect most of the QCD background to be heavy quark events with semi-leptonic decays, we use the b quark correlation (i.e. C_B) for these events.

also to be tagged by the impact parameter b-tagging algorithm. Applying this b-tagging algorithm explicitly on these events, we indeed obtain 14 tagged events, confirming our expectations and that our sample contains $Z + b$-jet events as we have calculated.

In the calculation of total expected tagged events with the impact parameter algorithm, we assumed that the correlation for the QCD events are consistent with the correlations for b-jet events since we believe most of the QCD background is due to the $b\bar{b}$ contribution. The method presented here is not an exact procedure for testing the b-tagging used in this analysis but given the statistical uncertainties calculated shown in Table 5.6, the consistency of our results with the expectations increase our confidence in our result and b-tagging methods.

5.5 Ratio of Cross-Sections

In order to measure the ratio of cross-sections, we need to scale the events back with the corresponding efficiencies in order to find their contributions before b-tagging and taggability. However, all the efficiencies we calculated from data reflect the efficiencies per jet and since our measurement is an inclusive quantity, we need to find a relation between the per jet taggability efficiency and per event efficiency due to the events with more than one jet.

In the case of an event with non-zero number of jets, the efficiency to accept this event with a requirement of one or more jets can simply be written as 1 minus the efficiency to reject the evet. An event is rejected with a rate which is equal to the product of the rejection rate of each jet in the event, i.e. $\prod_{j=1}^{n_{jets}} (1 - \epsilon_j)$ where ϵ_j is the efficiency to accept a specific jet. Therefore, the light jet efficiencies are converted to event efficiencies by using the number of jets in Z+jet events in data and average event efficiency is found using the relation given in Eq. 5.14.

$$\epsilon^{event} = \frac{1}{N_{events}} \cdot \sum_{i=1}^{N_{events}} \left[1 - \prod_{j=1}^{n^i_{jets}} (1 - \epsilon_j^{jet}) \right] \tag{5.14}$$

However, estimating the effect of the jet multiplicities for the heavy jets (b and c-jets) is more involved since we do not know how many heavy quark jets are actually produced in the b-tagged events. In order to measure the effect of the heavy quark event contributions with more than one b and c quarks in the final state, we obtain the fraction of such events from theoretical calculations [20]. According to the theoretical estimations using CTEQ6 PDF set [10], in the case of $Z + b$-quark production, the fraction of two quark final state[4] is 10.8 % of the total inclusive Z+heavy quark production ($f^b_{Q\bar{Q}} = 0.108$) and the same fraction is

[4]Excluding the cases where the two quarks fall into the same jet cone of size 0.5 and reconstructed as one jet.

Efficiency	Per Jet Efficiency (%)	Per Event Efficiency (%)
Light jet taggability	78.6	80.3
Light jet b-tagging rate	0.24	0.27
b-jet taggability	80.7	82.4
b-jet b-tagging	33.1	35.5
c-jet taggability	80.7	81.7
c-jet b-tagging	8.42	8.94

Table 5.7: Since the measurement presented in this thesis is an inclusive measurement, we make corrections to measured efficiencies for jet multiplicities in the events. The effect of this correction is seen when the per jet and per event efficiency columns are compared. We use the efficiencies presented in the last column of the table above.

6.7 % for the c quarks ($f^{c}_{Q\bar{Q}} = 0.067$). In a similar way as we did for the light jet efficiencies, we also correct the efficiencies for the existence of events with more than one quark produced as in Eq. 5.15. We apply this correction for b and c-jet taggability and b-tagging efficiencies. The efficiencies before (per jet efficiency) and after (per event efficiency) the jet multiplicity corrections are listed in Table 5.7.

$$\epsilon^{event} = (1 - f_{QQ}) \cdot \epsilon^{jet} + f_{QQ} \cdot \left[1 - (1 - \epsilon^{jet})^2\right] \tag{5.15}$$

In order to find the original b, c and light quark contents in the selected events, we write the relations for different contributions of sources in the samples before and after b-tagging as shown in equations 5.16 and 5.17, respectively.

$$\begin{aligned} 1406 &= t_b\ N_B + t_c\ N_C + t_l\ N_L + N_{QCD} \\ 1406 - 17.53 = 1388.47 &= t_b\ N_B + t_c\ N_C + t_l\ N_L \end{aligned} \tag{5.16}$$

$$\begin{aligned} 22 &= t_b\ \epsilon_b\ N_B + t_c\ \epsilon_c\ N_C + t_l\ \epsilon_l\ N_L + N_{QCD_B} \\ 22 - 5.01 = 16.99 &= t_b\ \epsilon_b\ N_B + t_c\ \epsilon_c\ N_C + t_l\ \epsilon_l\ N_L \end{aligned} \tag{5.17}$$

The two equations presented above (5.16 and 5.17) are not sufficient to solve for the three unknows we have (N_B, N_C and N_L). In order to solve these equations, we assume that the inclusive $Z+c$ production cross section is a factor of 1.69 larger than the inclusive $Z+b$ cross section as obtained from theoretical estimations [20].

$$N_C = 1.69 \times N_B \tag{5.18}$$

Solving the equations 5.16 through 5.18 simultaneously, we obtain the following estimates for the number of Z+light-jet, $Z + b$-jet and $Z + c$-jet events produced where the errors are purely statistical.

- $N_B = 32.16 \pm 8.83$ (stat)
- $N_C = 54.35 \pm 14.92$ (stat)
- $N_L = 1641.62 \pm 47.40$ (stat)

From the numbers above, we can calculate the the ratio of production cross sections given in Eq. 5.19.

$$\frac{\sigma(Z+b)}{\sigma(Z+j)} = (1.86 \pm 0.44\ (\text{stat})) \times 10^{-2} \tag{5.19}$$

Having calculated different flavor contributions in our samples, we can compare the jet kinematic distributions correctly normalized and overlayed with the distributions obtained in data. The b-tagged transverse momentum distribution can be seen in Fig. 5.11 overlayed with expected contributions from real b-jets as well as c-jet, light-jet and multi-jet/QCD background sources. The distributions

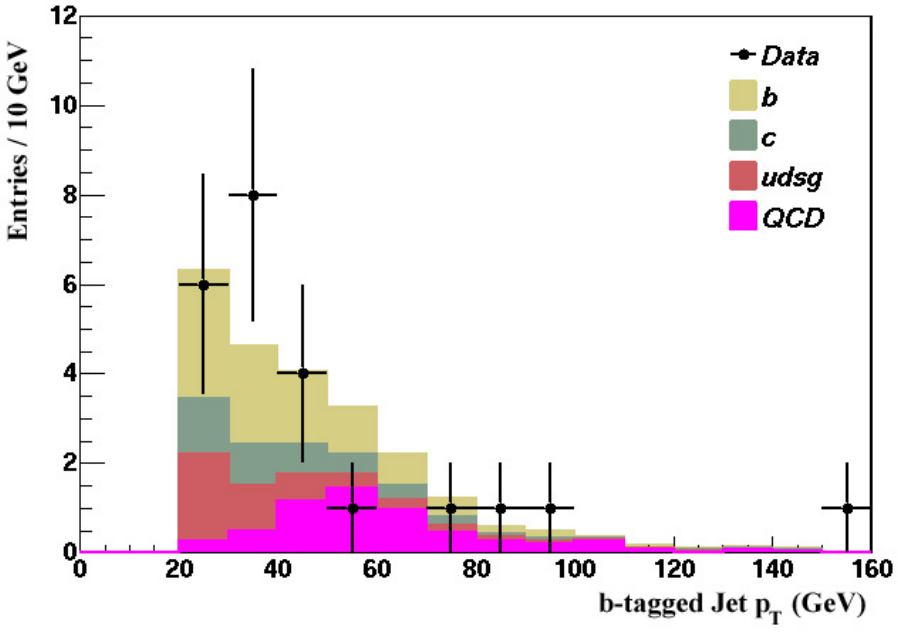

Figure 5.11: The comparison of b-tagged jet p_T in data and MC. The color-fill histograms, except the QCD contribution, are taken from corresponding MC samples with weights estimated as explained in text. The shape of the QCD contribution is estimated using the b-tagged jets in the non-isolated dimuon data sample.

are in good agreement with expectations. Similar normalized distributions are also plotted for the secondary vertices used for tagging the b-jets. We show the secondary vertex track multiplicity distribution in Fig. 5.12 and the consistency between the vertices found in data and expectations from simulation is good.

In addition to comparing the secondary vertex track multiplicity observed in data to our expectations, we also look at the secondary vertex decay length significance since it also provides a test of the validity of displaced vertices. Fig. 5.13 shows the decay length significance distributions for the reconstructed secondary vertices. Even though we apply a decay length signifance cut and remove secondary vertices with significance values smaller than 7, we remove this cut for

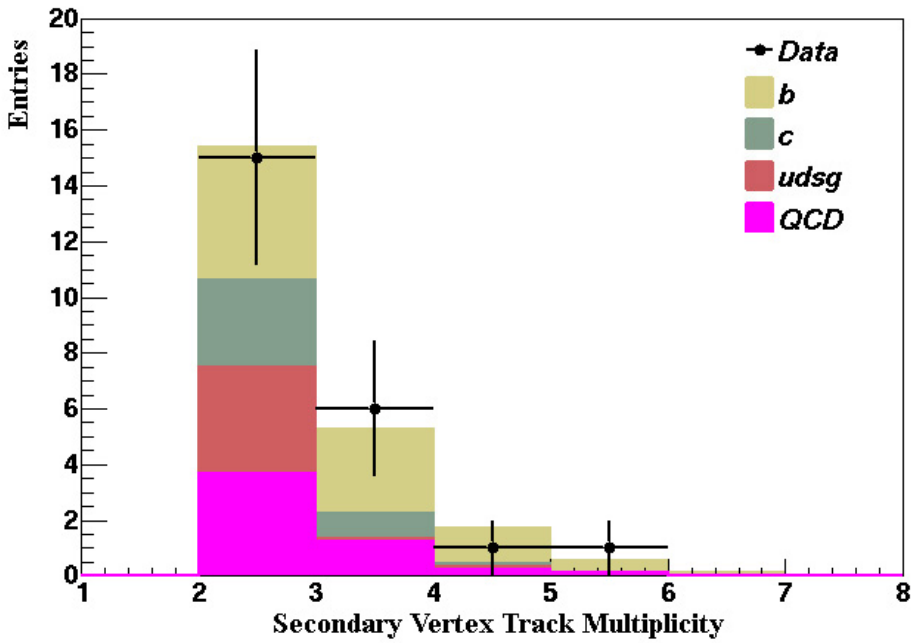

Figure 5.12: Secondary vertex track multiplicity. The color-fill histograms, except the QCD contribution, are taken from corresponding MC samples with weights estimated from the final data sample. The shape of the QCD contribution is estimated using the secondary vertices in the non-isolated dimuon data sample. These distributions are plotted only for those secondary vertices that are associated to calorimeter jets.

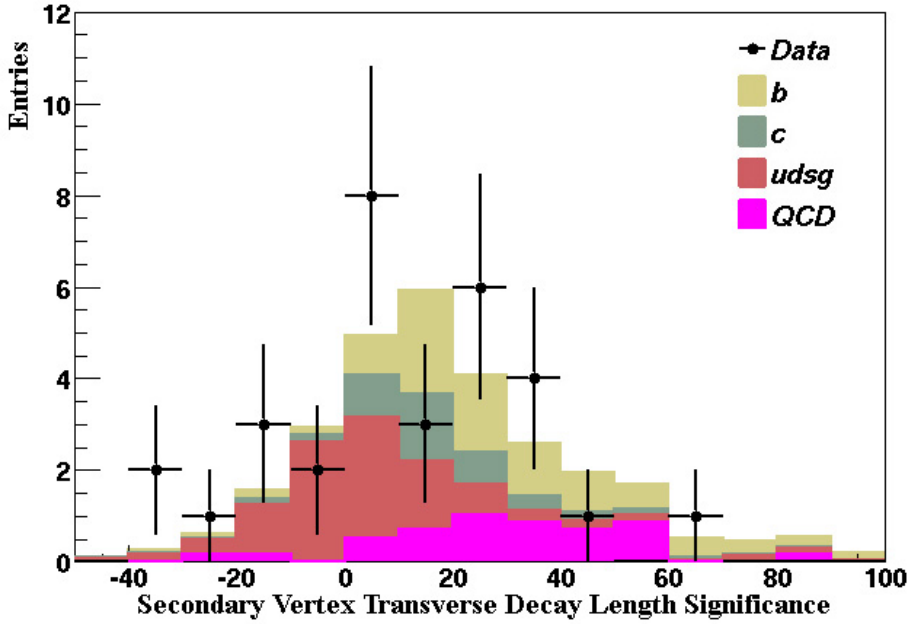

Figure 5.13: Secondary vertex decay length significance. Although we require the vertices to have a decay length significance of at least 7.0, we removed this cut for making this plot. The color-fill histograms, except the QCD contribution, are taken from corresponding MC samples with weights estimated from the final data sample. The shape of the QCD contribution is estimated using the secondary vertices in the non-isolated dimuon data sample. These distributions are plotted only for those secondary vertices that are associated to calorimeter jets.

Fig. 5.13 in order to observe and compare the distributions in different flavors of reconstructed secondary vertices.

5.6 Consideration of Systematic Uncertainties

The ratio of cross sections is subject to systematic uncertainties in fit parameters, errors from theoretical inputs and estimation procedures. The following sources are the major contributors to the systematic uncertainty in our measurement and quoted as absolute errors on the final result.

- **Uncertainty in the Background Estimation Before b-tagging**
  - We calculated the contribution of multi-jet/QCD background to the $Z+ \geq 1$ taggable jet sample to be 17.53 $\pm$ 4.14 events and we propagate the error on this estimate as a source of systematic error on our final measurement. Therefore, the systematic error from the QCD background before b-tagging, is calculated to be $\pm$ 0.01 $\times 10^{-2}$.
- **Uncertainty in the Background Estimation After b-tagging**
  - In the calculation of the QCD background after b-tagging, we also estimated uncertainty associated with our estimation. The overall QCD background estimate in the b-tagged sample was 5.01 $\pm$ 1.15 events. We propagate this error to the measurement and calculate the systematic uncertainty to be $\pm$ 0.16 $\times 10^{-2}$.
- **Differences in the Mistag Rate Functions from Different Data Sets**
  - The mistag rates are measured in two different data samples, one in data collected through a combination of jet triggers and another sample which is collected with the requirement of an EM object and an existing jet in the event (EMQCD). We observed slight differences in the mistag rates calculated from these two samples and this difference is taken to

be one of the sources of systematic error for our measurement. The effect of this difference on the final ratio of cross sections is ± 0.10 $\times 10^{-2}$.

- **Uncertainty in the Jet Energy Scale (JES)**
  - The jet energy scale correction is applied to all jets in the analysis but these corrections are associated with statistical and systematic uncertainties. Major systematic uncertainties stem from the instrumental background and the biases introduced in the selection of the data sets from which the energy corrections are derived [70]. To understand the effect of these uncertainties, we rescaled the jet energies by ± σ_{corr} and performed our calculations again. The background calculations are also scaled to reflect the changes in the jet energy distributions. The average effect of the uncertainty in jet energy scale error is -0.12 $\times 10^{-2}$ and +0.02 $\times 10^{-2}$ on the final ratio of cross sections.
  - The differences between the JES of the b-jets and light jets are also investigated in MC [86]. The uncertainty due to these differences are calculated to be -0.09×10^{-2} and $+0.10 \times 10^{-2}$ on the final ratio of cross sections.

- **Uncertainty in the b and c-jet b-tagging Efficiencies**
  - The b and c-jet tagging efficiencies are used in extracting the ratio of cross sections. These efficiencies are available as functions of jet transverse momentum and detector pseudo-rapidity regions [77]. They are also calculated with corresponding statistical and systematic errors which are due to the uncertainties regarding the measurement methods. We vary the jet efficiencies by ± σ_{eff} assuming that b and c

tag efficiencies are entirely correlated, repeat the analysis, and then measure the difference from the actual results.

The effect of uncertainty in b and c efficiencies is calculated to be -0.04×10^{-2} and $+0.05 \times 10^{-2}$ on the final ratio of cross sections.

- **Uncertainty in the Mistag Rate Function**
  - In a similar way we calculated the fluctations due to the b and c efficiency errors, we also propagated the error in the light jet mistag rate to our final result as well. The effect on the calculated measurement is found to be $\pm$ 0.04 $\times 10^{-2}$.
- **Uncertainty from the Hadronic Jet Correction for b-jet Tagging Efficiency**
  - It is mentioned early in this chapter that the b and c-jet tagging efficiencies are obtained from events with jets where the jet cone contains a muon. We correct the efficiencies for jets that do not contain a muon (non-muonic) and estimate the correction factor to be 0.857 ± 0.016(syst) [86] i.e. the ratio of non-muonic b-jet tagging efficiency to muonic b-jet tagging efficiency. The error comes from different MC samples used to estimate the correction factor.

    The effect of the corresponding uncertainty on the final ratio is assessed and the systematic uncertainty on the result is calculated to be -0.03×10^{-2} and $+0.04 \times 10^{-2}$.
- **Differences in the Jet Reconstruction Efficiencies for heavy and light quarks**
  - Although we used the hypothesis that the heavy-jet and light-jet reconstruction efficiencies cancel out in the cross section ratio calculation,

we showed in Fig. 5.5 that the heavy and light quark jet reconstruction efficiencies can be different as much as 2 %. We treat this difference as a source of systematic error and measure its effect on the final cross section ratio to be $\pm$ 0.04 $\times 10^{-2}$.

- **Uncertainty in Taggability Scale Factor for Data and MC**
  - We measured the taggability difference of MC and data jets (larger for MC), however this estimate has an systematic error due to the variation of different MC samples with which these differences are measured. The error on this scale factor is propagated to the final cross-section ratio and the resulting uncertainty is estimated to be $\pm$ 0.01 $\times 10^{-2}$.
- **Uncertainty in the Ratio of Expected $Z + c$-jet and $Z + b$-jet Production**
  - To decouple contributions from b and c events, we used the predicted ratio of $Z + b$-jet and $Z + c$-jet next-to-leading order inclusive cross sections, obtained from [20]. The theoretical uncertainties in these predictions are attributed to uncertainties for the selection of the renormalization and the factorization scale as well as the uncertainties in the heavy quark parton distribution functions. The total uncertainty for the ratio of $Z + b$-jet and $Z + c$-jet next-to-leading order inclusive cross sections is estimated to be 9.5 %. Using the ratio values scaled by $\pm$ σ_{ratio}, we recalculate our result and take the differences in the final result as a systematic uncertainty, which is found to be $\pm$ 0.05 $\times 10^{-2}$.
- **Uncertainty for the Event Efficiency Correction for Heavy Jet Events**
  - We discussed the correction we applied for obtaining the efficiencies per

event from efficiencies calculated per jet. We used theoretical input for estimating the fraction of heavy quark production with two quarks to the inclusive production. These fractions are assigned an uncertainty of 20 % consistent with the leading order cross-section calculations [20] [87].

We propagate the estimated uncertainty in the heavy quark taggability and b-tagging efficiencies due to the uncertainty in the theoretical input, to the final cross-section ratio and find the resulting uncertainty to be $\pm$ 0.03 $\times 10^{-2}$.

- **Uncertainty due to the Merged Heavy Quarks**

  - An important fraction of inclusive $Z + b$-jet (and $Z + c$-jet) final states include the processes where two heavy quarks are produced but being close to each other, are reconstructed as a single jet final state. Even though such an event would appear as a single jet event, the presence of the two heavy quarks (and hadrons) effects the b-tagging efficiencies in a substantial way. Such cases of quark merging are estimated to be $\sim$ 10 % (19 %) of the inclusive $Z + b$-jet ($Z + c$-jet) production [20].

    Using $Z + b\bar{b}$ and $Z + c\bar{c}$ simulation, we calculate that the b-tagging efficiency is significantly higher for jets containing two heavy quarks within their cone volume as compared to jets with single heavy quarks. This increase in b-tagging efficiency is estimated to be 40 % for b-jets and 60 % for c-jets.

    This increase in efficiency are used as input to calculate an average b-tagging efficiency for inclusive $Z + b$ and $Z + c$ events. The average efficiency is calculated to be 3.6% higher than the single jet efficiency for b-jets and 9.6 % for c-jets.

We treat this change in efficiency due to the non-negligible presence of merged heavy quark jets as another source of systematic uncertainty and find the resulting uncertainty on the ratio measurement to be $+0.10 \times 10^{-2}$.

Except for the systematic sources that effect the b and c-jet efficiencies in the same way, we treat the uncertainties uncorrelated and add them in quadrature for the final systematic uncertainty. The uncertainties on b-jet and c-jet efficiencies are assumed to be fully correlated. A summary of the systematic uncertainties on the number of $Z + b$-jet, $Z + c$-jet and Z+light-jet events as well as the ratio of cross-sections is provided in Table 5.8.

5.7 Conclusion

We conclude that the ratio of the inclusive $Z + b$-jet to Z+jet cross sections is found to be $1.86 \pm 0.44(\text{stat})^{+0.24}_{-0.28}(\text{syst})$ % and presented with more detail below:

$$\begin{aligned} \frac{\sigma(Z+b)}{\sigma(Z+j)} &= (1.86 \pm 0.44(\text{stat})^{+0.24}_{-0.28}(\text{syst})) \times 10^{-2} \\ N_B &= 32.16 \pm 8.83(\text{stat})^{+4.27}_{-5.50}(\text{syst}) \\ N_C &= 54.35 \pm 14.92(\text{stat})^{+7.62}_{-9.92}(\text{syst}) \\ N_L &= 1641.62 \pm 47.40(\text{stat})^{+184.58}_{-144.85}(\text{syst}) \end{aligned}$$

The theoretical calculation for the same cross-section ratio is $(1.8 \pm 0.4) \times 10^{-2}$ for the jet kinematics used in this analysis [88] and it is in good aggreement with our measurement.

Systematic Source	N_B (-/+)	N_C (-/+)	N_L (-/+)	Ratio (%)
Background After b-tag	2.81/2.81	4.74/4.74	7.71/7.71	0.16/0.16
Background Before b-tag	0.03/0.03	0.05/0.05	5.23/5.23	0.01/0.01
Mistag Rate Differences	1.81/1.81	3.06/3.06	4.97/4.97	0.10/0.10
Mistag Rate	0.71/0.71	1.20/1.20	1.95/1.95	0.04/0.04
Jet Energy Scale	3.22/1.21	5.44/2.05	144.28/184.05	0.12/0.02
b-jet vs light-jet JES	1.75/1.54	2.95/2.67	5.54/6.17	0.09/0.10
b/c tag efficiency (TRF)	0.79/0.84	1.34/1.41	2.30/2.18	0.04/0.05
Hadronic Jet Eff Corr.	0.57/0.60	0.96/1.01	1.64/1.57	0.03/0.04
Jet Reco. Eff (b vs. q)	0.64/0.67	1.08/1.13	1.83/1.76	0.04/0.04
Taggability SF Error	0.23/0.24	0.39/0.40	0.00/0.00	0.01/0.01
Error on $\sigma_{Z+c}/\sigma_{Z+b}$	0.86/0.91	3.75/3.55	2.73/2.88	0.05/0.05
20% Error on $Z + Q\bar{Q}/Z + Q$	0.53/0.55	0.89/0.92	1.22/1.19	0.03/0.03
Effect of Merged b/c Quarks	1.66/0.00	2.81/0.00	0.00/4.57	0.10/0.00
Total Syst. Error	5.50/4.27	9.92/7.62	144.85/184.58	0.28/0.24

Table 5.8: Summary of systematic uncertainties. Refer to the text for further explanations for the source of these uncertainties.

Chapter 6

Dimuon and Dielectron Channel Combination

6.1 Introduction

A similar measurement of the ratio of inclusive $Z + b$-jet to Z+jet cross sections is also performed in the di-electron channel where the Z boson decays into a pair of electrons (instead of muons). The dielectron analysis is described in extensive detail in [86], but we will present a short description of event selection and the measurement of the ratio in this chapter. Finally, we will also discuss how these independent measurements are combined into a single measurement.

6.2 Electron Selection and Candidate Events

The dielectron analysis is based on a collider data sample corresponding to an integrated luminosity of 189 pb^{-1}. The data is collected using two different dielectron triggers and further skimmed for two reconstructed EM objects of transverse momenta larger than 15.0 GeV (2EMhighpt skim).

As we discussed in chapter 4, electrons are reconstructed via simple cone algorithms in the calorimeter with radius of 0.2 in $\eta - \phi$. The electromagnetic fraction for the initial candidates is required to be larger than 90 %. The isolation which is defined as $((E_{TOT}^{R<0.4} - E_{EM}^{R<0.2})/E_{EM}^{R<0.2})$ is required to be less than 0.15. The H-matrix χ^2, as defined in chapter 4, is required to be less than 20 for these EM object candidates. Finally the selected EM objects are required to pass the following set of kinematic cuts:

- $p_T > 15.0$ GeV
- $|\eta| < 2.5$

In order to reconstruct the Z candidates, at least one EM object is required to have a matching central track and the dielectron invariant mass is required to be between 80.0 and 100.0 GeV . This window is tighter than that used for the dimuon channel because the electron energy resolution is better than that of muons. Before any jet selection, we find 15,613 Z candidates in the dielectron channel with inclusive number of jets.

Despite the difference due to the electron selection in the dielectron channel analysis, the jet selection, taggability and b-tagging requirements are kept exactly same in the two analysis. The dielectron candidate invariant mass distributions for events with one or more taggable jets and with a b-tagged jet are shown in Fig. 6.1.

The transverse momentum of taggable jets as well as b-tagged jets can also be seen in Fig. 6.2 and Fig. 6.3, respectively. After the requirement of at least 1 taggable jet, the number of Z candidates reduces to 1658 events. With the b-tagging, the number of dielectron Z candidate events including at least one b-tagged jet is 27 events. Unlike the dimuon analysis where we observed a single event with two b-tagged jets, no event with more than one b-tagged jet is found

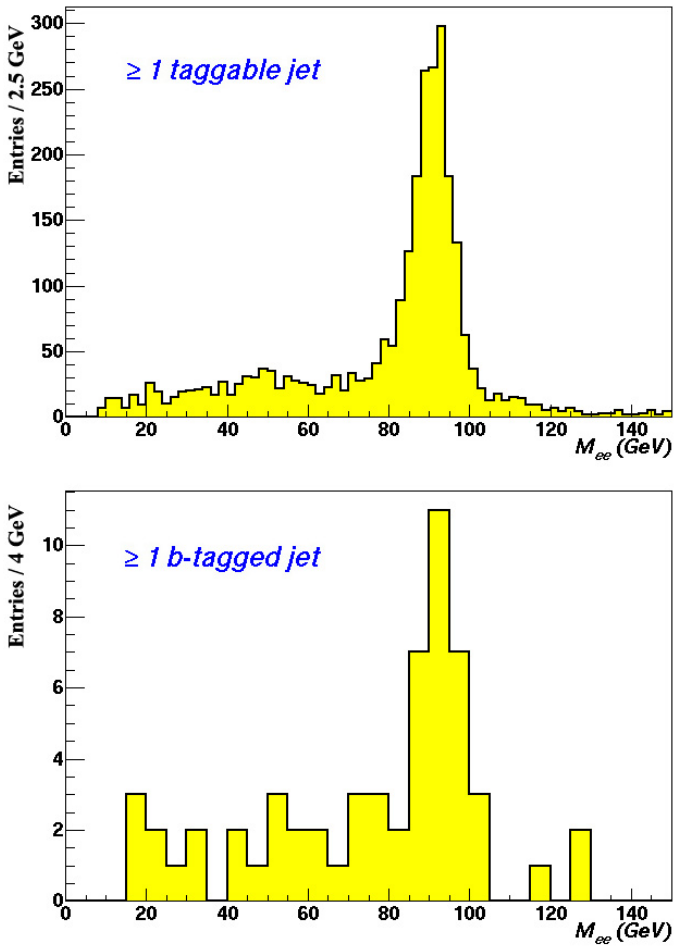

Figure 6.1: Dielectron invariant mass distribution in data, where at least one of the electrons is required to have a matching central track. In the upper plot, at least one taggable jet present in the event, whereas lower plot requires at least one b-tagged jet present in the event along with the dielectron candidate. Distributions shown with no cut on the invariant mass.

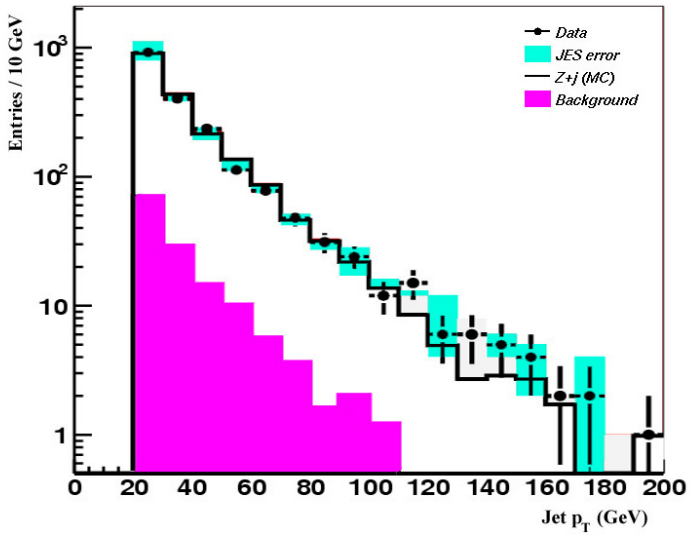

Figure 6.2: The comparison of taggable jet p_T in Z candidate events (bars) and expectation from $Z + j$ (black line) and the background (magenta-filled histogram). Background contribution includes the fake background where a jet fakes an electron as well as the non-resonant Drell-Yan continuum. In making the normalizations, MC jets are scaled by the data versus MC jet reconstruction efficiency difference.

among the 27 candidates.

6.3 Ratio of Cross-Sections

The non-Z background contribution to the candidate di-electron events is calculated in a different way from the dimuon channel. Instead of analytically finding the background contribution as in the dimuon channel, fits to the dielectron invariant mass distribution are used to extract this. The bands of invariant mass to either side of the Z mass window are fit with an exponential and the fit is extrapolated to the region of interest (80-100 GeV) to find the background contribution. With this method, there is no way of separating the two sources of the background, the multijet fake contribution and Drell-Yan continuum. The reason for differ-

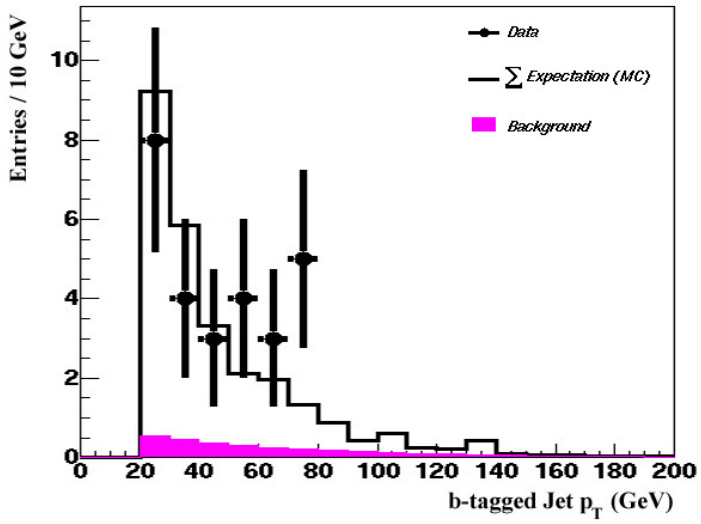

Figure 6.3: The comparison of b-tagged jet p_T in Z candidate events (bars) and total expectation from all sources contributing to the b-tagged jet final state (real b-jets as well as c-jets, light jets and background). The magenta fill shows the dielectron background which consists of the fake background where a jet fakes an electron as well as the non-resonant Drell-Yan continuum.

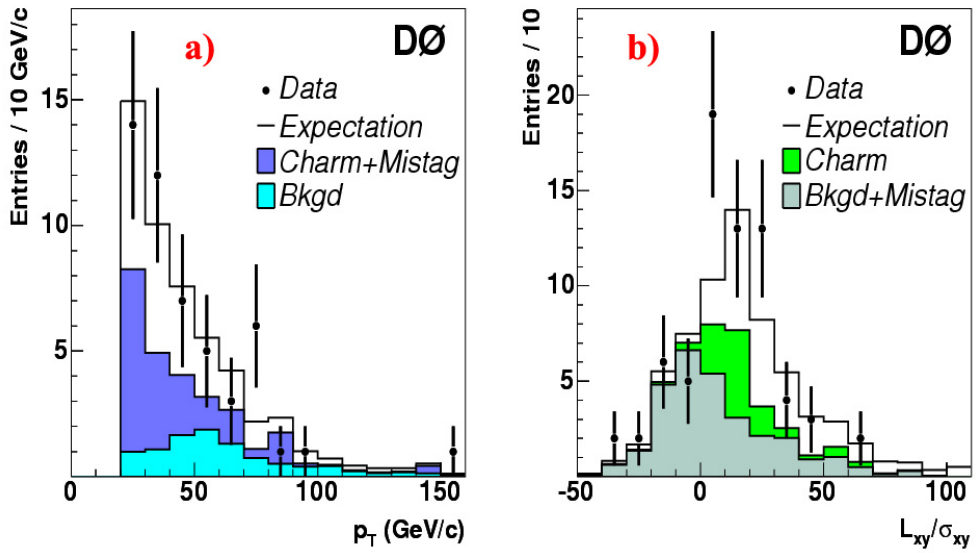

Figure 6.4: Dielectron and dimuon channels combined. Left plot (a) shows the transverse momentum distribution of the b-tagged jets whereas the plot on the right (b) shows the secondary vertex transverse decay length significance distribution without the cut on the same quantity (> 7) as normally done for the analysis. All error bars are statistical.

ent methods of background calculations employed in the dielectron and dimuon channels is related to the application of the isolation criteria in the two analyses. Isolation criteria is a part of the electron reconstruction and there is no way of using the isolation at the analysis stage forcing this particular way of measuring the background. Since isolation criteria are applied after the reconstruction stage, a similar restriction is not a problem for the dimuon channel. Consequently, this method yields a dielectron background of 4.7% within the invariant mass window.

After estimating the background before and after b-tagging, we solve the set of equations presented in the previous chapter. In the dielectron channel, the ratio of inclusive cross sections of Z+b-jet to Z+jet is found to be $2.34 \pm 0.66(\text{stat})^{+0.27}_{-0.28}(\text{syst})\%$.

6.4 Combination of the Two Channels

Having two experimental measurements for the same physical quantity, it is beneficial to combine the two results into a single measurement. Due to the small statistics in each of the separate channels, the statistical uncertainty is the major uncertainty in these measurements and combining the results help reduce this uncertainty. The two results are combined using a statistically weighted averaging scheme as shown in Eq. 6.1.

$$R_{comb} = \sqrt{\frac{N_{\mu\mu}}{N_{\mu\mu}+N_{ee}}} \cdot R_{\mu\mu} + \sqrt{\frac{N_{ee}}{N_{\mu\mu}+N_{ee}}} \cdot R_{ee} \tag{6.1}$$

where R represents the measurement of the ratio from each channel and $N_{\mu\mu}$ or N_{ee} stands for the number of Z+taggable jet events in dimuon and channels respectively. In the averaging process, all the systematic uncertainties are assumed to be fully correlated and summed linearly except the uncertainties related to the background estimation. Since the sources of backgrounds in muon and electron channels are different, the corresponding uncertainties are added in quadrature. The resulting measurement for the ratio of the inclusive $Z + b$-jet to Z+jet cross sections is found to be;

$$\frac{\sigma(Z+b)}{\sigma(Z+j)} = (2.11 \pm 0.41(\text{stat})^{+0.25}_{-0.22}(\text{syst})) \times 10^{-2} \tag{6.2}$$

Chapter 7

Outlook for $Z + b\bar{b}$ Cross-Section Measurement

7.1 Introduction

Most of physics analyses currently performed at DØ involve production modes with small signals compared to the large backgrounds from similar-signature physics channels. It is clear that the study of these signals should be carefully optimized to achieve the best combination of event yield while keeping the signal significance at optimum levels. The traditional methods used in main-stream analyses, therefore, might not always provide the most optimum selection of events.

An example of such rare signals is the $Z(\mu\bar{\mu}) + b\bar{b}$ production where two high momentum b-jets are produced via gluon splitting in association with a Z boson, as shown in Fig. 7.1. Study of this signal is very important for the understanding of QCD b-jet production with associated vector bosons. Another importance of this channel is that it is one of the major background processes to several proposed new physics signals like technicolor production as well as one of the Standard Model

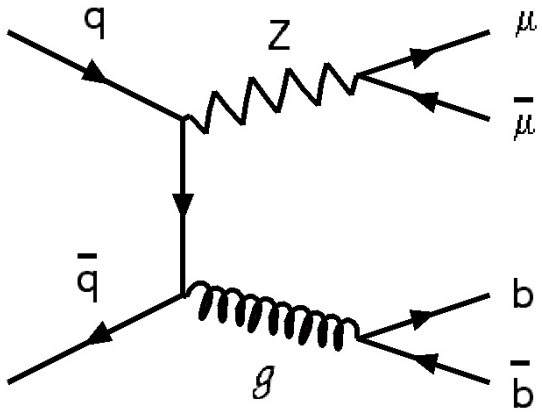

Figure 7.1: The Feynman diagram for $Z(\mu\bar{\mu})+b\bar{b}$ production at Tevatron where Z boson decays to a pair of leptons (muons in this case) and the gluon decays to a pair of b quarks.

(SM) Higgs boson production modes.

The theoretical calculations including next-to-leading (NLO) corrections tells us that the production cross-section for $Z(\ell\bar{\ell}) + b\bar{b}$ signal is expected to be about 0.5 pb for the kinematic region we are interested in. This translates to a small production probability such that with 300 pb^{-1} integrated luminosity, there are only about 150 of such events produced as a result of proton anti-proton collisions at the Tevatron. Due to several experimental factors like detector acceptance and inefficiencies at different levels of reconstruction, we do not observe all of these events produced in the collisions and lose a significant portion of signal events. The signal acceptance for this signature is about 1 % using current standard selection cuts and this gives an expectation of about 1.5 events for 300 pb^{-1} integrated luminosity.

One or two recorded events are certainly too few to make any quantitative or qualitative judgement about the production of $Z(\mu\bar{\mu}) + b\bar{b}$ events and more sophisticated methods should be employed to increase this low yield. With this

purpose in mind, we will demonstrate a basic optimization scheme of the analysis strategy to achieve a better level of signal event yields.

7.2 Optimization Methods and Preselection

We would like to perform the optimization first by summarizing the key observations that motivate this need. These are;

- The operating points for event selection should be optimized for the specific signal investigated.

  As we discussed before, the analysis strategy for the search of rare physics signals where one would like to collect as many events as possible is substantially different from cases where one wants to improve on signal purity and accomodate tighter event selection cuts.

- Traditional analysis strategies using square cuts[1] that apply selections on each physics object (tracks, jets, muons etc) in the event disregard the correlation between these objects and throw out a significant number of signal events from consideration.

  For signal topologies including more than one physics objects, the analysis could be loosened to allow for cases where one of the objects has high likelihood of passing the standard event selections and the other has lower chance of making through the possible event selection criteria. A schematic view of the possible cases is shown in Fig. 7.2.

[1] *Square cut* method refers to an analysis strategy where specific cuts on several parameters are made independently, delineating an n-dimensional rectilinear box in the parameter space where the events are selected.

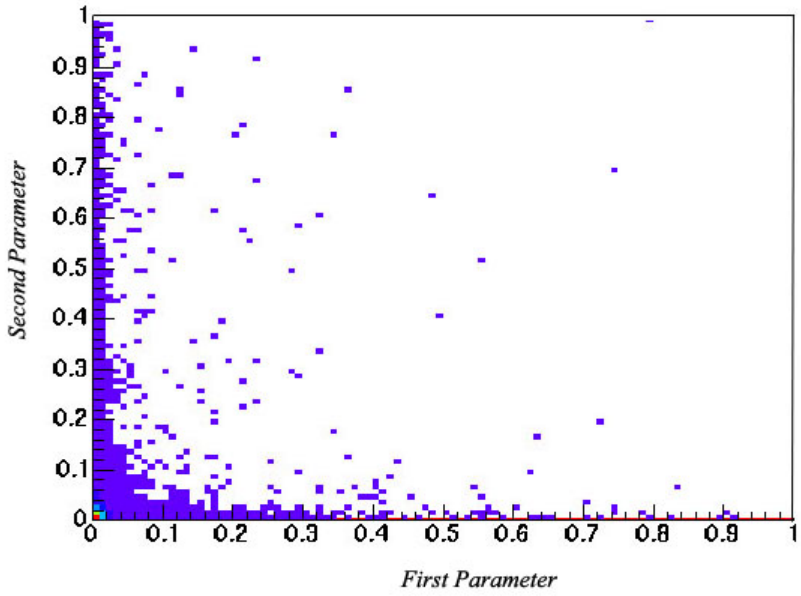

Figure 7.2: An example of a 2D feature space where the higher end of tails near both axes contain a significant fraction of the total sample. These tails would simply be ignored and substantial amount of data would be lost with a traditional square cut about the origin.

Along these lines, we will demonstrate an optimization scheme for the selection of $Z(\mu\bar{\mu}) + b\bar{b}$ events in this chapter. At the moment we treat the dimuon and two b-jet systems independently for simplicity but further optimization could be achieved if the $Z(\mu\bar{\mu}) + b\bar{b}$ system is considered fully.

For this study, we made use of several MC (shown in Table 7.1) and data samples to assess the effect of the optimization techniques. Data samples are shortly denoted as:

- 2MU_HIGHPT — An inclusive collection of events with at least two reconstructed LOOSE muons both of which are matched to central tracks. The central track transverse momentum for these muons are also required to be larger than 15.0 GeV . These events mostly consist of the Drell-Yan dimuons as well as the muons produced in the semileptonic decays of heavy quarks.

- MU_2TRACK — An inclusive collection of events with at least two reconstructed tracks of transverse momentum larger than 15.0 GeV and at least one of the selected tracks is required to match a reconstructed LOOSE muon.

- JET_TRIGGER — An inclusive collection of events firing the jet triggers signalling the presence of a calorimeter jet. Although there is a small contribution from $W +$jet and $Z +$jet sources, these events are mostly from QCD inclusive jet production. This original selection of inclusive jet events are further filtered with a requirement of at least two offline jets of transverse momentum 20.0 GeV and at least one central track matched LOOSE muon of transverse momentum above 15.0 GeV . This sample is used for the purpose of representing the background samples as described in the following sections.

Sample	MC Generator	Events	Cross-Section
$Z(\mu\bar{\mu}) + b\bar{b}$	ALPGEN +PYTHIA	100k	0.539 pb
$Z(\mu\bar{\mu}) + c\bar{c}$	ALPGEN +PYTHIA	40k	1.153 pb
$Z(\mu\bar{\mu}) + jj$	ALPGEN +PYTHIA	180k	29.10 pb

Table 7.1: Information on the MC samples used in this study.

7.2.1 Pre-Selection

Before studying possible optimization methods, we clean up the data samples using basic selection cuts that are widely used and necessary for similar analyses. The pre-selections on jets, muons and the reconstruction of the Z boson are outlined in the following subsections.

Jet Selection

For this analysis, we use calorimeter jets reconstructed with the cone algorithm of radius size 0.5 (chapter 4). The jet selection cuts are summarized below:

- Application of L1 confirmation
- $0.05 <$ EM-fraction < 0.95
- CH-fraction < 0.4
- n90 > 1
- Apply jet energy scale (JES) corrections (v05-01-00)
- $E_T \geq 20.0$ GeV
- $|\eta| \leq 2.5$

Prior to the application of b-tagging, selected calorimeter jets are required to be taggable as described in chapter 5. This condition is imposed on the calorimeter jet by matching it to the reconstructed track jets within a matching $\Delta R_{track-jet,jet}$ of 0.5. For b-tagging, we use the impact parameter b-tagging algorithm as described in chapter 4 and the taggable jets are assigned a probability describing the likelihood of being associated with the hard-scatter (primary) vertex as opposed to a displaced vertex. We do not yet apply a cut on this impact parameter probability of the jets but rather use it as an input for our optimization study.

Muon Selection

Muons are required to be at least LOOSE in quality (chapter 4) and be matched to central tracks with;

- $p_T^{central} > 15.0$ GeV
- $|\eta| < 2.0$

For making Z candidates, we require two selected muons with the following criteria;

- Opposite electric charge ie. $Q_{\mu_1} \neq Q_{\mu_2}$
- Opening angle in transverse plane: $\Delta\phi > 0.4$
- Invariant mass window: 65.0 GeV $< M_{\mu_1\mu_2} <$ 115.0 GeV

We investigated the preselection requirement of two central track matched, loose muons. As we mentioned in chapter 4, the central tracking system alone provides the necessary kinematic information for the reconstructed muons and we use the muon system for the identification of the central track as a muon. However, this muon system confirmation comes with the expense of the loss of

efficiency due to muon reconstruction and is even more pronounced for the muons pointing towards the bottom region of the muon detector (octants 5 and 6, $|\eta| < 1.6$) where the detector acceptance is lower as compared to other regions.

Given the problem presented above, we studied whether the Z boson candidates can be reconstructed with a combination of two tracks, only one of which is required to be identified as a muon. For this purpose, we used the MU_2TRACK data sample and required two central tracks of transverse momentum larger than 15.0 GeV and pseudo-rapidity within 2.0. At least one of the tracks is required to match a reconstructed loose muon (instead of usual requirement of both tracks matching muons). Both tracks are required to be isolated with respect to the closest jet found in the event as specified by a cut on track $p_T^{rel} > 10.0$ GeV as used in previous chapter (tracks with $p_T^{rel} > 10.0$ GeV are accepted as isolated).

Fig. 7.3 shows the invariant mass of the two track combinations where one and only one of the tracks is matched to a reconstructed muon. In order to observe the effect of the efficiency loss due to the second muon reconstruction, we focused our selection to the bottom region of the muon detector where we required the unmatched track to point towards this area (muon system octants 5 and 6, $|\eta| < 1.6$). We observe that the signal contribution for these type of muon and track combinations (198 events) is very small as compared to the added level of background contamination (more than 20 times the added signal) which is believed to be mostly due to events with a real single muon and additional high-p_T tracks from the jets. We conclude that the inclusion of events with one muon and an isolated track is not desirable.

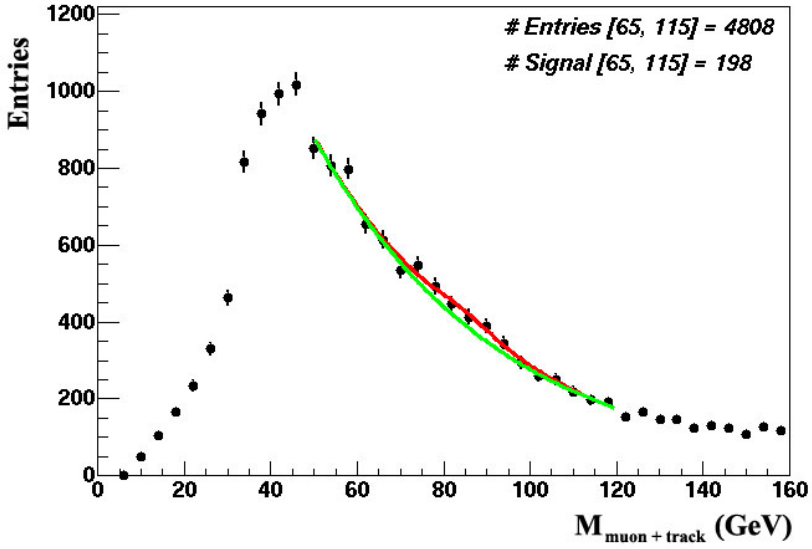

Figure 7.3: The invariant mass distribution of the two tracks out of which only one of them is matched to a reconstructed loose muon. Furthermore, the unmatched track is required to be pointing towards the bottom of the DØ detector (octants 5 and 6) where muon detector acceptance is somewhat lower with respect to the other regions.

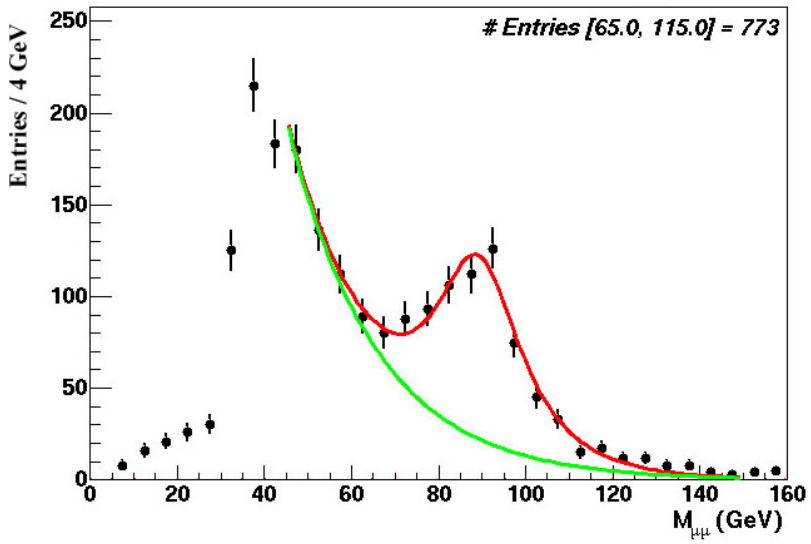

Figure 7.4: The dimuon invariant mass distribution in data with no isolation cut applied on the muons. The red and green lines show the fit to a combination of functions describing the Z resonance and the continuum.

7.3 Dimuon Selection Optimization

There are, in general, two major background processes to Z boson dimuon decays: (1) the Drell-Yan production of the dimuon pairs, and (2) the multijet production like $b\bar{b}$ where two muons are produced due to semileptonic decays of B hadrons. Unlike the Z resonance, these two major backgrounds contribute to the continuum in the dimuon invariant mass distribution as seen in Fig. 7.4. Fig. 7.4 is obtained from the 2MU_HIGHPT data sample with the requirement of two track matched, loose muons and two taggable jets in the events.

One of the best ways to reduce the background to real Z dimuons is to reduce the multijet (QCD) contribution inside the peak region [65, 115] GeV . The most apparent characteristic of the QCD dimuon events is the isolation of the muons since most of such muons are found near or inside the jets resulting in the large

amount of calorimeter & track activity nearby them.

Before proceeding further, we analyze some fundamental isolation variables in order to understand their power to discriminate real Z dimuons from QCD dimuon events and select some of the most significant of these variables in our optimization scheme.

We consider the following isolation variables:

- ΔR : Separation of the muon and the nearest good calorimeter jet in η-ϕ space
- p_T^{rel} : The transverse component of the muon momentum with respect to common muon and nearest jet axis:

$$p_T^{rel} = \frac{|\vec{p}_\mu \times (\vec{p}_\mu + \vec{p}_{jet})|}{|(\vec{p}_\mu + \vec{p}_{jet})|} \tag{7.1}$$

- **TrkSum**: Sum of all track transverse momenta inside a cone of 0.5 around the muon:

$$\text{TrkSum} = \sum_{\Delta R(track,\mu)<0.5} p_T^{track} \tag{7.2}$$

- **Halo**: Total transverse energy deposition in calorimeter inside a cone of 0.4 around the muon subtracted by the same energy deposition inside a cone of 0.1 about the muon:

$$\text{Halo} = \sum_{dr<0.4}^{N_{cell}} E_T^{cell} - \sum_{dr<0.1}^{N_{cell}} E_T^{cell} \tag{7.3}$$

- **Momentum Scaled Variables**: p_T^{rel} , TrkSum and Halo variables are each divided by the muon momentum.
- **Fisher Discriminant**: A Fisher discriminant constructed from the TrkSum, Halo and muon momentum ($|\vec{p}_\mu|$) variables. Given in the form of a

linear transformation, the Fisher discriminant gives the best projection in the parameter space for which the signal and background variables are best separated from each. Eq. 7.4 shows the form of such a projection where $\mathbf{m_i}$ (S, signal or B, background) is the vector of means for the data samples in the variable space and $\mathbf{C_w}$ is the sum of the covariance matrices for each class of data [89]. Vector x represents the data point in the original variable space and y represents the projection of y in the transformed space.

$$\mathbf{w} \propto \mathbf{C_w^{-1}} (\mathbf{m_S} - \mathbf{m_B}) \tag{7.4}$$

$$\mathbf{y(w)} \equiv \mathbf{w^T x} \tag{7.5}$$

The performance of these discriminants in background and signal muons are shown in Fig. 7.5 (the signal efficiency and background rate are defined per single muon) where background muons are obtained from dijet events in JET_TRIGGER data and signal muons are obtained from $Z(\mu\bar{\mu}) + b\bar{b}$ MC sample. For the Fisher discriminant performance, we divided the signal and background samples into two same size subsets, one for training purposes and the other for measuring the performance.

We see from Fig. 7.5 that the isolation variables which provide the best discrimination between background and signal events are the TrkSum and Halo variables as calculated according to the Eq. 7.2 and Eq. 7.3 respectively. Fig. 7.5 also shows the multivariate discriminant constructed using the Fisher method and this construction does not seem to add to the individual discrimination strength of the two most powerful isolation variables.

In order to understand the correlation of these isolation variables and the momentum of the muon for signal and background muons, we scale some of the mentioned isolation variables by the muon momentum as shown in Fig. 7.6. We

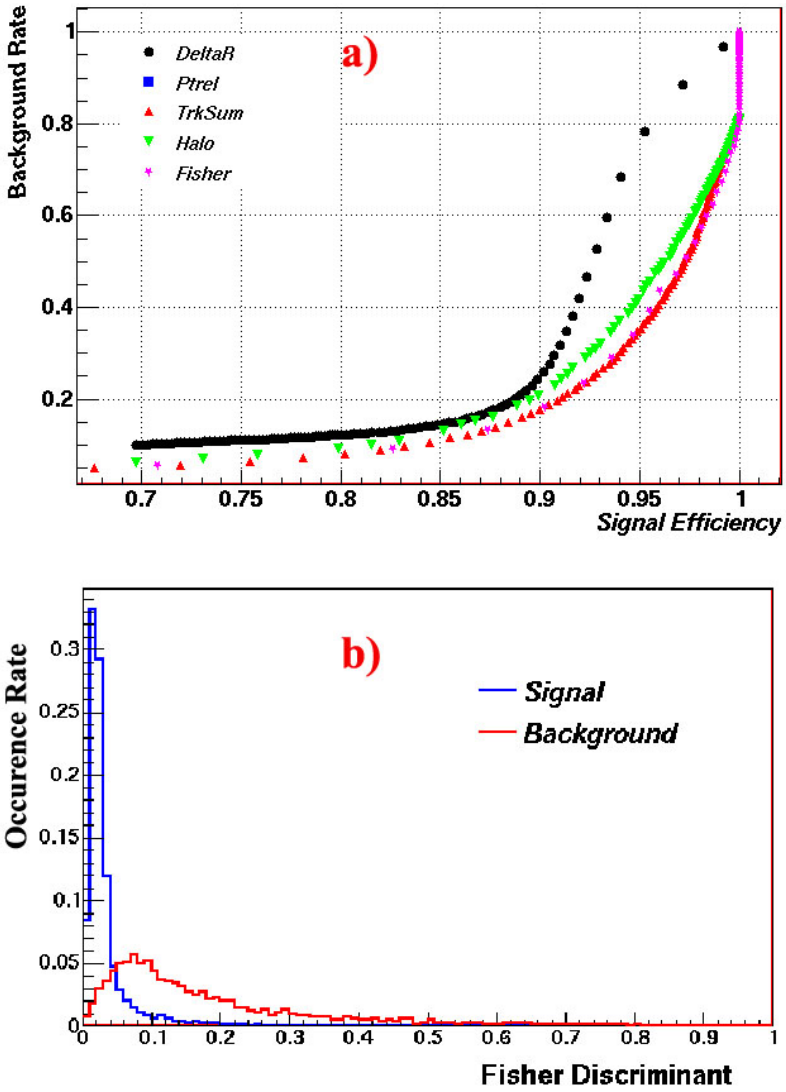

Figure 7.5: The single muon performance of some isolation discriminants (a) in background and signal samples. The lower plot (b) shows the Fisher likelihood discriminant constructed from the combination of the other four isolation variables (ΔR , p_T^{rel} , TrkSum and Halo) for signal and background muons.

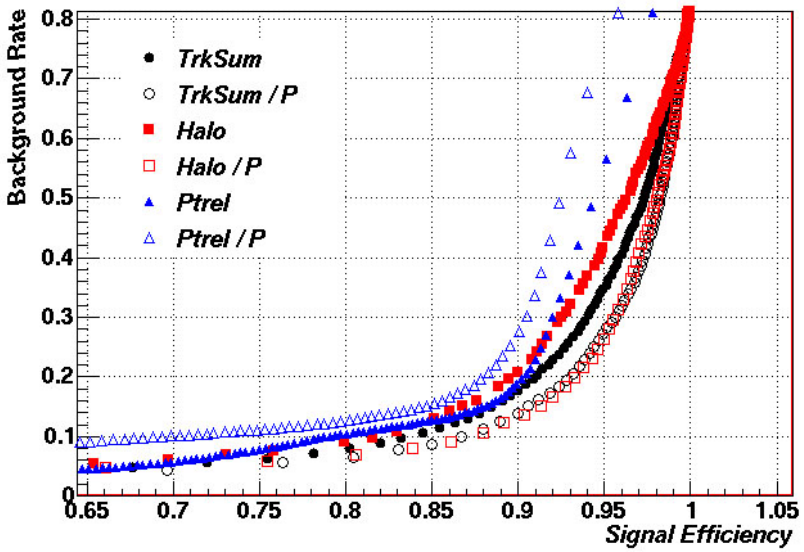

Figure 7.6: The single muon performance of isolation discriminants in background and signal samples compared to the muon momentum scaled versions of these discriminants. Filled markers represent the original isolation variable whereas the unfilled markers represent the same isolation variable scaled (divided) by the momentum of the muon. The signal and background distributions are normalized to an area of 1.

compare the performance of the unscaled isolation variables to their scaled versions and observe that the discrimination characteristic of the two most powerful isolation variables are enhanced when divided by the muon momentum.

It is clear that the Halo and TrkSum variables, when combined with the momentum of the muon, provide the best signal efficiency for lower background rates. Since both the Halo and TrkSum variables are behaving in a similar way (larger for background, smaller for signal muons), we combine the effect of these two isolation discriminants in a new isolation discriminant, f_{iso} as defined in Eq. 7.6. The result of the individual scaled Halo and TrkSum variables as compared to the sum of the two is shown in Fig. 7.7.

$$f_{iso} = \frac{\left[\sum_{dr<0.4}^{N_{cell}} E_T - \sum_{dr<0.1}^{N_{cell}} E_T\right] + \sum_{dr<0.5}^{N_{track}} p_T}{P_\mu} \tag{7.6}$$

Fig. 7.7 shows us that the combined isolation discriminant (f_{iso}) performs consistently with our expectation and enhances the performance of individual discriminants. Furthermore, the Fisher discriminant, finding the best linear combination among the Halo, TrkSum and muon momentum variables, is observed to be weaker than our intuitive construction, f_{iso}.

Our study on single muons showed that the combined isolation discriminant provides the best performance for the discrimination of signal and background muons. Following this observation, we can also work on the optimization of the isolation criteria for the dimuon system but we find it more natural to describe the isolation of the muon with a probability rather than the actual physical variable (f_{iso}). As we will observe later, working with a probability provides the flexibility necessary for performing a variety of optimization techniques.

We construct the isolation probability solely from the background sample which we extracted from the jet-trigger data as in Eq. 7.7. This way the probability density distribution, shown in Fig. 7.8, can fully be extracted from data alone. This would enable the isolation probability to be independent of any simulation but the definition of such a probability would be the "isolation probability of the muon to be a background-like muon". However, this can simply be inverted to describe the likelihood of being a signal-like (Z -like) muon.

$$P_{iso}(f_0) = \frac{\int_{f_0}^{\infty} f_{iso}(\mu) df}{\int_{0}^{\infty} f_{iso}(\mu) df} \tag{7.7}$$

The behaviour of the constructed isolation probability in signal and background

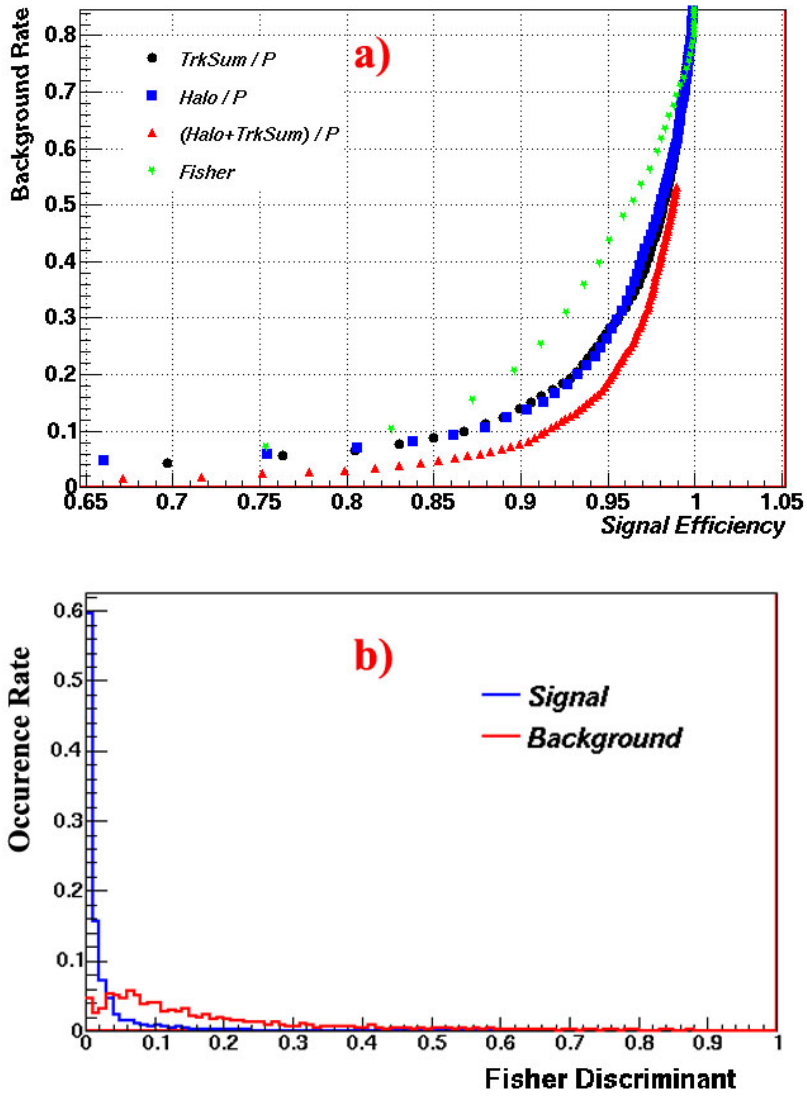

Figure 7.7: The single muon performance of scaled isolation discriminants (a) in background and signal samples. The lower plot (b) shows the Fisher likelihood discriminant constructed from the combination of Halo, TrkSum and muon momentum variables to search for other ways of combining these variables (other than adding and scaling with muon momentum. The signal and background distributions are normalized to an area of 1.

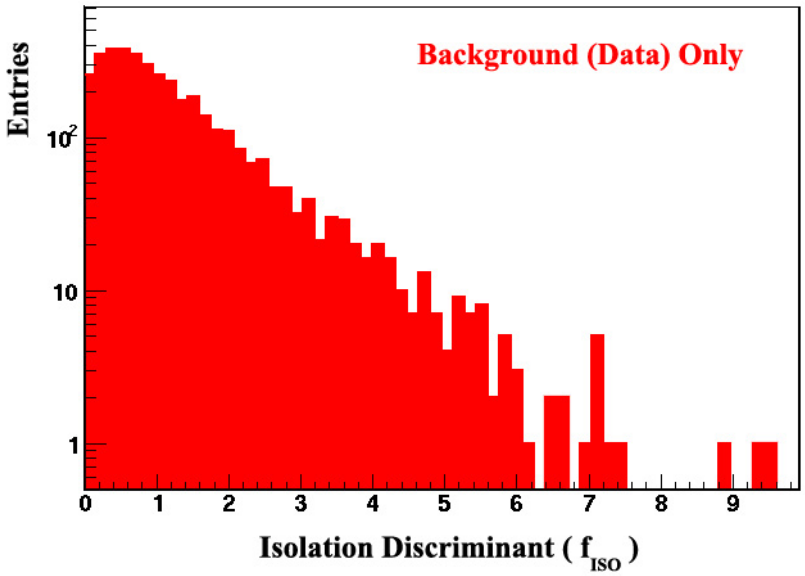

Figure 7.8: The isolation discriminant, ie. f_{iso} defined in Eq. 7.6, as obtained from single muons in background data sample.

muons is shown in Fig. 7.9. The background sample used in this plot is independent of the sample for which the probabilities are reconstructed since we divided the background sample into training and test samples for this purpose. We observe that the muons in the background data sample show a flat probability between 0 and 1 as expected from the construction of the probability. We also realize that signal-like muons accumulate around $P_{iso} = 0$, since this probability describes the likelihood of being a background-like muon. Fig. 7.9 convinces us that the construction of the probability works just as expected.

Our next step is to combine the isolation probabilities of the two individual muons in the signal and background dimuon events. However, as we discussed before, the background sample extracted from jet-trigger data is selected with only 1 or more muon requirement and most of the events in this sample indeed are exclusively one-muon events. In order to overcome this problem, we employ a

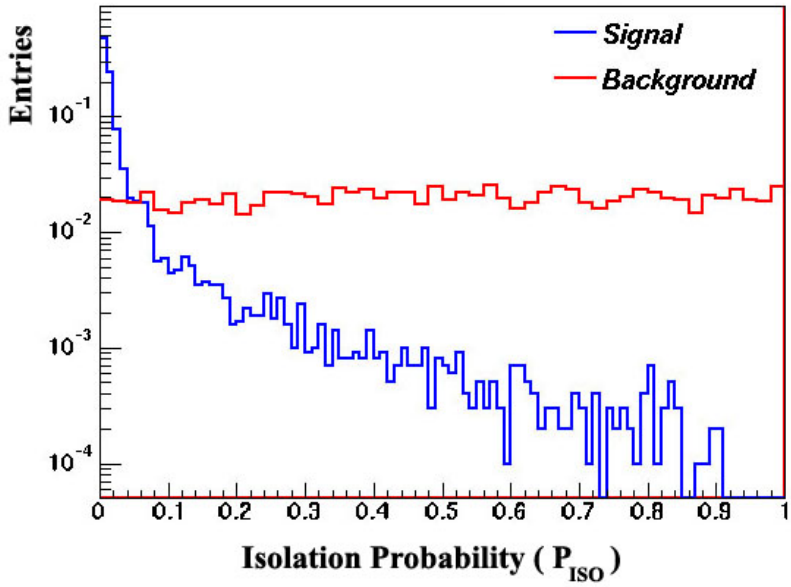

Figure 7.9: The isolation probability, ie. P_{iso} defined in Eq. 7.7, of background and signal muons.

simple scheme in which we perform a fundamental simulation technique.

Using the discriminant distribution, f_{iso}, of muons in background events, we generate a second muon in the event with an isolation discriminant equal to a random value generated from f_{iso} distribution. We show the discriminant values of the real and generated muons in the background events in Fig. 7.10. The random generation of a second muon in the event ignores the possible correlations between the two muons which might be appearing in the real collider data. However, we will demonstrate later that our approximation with this dimuon generation scheme is a good approach to mimicking the real background dimuon events.

From Fig. 7.11, we observe the correlations between the two isolation probabilities of the muons in the Z events. The signal dimuon events appear to have occupation densities consistent with hyperbolic contours, described by the relation $P_1 \times P_2 = const.$

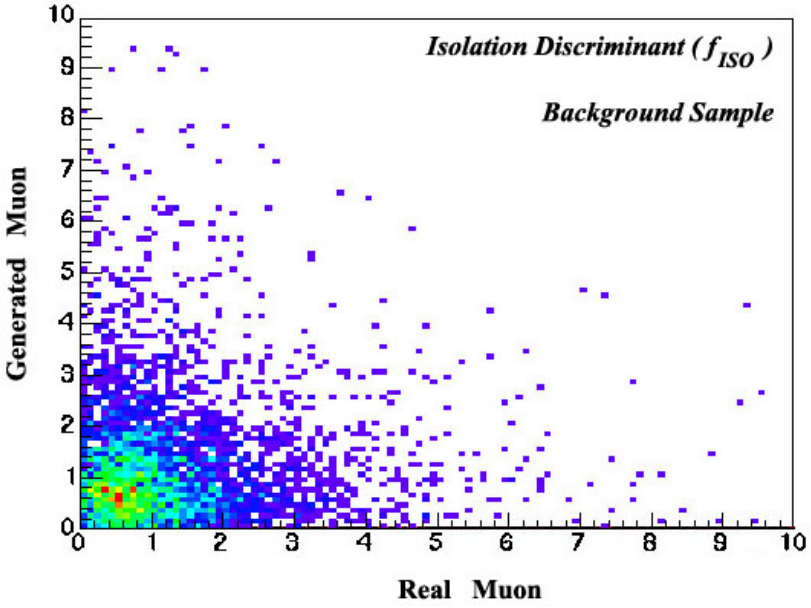

Figure 7.10: The isolation discriminant, ie. f_{iso} defined in Eq. 7.6, for real background muons and generated muons. The projection of this plot on either of the axes produces Fig. 7.8.

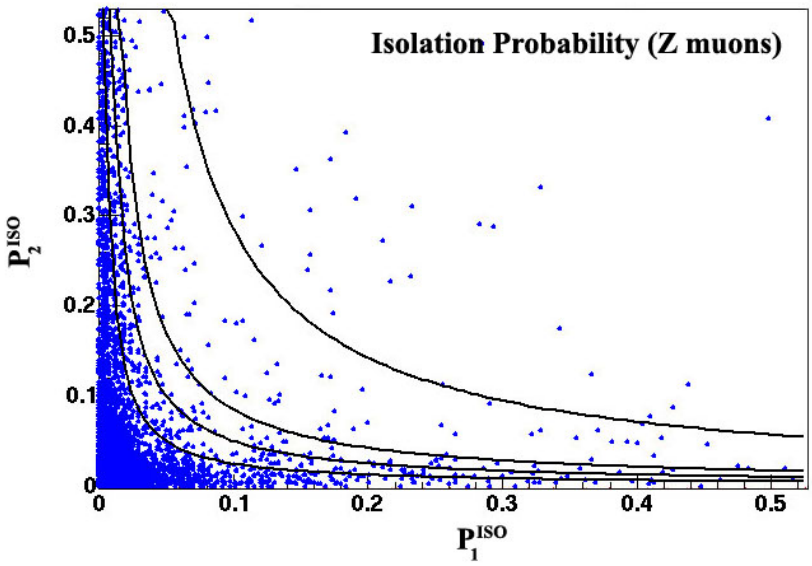

Figure 7.11: The 2D isolation probability, ie. P_{iso} defined in Eq. 7.7, distribution in signal dimuon events (x and y axis show the leading and next-to-leading muons, respectively). The distribution suggests that hyperbolic contours give a good description of the Z dimuon events and border the area of probability accumulation in these events.

We combine the individual muon isolation probabilities to create a dimuon probability consistent with the hyperbolic contours in Fig. 7.11. We also compare the performances of these hyperbolic cuts to more traditional square cut analysis where a cut is applied to both muons (ie. $(P_1 < cut)$ AND $(P_2 < cut)$) and an OR-ing scheme where we only apply a cut on the most isolated (smallest probability) muon (ie. $P_{min} < cut$).

The performances of these different strategies can be compared in the signal dimuon efficiency versus background dimuon efficiency plot in Fig. 7.12 . The performances of these different event probability construction models indeed demonstrate that the hyperbolic contours provide the best description of the signal probability phase space. The performance gain as evidenced by Fig. 7.12 is quite striking especially in the high efficiency regions (near 95% signal efficiency) where the hyperbolic construction of event probability achieves about 6 times lower background levels at same signal efficiencies. This can be translated to a gain of almost 2.5 in the significance of the dimuon signal with respect to the QCD background.

In addition to trying pre-constructed strategies which proved to be very efficient, we also tried a "random grid search" method which enables the selection cuts to attain flexible values across the 2D phase space [90]. We tested this strategy on a grid of 5000 network nodes and the performance of this method can be seen in Fig. 7.13. The efficiency vs. background rate plot shows us that there are some efficient operating points which provide as low as 8% background rate at 95% signal efficiency. Although being much better than the traditional square cut approach, the event probability we constructed proved to be a much better choice to discriminate the signal from background.

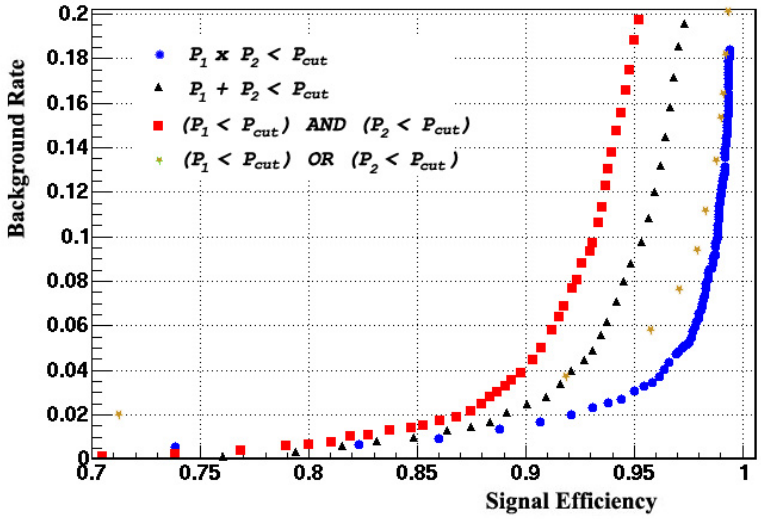

Figure 7.12: The dimuon (event) efficiency of some event probability constructing strategies in background and signal samples.

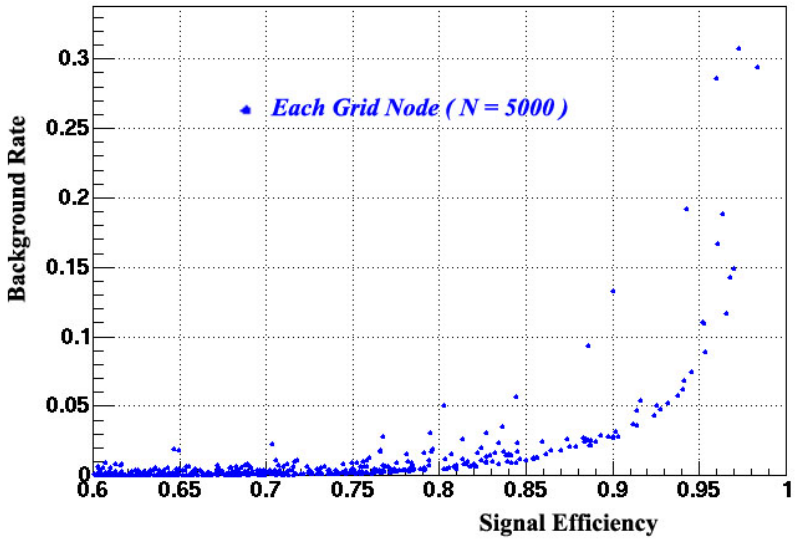

Figure 7.13: The dimuon (event) efficiency of in background and signal samples obtained via a 5000 network node random grid search.

7.3.1 Efficiency Measurement in Data

We have demonstrated the performance of the dimuon isolation probability on Monte Carlo signal ($Z(\mu\bar{\mu}) + jj$) events as well as jet trigger data which we used as the background sample. We have two additional tasks to confirm the validity of our studies. First of all, we need to confirm that artificially generating the second muon in the background sample correctly simulates the actual background events and does not introduce any bias. We also need to measure the signal dimuon isolation efficiency directly from the Z events in the data.

In order to study the muons in the background events, we use the 2MU_HIGHPT data sample and select two muons in the event. The background-like dimuons are distinguished from real Z dimuons by requiring that the isolation probability of the two muons should be greater than 0.005, this sample is also called *anti-isolated*. Most of these dimuon candidates are indeed background events as seen from the dimuon invariant mass distribution in Fig. 7.14.

The isolation probability distribution for these anti-isolated dimuons is also given in Fig. 7.15 overlayed with the dimuon probability where we generated the second muon in the event from a flat probability. Fig. 7.15 shows that our simple simulation scheme appear to describe the probability distribution of the real background dimuon events well within the available statistics.

Given our ability to describe the real background dimuons in data, we use the generated dimuon probability distribution to calculate the isolation efficiency for background dimuon events (with two additional jets). For signal efficiency, we employ an invariant mass fitting procedure where we fit the invariant mass distribution of dimuons before and after the isolation requirement and extract the number of real Z candidates from the fits as shown in Fig. 7.16. The results are shown in Table 7.2.

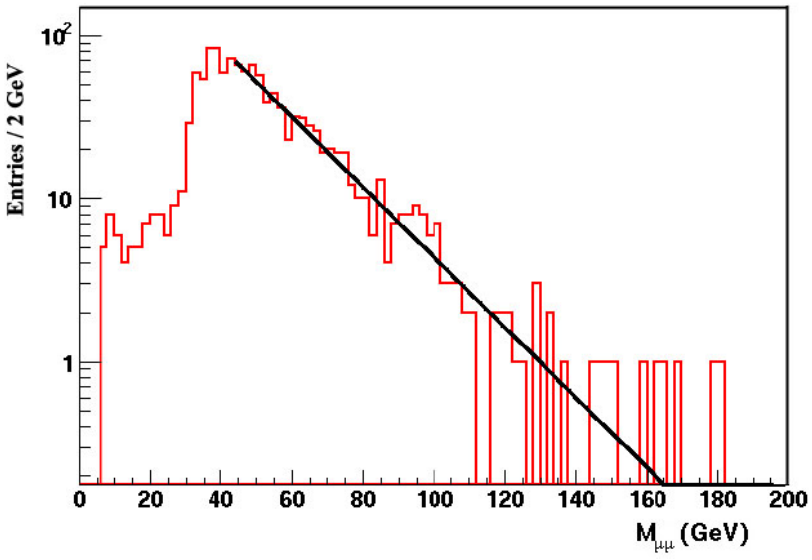

Figure 7.14: The invariant mass of the two muons in the anti-isolated ($P_{iso} \geq 0.005$) data sample.

Isolation	Signal Efficiency	Background Rate
$P_{iso} < 0.001$	78.7 %	0.79 %
$P_{iso} < 0.003$	89.0 %	2.07 %
$P_{iso} < 0.005$	92.1 %	3.17 %
$P_{iso} < 0.010$	95.7 %	5.55 %
$P_{iso} < 0.015$	97.6 %	7.74 %
$P_{iso} < 0.025$	98.2 %	11.62 %

Table 7.2: The signal and background dimuon efficiencies for several dimuon isolation probability requirements. Consult the text for an explanation of the calculation method.

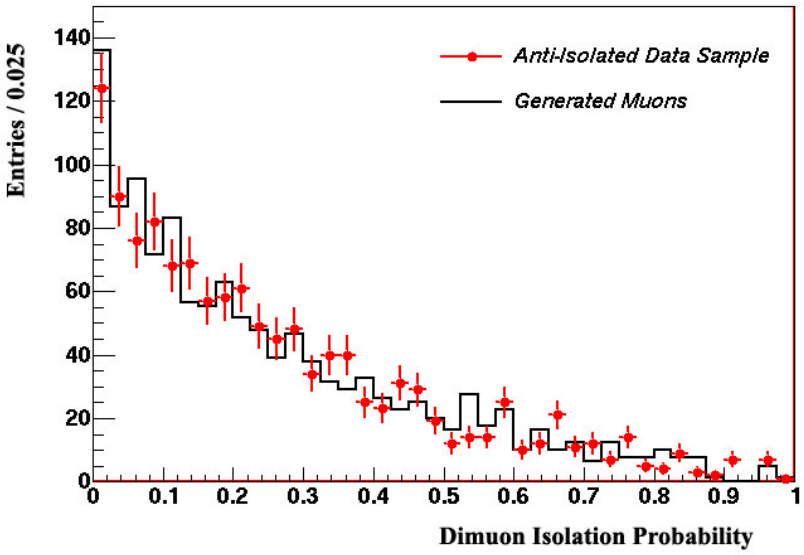

Figure 7.15: The isolation probability of the two muons in the anti-isolated ($P_{iso} \geq 0.005$) data sample (error bars) is shown overlayed with the probability of the dimuons extracted from the JET_TRIGGER data where the second muon is artificially generated in the event.

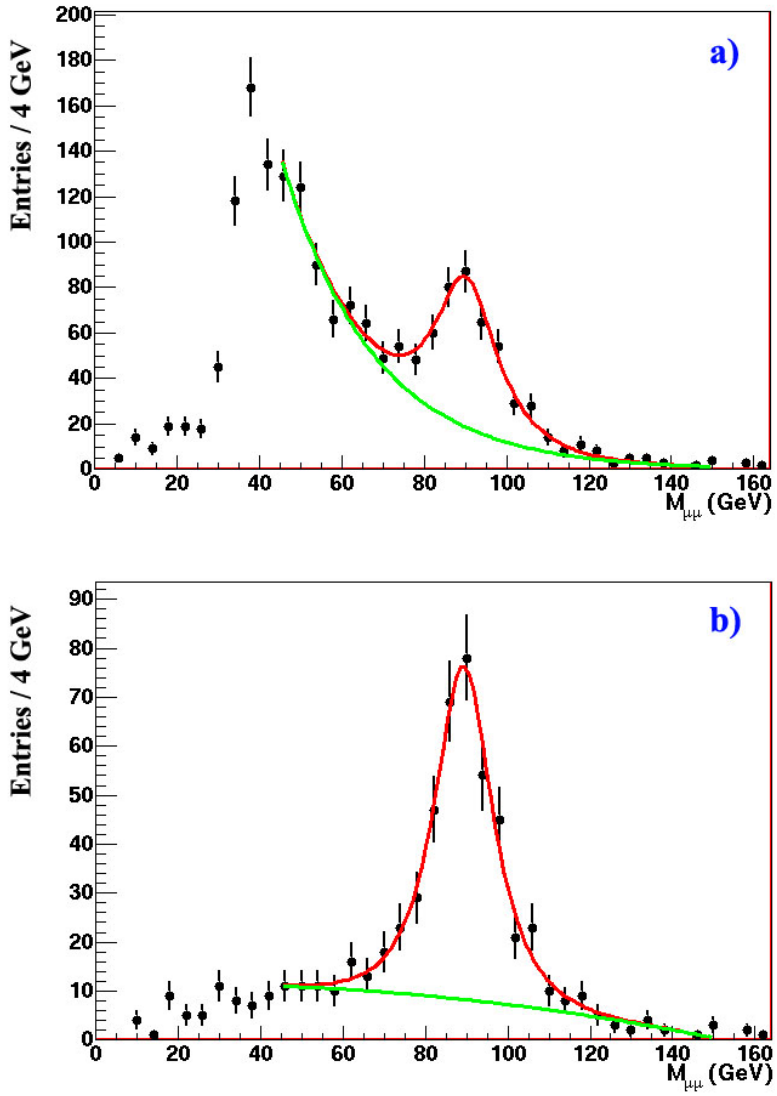

Figure 7.16: The calculation of the signal dimuon isolation requirement efficiency (shown for $P_{iso} \geq 0.025$). Upper plot (a) shows the dimuon invariant mass distribution with no isolation requirement and the lower plot shows the same distribution after a cut on the isolation probability. The number of real Z candidates are extracted from the peak within the mass window [65, 115] GeV .

7.4 b-jet Selection Optimization

Through the optimization studies, we observed that applying the selection cuts on the dimuon system (on the dimuon isolation event probability) provided better performance than a traditional square cut analysis. The same strategy can be extended to the two b-jet system where we again have two similar objects in the final event signature. However, in this case, our optimizations will be performed on the b-tagging probability rather than the isolation.

We perform the optimization through a two-step approach where we first determine the level of background which provides us the best signal significance and after determining this, we move on to studying of the possible enhancements that could increase the signal efficiency further while keeping the background rate at this optimum level.

The production of real $Z + b\bar{b}$ events at the current DØ data is very low and hence we perform these optimizations on simulated (MC) signal and background data. We assumed some general dimuon trigger efficiencies for selecting Z 's and applied event selection and b-tagging algoritms on the jets in these MC events. We take into account the differences in b-tagging in MC and real data by using a general scale factor (SF) of 80% to bring down the MC efficiencies to more realistic figures [79]. Tables 7.3 through 7.5 summarize the efficiencies and cross-sections used and obtained in this study. As expected, the Z selection performance does not show any significant variations between these samples. Small discrepancy observed in the Z selection efficiencies shown in Table 7.3 and Table 7.5 could be attributed to the fact that different underlying quark masses in these samples effect the jet kinematics and topology which indirectly effects the isolation condition imposed on the muons from the Z .

The expectation from QCD background for faking real Z dimuons is extracted from real $\mu\bar{\mu}$+jj events in data and found to be about 2.6 events in about 150 pb^{-1}

Information	$Z(\mu\bar{\mu}) + b\bar{b}$		
Cross-Section	0.539 pb		
Trigger Efficiency	76.50 %		
Selection	**Events**	**Efficiency**	**Events/ 150 pb^{-1}**
Events (before trigger)	126143.8	100.00 %	80.85
$\#Z$	40018	31.72 %	25.65
$\#Z + \geq 2$ jets	8899	7.05 %	5.70
$\#Z + \geq 2$ taggable jets	7654	6.07 %	4.91

Table 7.3: Basic information and the pre-selection efficiencies used for $Z(\mu\bar{\mu}) + b\bar{b}$ MC.

Information	$Z(\mu\bar{\mu}) + c\bar{c}$		
Cross-Section	1.153 pb		
Trigger Efficiency	76.50 %		
Selection	**Events**	**Efficiency**	**Events/150 pb^{-1}**
Events (before trigger)	130718.9	100.00 %	172.91
$\#Z$	41469.4	31.72 %	54.86
$\#Z + \geq 2$ jets	9221.8	7.05 %	12.20
$\#Z + \geq 2$ taggable jets	7931.6	6.07 %	10.49

Table 7.4: Basic information and the pre-selection efficiencies used for $Z(\mu\bar{\mu}) + c\bar{c}$ MC.

Information	$Z(\mu\bar{\mu}) + jj$		
Cross-Section	29.10 pb		
Trigger Efficiency	76.50 %		
Selection	**Events**	**Efficiency**	**Events/150 pb^{-1}**
Events (before trigger)	213160.8	100.00 %	4365.00
$\#Z$	61677	28.93 %	1262.99
$\#Z + \geq 2$ jets	12601	5.91 %	258.04
$\#Z + \geq 2$ taggable jets	10339	4.85 %	211.72

Table 7.5: Basic information and the pre-selection efficiencies used for $Z(\mu\bar{\mu}) + jj$ MC.

(see chapter 5 for details on the method). This specific background is treated as $b\bar{b}$ and the jets are weighted with corresponding b-tagging efficiencies. We know that the composition of this background is not purely $b\bar{b}$ but could be treated as such for the most conservative estimate.

The b and c-jet tagging efficiencies as a function of mistag rage (fake rate or light quark/gluon jet tagging rate) with impact parameter b-tagging algorithm is shown in Fig. 7.17 with the data/MC scale factor included in the efficiencies.

General DØ procedures for the identification of b-jets operate at levels to allow 1.0% (LOOSE), 0.5% (MEDIUM) and 0.25 % (TIGHT) of mistagged jets. In order to understand if these operating points are suitable for $Z + b\bar{b}$ analyses or to find the optimum operating point, we vary the tagging cuts along the b-jet and c-jet tagging efficiency curves shown in Fig. 7.17 and look at a reasonable figure of merit to compare different operating points. For the choice of a figure-of-merit in this analysis, we use the signal significance of $Z + b\bar{b}$ in 150 pb^{-1} data, ie. $S/\sqrt{S+B}$.

In Fig. 7.18, we show the different b-tagging operating points in a graph of signal significance versus mistag rate in 150 pb^{-1}. It is clear from the figure that

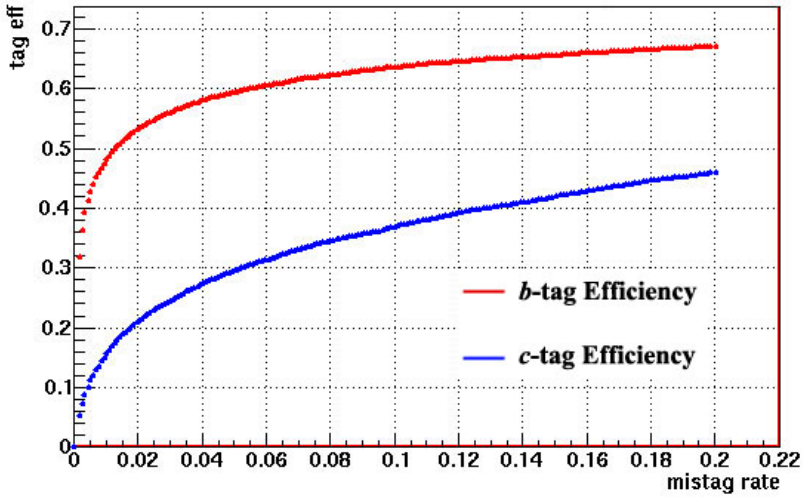

Figure 7.17: b-jet (red curve) and c-jet (blue curve) tagging efficiencies as a function of mistag (light jet tagging) rate obtained with the impact parameter b-tagging method.

the significance does not reach its optimum level with current b-tagging operating points ie. LOOSE etc. For $Z+b\bar{b}$ signal, the optimum signal significance is obtained at a much looser mistag rate of 3.6%. This finding is crucial for $Z+b\bar{b}$ analysis since the increase in efficiencies will provide us larger data sets to work while keeping the signal significance at maximum.

This simple exercise clearly shows that the currently utilized set of operating points are too tight for $Z + b\bar{b}$ analysis and both the event yield and signal significance benefit from loosening the mistag rate and the efficiencies.

The number of expected (signal, background and total) events as a function of the mistag rate are also derived and shown in Fig. 7.19 along with actual observations from 150 pb^{-1} collider data. Our first observation is that the optimum operating point which we determined to be about 3.6% mistag rate gives us an event yield of about 3.5 events in 150 pb^{-1} integrated luminosity as compared to about 2 events that the current loosest operating point achieves. The increase is

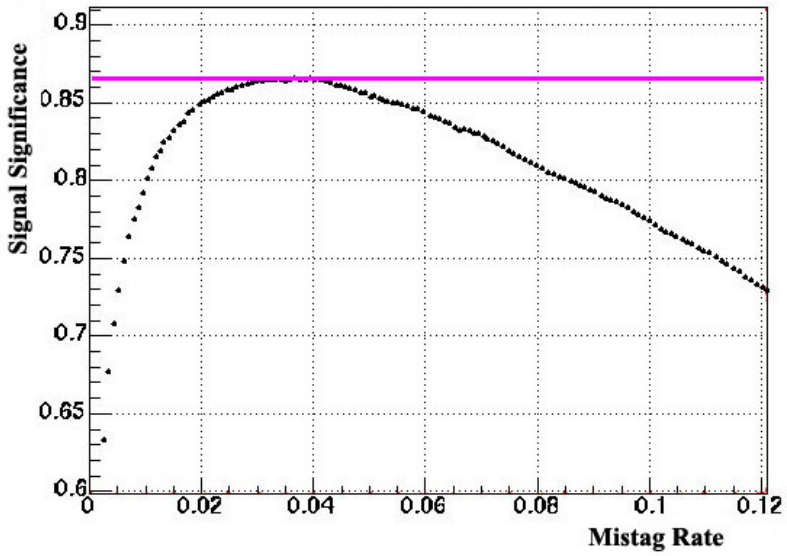

Figure 7.18: Signal significance, ie. $S/\sqrt{S+B}$, versus mistag rate for different b-tagging operating points. The horizontal line is shown to guide the eye for finding the maximum of the curve (dots). The maximum significance for $Z + b\bar{b}$ signal is obtained at a mistag rate of about 3.6%.

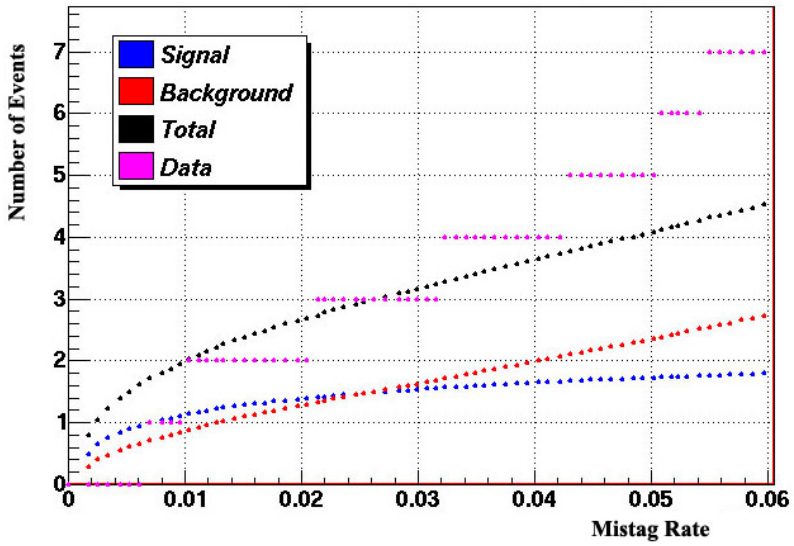

Figure 7.19: Number of expected signal (only b-jets), background (sum of c-jet, light jet and QCD contributions) and total events as a function of mistag rate are shown overlayed with observations from 150 pb^{-1} real data.

an equivalent of adding 75% more data into the analysis and keeping the signal significance at maximum.

Another observation from Fig. 7.19 is that given the low statistics in data events, we see that our modelling has a good consistency with actual data up to mistag rates of about 5%. The observations from data start to overshoot our expectations but we believe this is partially a result of being over-conservative in the MC/data b-tagging efficiency scale factor estimation. We used a global down-scale factor of 80 % across all operating points but we know that this scale factor approaches 100 % as the mistag rate increases.

After having found the level of mistag rate that we can allow for achieving the optimum performance from the b-tagging method, we can turn our attention to increasing the signal efficiency with respect to the square cut analysis. The most natural way to study this will be to follow the path we have described in the dimuon

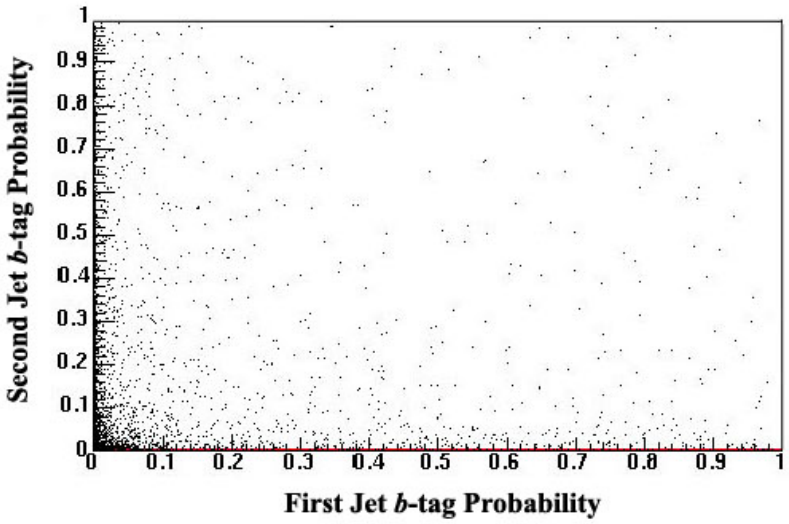

Figure 7.20: The impact parameter b-tag probability of the two leading taggable jets in the signal ($Z + b\bar{b}$) sample, x-axis shows the leading jet while y-axis showing the next-to-leading jet in the event. Since the probability describes the likelihood of being associated with the primary vertex, the probabilities for b-jets are close to P=0 .

optimization section since we observed substantial increases in the efficiencies when the probabilities of the two similar objects in the event are combined.

The impact parameter probability of the leading two taggable jets in the signal sample are shown in Fig. 7.20 and this 2-dimensional space reminds us the corresponding space of the Z dimuon system with the proability contours bordered by hyperbolic contours.

Combining the jet IP probabilities according to hyperbolic contours would again allows us the flexibility to gain the efficiency from events which have one strong b-jet and one weaker quality b-jet in signal events. Since the light jet probability distribution is flat in the 2-dimensional space, we expect similar performance from the two b-jet probability.

Along with many different algorithms we tried, we show the most powerful

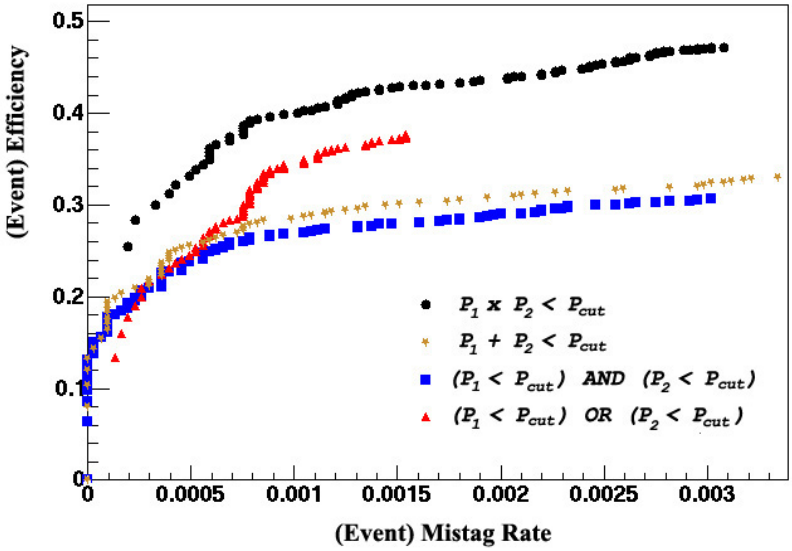

Figure 7.21: Signal ($Z+b\bar{b}$) event efficiency versus mistagged event rate (two mistagged jets) with different strategies used to make the event selection.

combination methods in Fig. 7.21 with the performance of current official operating points for double b-tagging. The 3.6% optimal point for mistag rate corresponds to about 0.1% (∼3.6%×3.6%) event mistag rate for the two b-jet system and at about 0.1% mistag rates, we see that the topological event probability constructed along the hyperbolic contours ($P_1 \times P_2 = const.$) gives much better performance as compared to the traditional square cut analysis (points shown as squares).

Fig. 7.21 shows that at the optimal 0.1% mistagged event rate, the combined product of probabilities achieve as much as 50% increase in signal efficiency over what a traditional square cut analysis can achieve.

7.5 Discussion

In this study, we have demonstrated that more optimal $Z(\mu\bar{\mu}) + b\bar{b}$ selection can be obtained by a simple technique of combining the probabilities of the two similar

objects (μ's or b-jets) in the event resulting in substantial improvements. These more optimal strategies allow more efficiency and high yields for the $Z(\mu\bar{\mu}) + b\bar{b}$ signal which is crucial given the low production cross-sections at the Tevatron.

In the dimuon selection, we first analyzed the best isolation discriminants and constructed an isolation likelihood for the dimuon selection. When compared to a traditional muon isolation cut, our strategy achieved as much as a six fold decrease in the amount of background (at 95% signal efficiency) using the isolation probability obtained from the two muons in the event. The advantage of the method is, however, less pronounced at low signal efficiency levels as seen from Fig. 7.12.

The enhancements for the two b-jet sector was even more striking since we did two layers of optimization for the b-jet identification. First, using the traditional square cut analysis, we found the necessary level of background rate for achieving the best signal significance for the $Z + b\bar{b}$ production. This optimal point was observed to provide as much as 60% increase in the b-tag efficiency when compared to the operating point we have chosen for the ratio of $Z + b$ to $Z + j$ inclusive cross-sections analysis.

A similar combination of the two jet impact parameter b-tag probabilities worked to our benefit for the $Z + b\bar{b}$ signal as well and using this method, we were able to boost the signal efficiency to higher levels while keeping the mistag background at a fixed point as shown in Fig. 7.21. The improvement from this method over the traditional analysis at the previously found optimal operating point was a factor of 1.5.

Combining all these optimal analysis strategies, the sensitivity to $Z(\mu\bar{\mu}) + b\bar{b}$ signal is enhanced substantially. Compared to the strategy used in the measurement of the ratio of cross-sections described in chapter 5, the improvements described here brings about a factor of 3 increase in the signal efficiency at more optimal background levels. According to our projections for about 300 pb^{-1} integrated

luminosity, proposed optimizations would roughly yield about 6.6 $Z(\mu\bar{\mu}) + b\bar{b}$ signal events data as compared to only 2 events that the traditional methods would obtain. Given these improvements, similar levels of statistical significance for $Z + b\bar{b}$ signal can be obtained at less than half the integrated luminosity it would take otherwise.

Bibliography

[1] DØ Run II Collaboration, V. M. Abazov *et al.*, *A Measurement of the Ratio of Inclusive Cross Sections* $\sigma(p\bar{p} \to Z + b \text{ jet})/\sigma(p\bar{p} \to Z + \text{jet})$ *at* $\sqrt{s} = 1.96$ *TeV*, FERMILAB-Pub-04/297-E, submitted to Phys. Rev. Letters, October 2004.

[2] C. Quigg, "Gauge Theories of the Strong, Weak and Electromagnetic Interactions", Addison-Wesley, ISBN 0-201-32832-1 (1997).

[3] V. D. Barger and R. J. N. Philips, "Collider Physics", Updated Ed. Addison-Wesley, ISBN 0-201-14945-1 (1996).

[4] D. Griffiths, "Introduction to Elementary Particles", John Wiley & Sons, ISBN 0-471-60386-4 (1987).

[5] Particle Adventure web site at "`http://particleadventure.org`".

[6] D. J. Gross and F. Wilczek, "Ultraviolet Behavior of Non-Abelian Gauge Theories", Phys. Rev. Lett. **30**, 1343 (1973).

[7] H. D. Politzer, "Reliable Perturbative Results for Strong Interactions?", Phys. Rev. Lett. **30**, 1346 (1973).

[8] S. Eidelman *et al.*, "Particle Data Group Review of Particle Physics", Phys. Lett. B **592**, 1 (2004).

[9] S. Weinberg, Phys. Rev. Lett. **19**, 1264 (1967).

A. Salam, "Elementary Particle Theory", Almquist and Wiksells, Stockholm (1969).

S. L. Glashow, J. Ilipoulos and L. Maiani, Phys. Rev. D **2**, 1285 (1970).

[10] H. L. Lai *et al.* (CTEQ Collaboration), "Global QCD Analysis of Parton Structure of the Nucleon: CTEQ5 Parton Distributions", Eur. Phys. J. C **12** 375 (2000).

[11] P. W. Higgs, Phys. Rev. Lett. **12**, 508 (1964).

[12] J. F. Gunion, H. E. Haber, G. Kane and S. Dawson, "The Higgs Hunter's Guide", Perseus Publishing, ISBN 0-7382-0305-X (1990).

[13] M. Carena, J. S. Conway, H. E. Haber and J. D. Hobbs, "Report of the Tevatron Higgs Working Group", FERMILAB-Conf-00/279-T, hep-ph/0010338 (2000).

[14] T. Hambye, K. Riesselmann, Phys. Rev. **D55**, 7255 (1997).

[15] C. Quigg, "The Top Quark and Higgs Boson at Hadron Colliders", FERMILAB-CONF-98/059-T, hep-ph/9802320 (1998).

[16] The LEP Electroweak Working Group, "A Combination of Preliminary Electroweak Measurements and Constraints on the Standard Model", CERN-PH-EP/2004-069, hep-ex/0412015 (2004).

[17] The LEP Working Group for Higgs Boson Searches, "Seearch for the Standard Model Higgs Boson at LEP", CERN-EP/2003-011 (2003).

[18] More information on the HDECAY program is available at "`http://home.cern.ch/~mspira/proglist.html`.

[19] Y. D. Mutaf, "Search for Discriminating Power in b-jet Identification between Higgs and Gluon Decays", DØ Internal Note# 4084 (2003).

[20] J. M. Campbell, R. K. Ellis, F. Maltoni and S. Willenbrock, Phys. Rev. D **69**, 074021 (2004).

[21] Fermi National Accelerator Laboratory (Fermilab) History Project web pages at "`http://www.fnal.gov/projects/history`".

[22] Fermi National Accelerator Laboratory (Fermilab) Accelerator Division web pages and miscellaneaus internal documents at "`http://www-bd.fnal.gov/`".

[23] Fermilab Run II Handbook at "`http://www-bd.fnal.gov/lug/runII_handbook/RunII_index.html`".

[24] A. Patwa, Ph.D. Thesis, SUNY at Stony Brook, 2002.

[25] C. W. Schmidt and C. D. Curtis, "A 50 mA Negative Hydrogen Ion Source", IEEE Transactions on Nuclear Science, NS-26, 4120 (1979).

[26] J. Thompson, "Introduction to Colliding Beams at Fermilab", FERMILAB-TM-1909, October 1994.

[27] The Fermilab BOOSTER Rookie Book at "`http://www-bdnew.fnal.gov/operations/rookie_books/Booster_PDF/Booster_TOC.html`.

[28] The Fermilab Main Injector Technical Design Handbook, available at "`http://www-fmi.fnal.gov/fmiinternal/MI_Technical_Design/index.html`".

[29] The Fermilab Anti-Proton Source Rookie Book at "`http://www-bdnew.fnal.gov/pbar/documents/PBAR_Rookie_Book.PDF`".

[30] The Fermilab Tevatron Rookie Book at "`http://www-bdnew.fnal.gov/operations/rookie_books/Tevatron_PDF/TeV_Rookie_Book.html`.

[31] DØ Collaboration, V. Abazov *et al.*, T. LeCompte and H. T. Diehl, Annu. Rev. Nucl. Part. Sci. **50**, 71 (2000).

[32] DØ Collaboration. S. Abachi *et al.*, Phys. Rev. Lett. **74**, 2632 (1995).

[33] CDF Collaboration. F. Abe *et al.*, Phys. Rev. Lett. **74**, 2626 (1995).

[34] J. Brzezniak *et al.*, Conceptual Design of a 2 Tesla Superconducting Solenoid for the Fermilab DØ Detector Upgrade, FERMILAB-TM-1886.

[35] P. Balm *et al.*, Magnetic Field Monitors for the DØ Solenoid, DØ Internal Note# 3977 (2001).

[36] DØ Collaboration, Silicon Tracker Technical Design Report, DØ Internal Note# 2169 (1994).

[37] DØ Collaboration, Central Fiber Tracker Technical Design Report, DØ Internal Note# 4164 (1999).

[38] DØ Collaboration, PAC Upgrade Review Report, available at "`http://www-d0.fnal.gov/hardware/upgrade/pac0495/d0toc.html`" (1995).

[39] M. Adams *et al.*, Central Preshower Detector Technical Design Report, available at "`http://d0server1.fnal.gov/users/qianj/CPS/index.htm`".

[40] K. D. Signore, A Core Dump of Useful Information About the Central Preshower Detector, available at "`http://d0server1.fnal.gov/users/qianj/CPS/index.htm`".

[41] A. Gordeev *et al.*, Technical Design Report of the Forward Preshower Detector for the DØ Upgrade, DØ Internal Note# 3445 (1998).

[42] J. Kotcher, Design, Performance and Upgrade of the DØ Calorimeter, FERMILAB-Conf-95/007-E (1995).

[43] J. Krane, Ph.D. Thesis, University of Nebraska, 1998.

[44] L. Sawyer *et al.*, Technical Design Report of the Upgrade of the ICD for DØ Run II, DØ Internal Note# 2886 (1997).

[45] B. S. Acharya *et al.*, Technical Design of the Central Muon System, DØ Internal Note#3365 (1998).

[46] G. Alexeev *et al.*, Technical Design Report for the DØ Forward Muon Tracking Detector Based on Mini-drift Tubes, DØ Internal Note# 3366 (1997).

[47] V. Abramov *et al.*, Technical Design Report for the DØ Forward Trigger Scintillation Counters, DØ Internal Note# 3237 (1997).

[48] G. C. Blazey, Proceedings at the X^{th} IEEE Real Time Conference, Beaune, France (1997).

[49] M. Abolins *et al.*, DØ Run II Level 1 Trigger Framework Design Report, available at "`http://www.pa.msu.edu/hep/d0/ftp/l1/framework/l1fw_tdr_05june98.txt`".

[50] More information on the DØRECO software can be obtined from `http://www-d0.fnal.gov/computing/algorithms/#intro`.

[51] A. Haas, Ph.D. Thesis, University of Washington, 2004.

[52] A. Khanov, "HTF: histogramming method for finding tracks. Algorithm description.", DØ Internal Note# 3778 (2000).

[53] G. Hesketh, Ph.D. Thesis, The University of Manchester, 2003.

[54] P. V. C. Hough, "Machine Analysis of Buble Chamber Pictures", Int. Conf. on High Energy Accelerators and Instrumentation, CERN (1959).

[55] R. Fruhwirth, "Application of Kalman Filtering to Track and Vertex Fitting", Nuclear Instruments and Methods in Physics Research **A262** (1987), 444-450.

[56] A. Schwartzman, "Primary Vertex Selection", DØ Internal Note# 3906 (2001).

[57] A. Schwartzman, "Vertex Fitting by means of the Kalman Filter techinque", DØ Internal Note# 3907 (2001).

[58] A. Schwartzman, "Probabilistic Primary Vertex Selection", DØ Internal Note# 4042 (2002).

[59] C. Luo, Ph.D. Thesis, Indiana University, 2003.

[60] O. Peters, "Muon Segment Reconstruction - Linked List Algorithm", DØ Internal Note# 3901 (2001).

[61] F. Deliot, "The Fit Algorithm in muo_trackreco", available at "`http://www-d0.fnal.gov/d0dist/dist/packages/muo_trackreco/devel/doc/fitalg.ps`", 2001.

[62] C. Clement *et al.*, "MuonID Certification for p14", DØ Internal Note# 4350-v1.0.

[63] S. Protopopescu, "EM Reconstruction Algorithms" available at `http://www-d0.fnal.gov/d0dist/dist/packages/emreco/devel/doc/EMReco.ps` (1999).

[64] F. Beaudette and J.-F. Grivaz, "Road Method: An Algorithm for the Identification of Electrons in Jets", DØ Internal Note# 3976 (2002).

[65] L. Duflot and M. Ridel, "The CellNN Algorithm: Cell Level Clustering in the DØ Calorimeter", DØ Internal Note# 3923 (2001).

[66] A. Alton *et al.*, "Photon Identification for DØ Run II Data", DØ Internal Note# 4487 (2004).

[67] N. Hadley, "Cone Algorithm for Jet Finding", DØ Internal Note# 904 (1989).

[68] Z. J. Casilum and R. Hirosky, "Jet Reconstruction Efficiency", DØ Internal Note# 3324 (1997).

[69] F. Aversa *et al.*, "Toward a Standardization of Jet Definition", Proceedings of Research Directions for the Decade, ISBN:2147483647 (1990).

[70] A. Goussiou *et al.*, "Jet Energy Scale for p11 Data", DØ Internal Note# 4112 (2002).

[71] N. Parua, "Status of Jet Energy Scale", Talk Presented at the DØ Collaboration Meeting, Fresno, California (2004).

[72] I. Csabai *et al.*, "Quark and Gluon Jet Separation Using Neural Networks", Phys. Rev. **D44**, 1905-1908 (1991).

[73] J. Pumplin, "Quark / Gluon Jet Discrimination at Hera", Nucl. Phys. **B390**, 379-398 (1993).

[74] P. Grannis, "Topological Quark/Gluon Jet Tagging", DØ Internal Note# 2188 (1994).

[75] A. Schwartzman, "Track Jet Studies Using a 3-Dimensional Simple Cone Jet Algorithm", DØ Internal Note# 3919 (2001).

[76] A. Schwartzman, "b-quark Jet Identification via Secondary Vertex Reconstruction", DØ Internal Note# 4080 (2003).

[77] L. Feligioni *et al.*, "Update on b-quark Jet Identification with Seondary Vertex Reconstruction using DØRECO Version p14", DØ Internal Note# 4414 (2004).

[78] D. Bloch *et al.*, "Jet Lifetime b-tagging", DØ Internal Note# 4069 (2002).

[79] D. Bloch *et al.*, "Performance of the JLIP b-tagger in p14", DØ Internal Note# 4348 (2004).

[80] More information on top_analyze software package can be obtained at "`http://www-d0.fnal.gov/Run2Physics/top/d0\_private/wg/top\_analyze/top\_analyze\_documentation.html`", 2004.

[81] More information on top_dq software package can be obtained at "`http://www-d0.fnal.gov/d0dist/dist/packages/top\_dq/devel/doc/usage.htm`", 2004.

[82] M. L. Mangano *et al.*, "ALPGEN, a generator for hard multiparton processes in hadronic collisions", JHEP 0307:001 (2003).

[83] M. L. Mangano *et al.*, "Multijet matrix elements and shower evolution in hadronic collisions: W B Bbar + N jets as a case study", Nucl.Phys.B632:343-362 (2002).

[84] T. Sjöstrand *et al.*, "High-Energy-Physics Event Generation with PYTHIA 6.1", Comput.Phys.Commun. 135, 238-259.(2001).

[85] More information available at "`http://www-d0.fnal.gov/phys_id/bid/d0_private/certification/p14-certification.html`" (2004).

[86] K. Hanagaki, "Observation of b-jets in Z(→ee) events", DØ Internal Note # 4353 (2004).

[87] S. Choi (private communications).

[88] J. M. Campbell and S. Willenbrock (private communications).

[89] C. M. Bishop, "Neural Networks for Pattern Recognition", Oxford University Press Inc., ISBN 0-198 53864-2 (1996).

[90] N. Amos *et al.*, "The Random Grid Search: A Simple Way To Find Optimal Cuts", Computing In High Energy Physics, **95** 215-219, Rio de Janeiro, Brazil (1995).